GRANULAR SHOCKS, PARTICLE SIZE SEGREGATION AND LEVEE FORMATION IN AVALANCHES AND DEBRIS FLOWS

A thesis submitted to the University of Manchester
for the degree of Doctor of Philosophy
in the Faculty of Engineering and Physical Sciences

2011

Christopher G. Johnson
School of Mathematics

Contents

Word count 29210

List of Figures

The University of Manchester

Christopher G. Johnson
Doctor of Philosophy
Granular shocks, particle size segregation and levee formation in avalanches and debris flows
February 22, 2011

Debris flows, avalanches and other geophysical mass flows pose a significant hazard to settlements in or near mountainous regions. Understanding the physical processes that govern these flows is an essential part of hazard assessment and mitigation strategies. This thesis addresses two aspects of geophysical mass flows: flow self-channelisation due to the formation of lateral levees, and granular shocks, which occur when a rapidly-moving debris flow or avalanche collides with an obstacle. We present the results of large-scale debris flow experiments in which the flow is channelised by coarse-particle levees that form at the flow margins. The flow surface velocities are measured with high speed overhead photography, and the deposits both sampled to obtain the grain size distribution and excavated to recover the deposited locations of tracer pebbles that were introduced in to the flow. We propose a model, supported by evidence from the large-scale experiments, that describes in detail the size segregation and kinematic transport processes responsible for the deposition of lateral levees. The second problem addressed in the thesis concerns granular shocks, or jumps, which are rapid changes in the depth and velocity of granular avalanches. We investigate these through experiments in which a falling jet of granular material impacts on an inclined plane, generating a steady granular jump, which is either teardrop-shaped or 'blunted'. Numerical solutions of a depth-averaged flow model agree quantitatively with many of the observed flow features. We use this model show that the transition between the teardrop-shaped and blunted jump regimes corresponds to a transition between two shock reflection structures, known as a regular and a Mach shock reflection. On planes inclined at a shallow angle, we demonstrate a wide variety of unsteady and channelised flows, which occur due to the complex interaction between flowing and stationary regions of granular material.

Declaration

No portion of the work referred to in this thesis has been submitted in support of an application for another degree or qualification of this or any other university or other institute of learning.

Copyright Statement

(see http://www.manchester.ac.uk/library/aboutus/regulations) and in The University's policy on presentation of Theses.

1. Introduction

In regions of steep terrain, geophysical mass flows are a common occurrence. This term encompasses a wide range of flows including lahars, snow avalanches, pyroclastic density currents and debris flows, all of which involve the rapid downslope transport of rock, debris and water. Such flows comprise a flowing solid granular phase, which is frequently coupled to a flow of the surrounding fluid, either water, air or volcanic gas. Geophysical mass flows are distinguished from the broader class of downslope mass movement processes (which includes soil creep, landslides and rockfalls) by their fluid-like behaviour. This behaviour is achieved when the granular component of a mass movement is sufficiently dense and rapidly-moving that it flows as a coherent fluidised mass.

Geophysical mass flows vary widely: in composition, from entirely water-saturated streamflows to dry rock avalanches; in size, from $\sim 10^2$ m^3 to $\sim 10^9$ m^3; and in speed, from less than one metre per day for earth flows (Hungr *et al.*, 2001) to over 100 m s^{-1} for the fastest pyroclastic density currents (Branney & Kokelaar, 2002). Their ability to flow as a fluid means that they may travel several tens of kilometres before coming to rest: such flows can be highly destructive, and pose considerable risk to life and property. This risk is heightened by the unpredictable initiation of geophysical mass flows: they may occur spontaneously when rainfall or meltwater destabilises slopes, or be triggered by volcanic eruptions or earthquakes. Throughout the long history of observation and modelling of geophysical mass flows (Lord Bishop of Clogher, 1712), a great deal of research has been motivated by the need to predict and understand large-scale flows for the practical purposes of hazard assessment and mitigation.

The coherent, fluid-like behaviour of geophysical mass flows motivates a continuum approach to modelling. However, the wide range of frictional, collisional, viscous and

cohesive forces that act upon each grain makes the problem of finding a universal granular rheology extremely challenging. In certain regimes, such as in quasi-static deformations, gas-like collisional flows (*e.g.* Campbell, 1990) and, more recently, dense granular flows (GDR MiDi, 2004; Jop *et al.*, 2006), there has been considerable success in rheological modelling. In geophysical mass flows the presence of a broad particle size distribution makes the prediction of rheology more complex; modelling is further complicated by particle size segregation, which renders flows and their rheologies spatially heterogeneous.

From a practical standpoint, the need for a rheology when modelling geophysical mass flows is partially mitigated by the observation that such flows are typically shallow, in the sense that their depth is much smaller than their horizontal length. This separation of scales allows a depth-averaged modelling approach, first derived by Savage & Hutter (1989), in which the flow is modelled by an incompressible fluid with a hydrostatic pressure. For a one-dimensional flow on a slope inclined at angle ζ from the horizontal, Savage & Hutter (1989) show that the Navier-Stokes equations governing the flow are reduced to depth-integrated mass and momentum equations,

$$\frac{\partial h}{\partial t} + \frac{\partial}{\partial x}\left(h\bar{u}\right) = 0\,, \tag{1.1}$$

$$\frac{\partial}{\partial t}\left(h\bar{u}\right) + \frac{\partial}{\partial x}\left(h\overline{u^2}\right) + Kg\cos\zeta\frac{\partial}{\partial x}\left(\frac{h^2}{2}\right) = hg\cos\zeta\left(\tan\zeta - \mu\ \mathrm{sgn}\ \bar{u}\right)\,, \tag{1.2}$$

where x is the downslope coordinate, t is time, h is the flow depth, $\bar{u}$ is the depth-averaged downslope flow velocity and g is the acceleration due to gravity. Depth-averaging the system of equations encompasses the effects of the rheology into two functions, the basal friction μ and earth-pressure coefficient K (the ratio of downslope to slope-normal tangential stress within the flow), for which Savage & Hutter use a constant Coulomb basal friction and an earth-pressure coefficient derived from a Mohr-Coulomb yield criterion. More recent extensions to the depth-integrated model include two-dimensional flow over arbitrary topography, pore-pressure effects (Iverson & Denlinger, 2001) and more sophisticated basal friction models (Pouliquen, 1999).

The equations of the Savage-Hutter model (1.1, 1.2) are hyperbolic and form shocks, which are analogous to the hydraulic jumps seen in shallow water flows. These discontinuities in flow height and velocity can occur in supercritical flows (those where the Froude number

$|\bar{u}|/\sqrt{gh}$ is greater than unity), either as one-dimensional bores or as two-dimensional oblique shocks (Hákonardóttir & Hogg, 2005; Cui *et al.*, 2007). Shocks are especially relevant to geophysical mass flows in the context of interactions between the flow and obstacles, such as protective structures and dams (Gray *et al.*, 2003). Protective structures are an important part of geophysical mass flow mitigation, and are designed to halt flows or divert them away from buildings and inhabited areas. The modelling of shocks is of practical importance in the design of protective structures for snow avalanches (Jóhannesson *et al.*, 2009) and debris-flows (Takahashi, 2007).

1.1 Structure of the thesis

This alternative format thesis is presented in the form of two papers, both on the modelling of unconfined free-surface granular flows.

In *The kinematics of levee formation in geophysical mass flows* (chapter 2), we describe large-scale experiments performed at the US Geological Survey debris flow flume, and present a theory to explain the formation of coarse-particle-rich lateral levees. The large-scale experiments involve the flow of ~ 10 m^3 of water-saturated sand and gravel down a ~ 100 m flume. We make detailed measurements of the surface velocity field of these flows and carefully excavate the deposit, sampling the particle size distribution and recording the deposited locations of coarse tracer stones that are introduced into the flow. The surface velocity field measurements allow us to infer constraints on the vertical velocity profile and deduce the structure of the three-dimensional velocity field in the flow head. We couple this velocity field to a model for particle size segregation, which allows us to predict the transport and accumulation of coarse particles within the flow. These predictions are supported by the experimentally observed distribution of coarse particles within the deposit.

Contributions to this paper was as follows: CGJ designed and implemented the procedure for acquiring surface velocity fields, analysed the experimental data and wrote the paper, with editorial comments from JMNTG, BPK and RMI. Additionally, BPK and RMI contributed text to the paper introduction. Measurement and control systems at the USGS debris flow flume were designed and implemented by ML and RGL. All the authors took part in the large-scale

experiments.

Chapter 3 consists of the paper *Granular jets and hydraulic jumps on an inclined plane*, which has been accepted for publication by the *Journal of Fluid Mechanics*. In this paper, we describe laboratory experiments and numerical solutions of the flow generated when a falling jet of granular material impacts upon an inclined plane. The jet impact produces a region of thin, rapidly-flowing radial flow on the plane, which transitions to a thicker, more slowly-moving downslope avalanche through a closed granular shock. We show that this shock can take one of two steady forms, either teardrop-shaped or 'blunted', and use a depth-integrated flow model to show that the these regimes correspond respectively to either a regular or a Mach shock reflection. Outside the regime of steady closed granular jumps, the interaction between flowing and stationary material on the plane leads to a variety of complex unsteady and asymmetric flows. The paper was written by CGJ, who also performed the experiments and wrote the numerical code. JMNTG initially suggested the problem, and provided editorial comments on the manuscript.

Both papers draw on the results of experimental flows which, although 'large-scale' in one case, are considerably smaller than natural avalanches and debris flows. The relevance of these experiments to full-scale flows depends on the extent to which flows are governed by scale-invariant physical processes. A difficulty in the modelling of geophysical mass flows is that flow rheology may be dependent on a number of mechanisms that do not scale: (Iverson *et al.*, 2010) demonstrates that pore-pressure effects become increasingly significant as the flow scale is increased, whereas flow yield strength and viscosity become decreasingly important. The rheology of small-scale experiments may therefore differ entirely from that of natural geophysical mass flows.

The modelling employed in this thesis centres on kinematics in an incompressible flow, in chapter 2, and granular shocks, in chapter 3. These features of the experimental flows are dependent on the incompressibility and shallow aspect ratio of the flows, which are independent of scale. While the rheology of experimental flows, especially of the small-scale experiments in chapter 3, may not be representative of full-scale geophysical mass flows, the modelling of kinematics and shock phenomena may be extended to large-scale flows.

An example of such scaling behaviour is illustrated in figure 1.1, which shows a small-scale bidisperse dry grain flow (*a*), alongside a debris-flow experiment ~ 70 times larger (*b*). Despite the considerable difference in rheology and dynamics between the two flows, both are near-incompressible and have qualitatively similar velocity fields, meaning that the kinematic process of coarse-particle-rich levee formation described in chapter 2 applies equally to both.

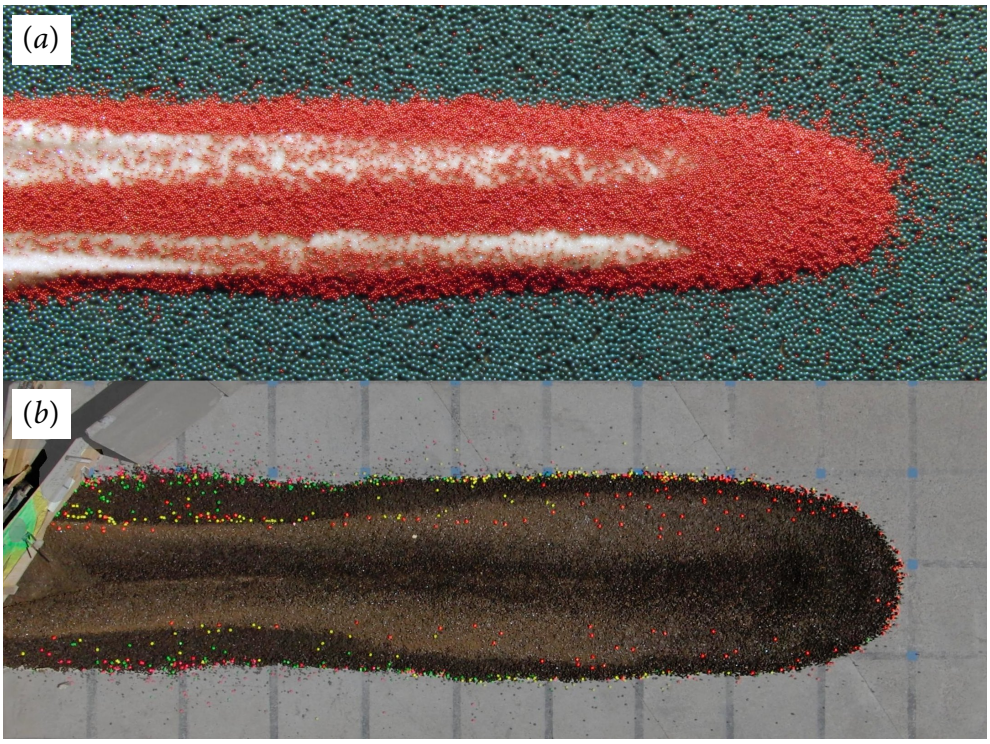

Figure 1.1: Two levee-channelised grain flows differing in scale by a factor of ~ 70. Despite different rheologies, both flows have a similar height and velocity fields (up to scaling factors). Typical flow properties are:

	(*a*)	(*b*)
Grains	Glass beads 300–400 μm, red (37.5% by mass) 75–150 μm, white, (62.5% by mass)	Water-saturated debris up to 32 mm diameter
Width	25 mm	2 m
Depth	3 mm	0.2 m
Slope angle	27.5°	2°
Flow speed	5 cm s^{-1}	4 m s^{-1}
Froude number	0.3	3

2. The kinematics of levee formation in geophysical mass flows

Publication 1: *The kinematics of levee formation in geophysical mass flows*

The kinematics of levee formation in geophysical mass flows

C. G. Johnson[1], B. P. Kokelaar[2], R. M. Iverson[3], M. Logan[3], R. G. LaHusen[3], J. M. N. T. Gray[1]

C. G. Johnson,

School of Mathematics,

University of Manchester,

Oxford Road,

Manchester (cjohnson@maths.manchester.ac.uk)

[1]School of Mathematics and Manchester Centre for Nonlinear Dynamics, University of Manchester, Manchester, UK.

[2]School of Earth Sciences, University of Liverpool, Liverpool, UK.

[3]U.S. Geological Survey, Cascade Volcano Observatory, Vancouver,Washington, USA.

Abstract. Particle size-segregation can influence bulk flow properties and hence the rate and distance of runout of diverse geophysical flows, including debris flows, pyroclastic currents and snow avalanches. Runout enhancement can occur through the spontaneous formation of coarse-particle-rich lateral levees which channelise the subsequent flow. We report the results of large-scale debris-flow experiments and analyse these results using a kinematic model of particle size segregation and transport within the debris-flow head. The experimental flows travel ∼80 m down a flume before forming an elongated deposit ∼10 m long on a runout pad. During formation of the deposit, we measured the surface velocity field using high-speed overhead photography, and we assessed the contemporaneous internal segregation of coarse particles by placing tracers particles ahead of the flow on the runout pad, which were incorporated into the flow. We determined the deposit granulometric architecture and the deposited location of the tracer particles by detailed transect sampling and systematic excavation. We found that coarse-rich levees formed by rapid progressive streamwise accretion approximately 3.5 m behind the flow front. Coarse particles migrated vertically at up to ∼6–7.5 $\mathrm{cm\,s^{-1}}$ in experimental debris-flows with a mean channel-flow velocity of ∼4 $\mathrm{m\,s^{-1}}$ and frontal advance rate of ∼2 $\mathrm{m\,s^{-1}}$. Formation of coarse-enriched levees resulted from the development of a recirculating region of coarse material in the debris-flow head. Coarse particles within this region followed spiral trajectories outwards into the progressively-accreting levees, whereas small particles migrated to the base of the flow and deposited in the channel be-

tween the levees. Although there was clear evidence for inverse grading occurring within the flow, the resulting leveed-channel deposit was strongly laterally graded, with only weak vertical grading.

1. Introduction

Debris flows, pyroclastic flows, snow avalanches and rockfalls transport particles that can have wide ranges of size, shape and density. Particle segregation can cause formation of relatively coarse-grained, frictionally resistive flow fronts that progressively build lateral levees, which in turn channelise the flows. The spontaneous channelisation restricts lateral spreading and thus can increase the travel distance, or runout.

This paper describes large-scale flume experiments and mathematical modelling of the interrelations between flow kinematics, granular segregation and levee deposition during the emplacement of debris flow deposits. We find a continuous process of granular flow and segregation that leads to the progressive, streamwise accretion of coarse-enriched levees a short distance behind the flow front. Whereas previous authors [e.g. *Sharp and Nobles*, 1953; *Branney and Kokelaar*, 2002; *Iverson et al.*, 2010] have simply described the channelised flow as 'shouldering aside' the coarse-grained flow front to form the levees, we investigate in detail a continuous process of granular flow and segregation that leads to progressive, streamwise levee formation.

It has long been known that, during flow of dry granular mixtures down a rough inclined plane, large and small particles unmix and tend to develop an inversely graded (coarsening upwards) particle-size distribution. The segregation occurs as small particles preferentially percolate downwards through spaces that open in the shearing, somewhat dilated mixture, and large particles consequently are forced towards the top of the flow [*Bagnold*, 1954; *Middleton*, 1970; *Middleton and Hampton*, 1976; *Savage and Lun*, 1988]. In geophysical mass flows, several mechanisms may drive and modulate segregation. Interstitial fluids can

hinder segregation by reducing the density difference between particles and fluid [*Vallance and Savage*, 2000; *Thornton et al.*, 2006]. In pyroclastic flows that transport low-density pumice, large fragments may rise to the flow surface for the additional reason that they are positively buoyant within the shearing dispersion [*Branney and Kokelaar*, 2002].

A coarse-particle-rich region at the flow surface, moving faster than the relatively fine material beneath due to vertical shear in the flow, preferentially advects the coarse material to the flow front, where it tends to accumulate. The higher pore-fluid diffusivity of the coarse-particle front allows the high pore pressures generated in large-scale flows to dissipate [*Iverson*, 1997] and results in the frontal accumulation being frictionally more resistant to flow than the shearing dispersion behind it [*Major and Iverson*, 1999]. This increased resistance causes a flow-front instability [*Pouliquen et al.*, 1997; *Pouliquen and Vallance*, 1999], the most obvious manifestation of which is the production of lobe-and-cleft form deposits. The coarse material may either become over-run and circulated within the head region before lateral expulsion, or advected directly into levees. Coarse-grained levees form behind the flow front on both sides, and each may amalgamate with an adjacent levee to obliterate the initial inter-lobe cleft [*Major*, 1997; *Pouliquen et al.*, 1997; *Pouliquen and Vallance*, 1999].

The segregation of coarse particles to the top of a flow and their resulting enhanced mobility due to vertical shear has been modelled by *Gray and Ancey* [2009]. In laboratory experiments of two-dimensional bidisperse granular avalanches, *Gray and Ancey* [2009] show that coarse particles transported to the flow front are deposited at the base of the flow, forming a deposit that has coarse particles at the base and at the surface, with fine particles in between. *Gray and Ancey* [2009] model the segregation and transport

processes in this flow using the particle size segregation model of *Gray and Thornton* [2005], and show that a recirculating region of coarse particles exists at the flow front. *Gray and Kokelaar* [2010] derive a one-dimensional depth-integrated form of the *Gray and Thornton* [2005] particle size segregation model and show that this reduced model correctly predicts the transport of coarse particles to a flow front, while being in a form suitable for augmenting existing depth-averaged flow models [e.g. *Iverson and Denlinger*, 2001].

While the accumulation of coarse particles at the flow front is understood in two dimensions, the resulting segregation mobility feedback, which causes transverse flow-front instabilities and the formation of leveed channels, is less clear. For example, we do not know the mechanism that defines the characteristic lengthscale of lobe-and-cleft form deposits, nor what controls the relationship between width and height of a leveed-channel flows. *Félix and Thomas* [2004] suggest relationships between the geometry of the deposit and the flow-front height and velocity of the parent flow based on laboratory experiments, but deeper understanding of the flow mechanisms is needed to be able to anticipate large-scale flow behaviour.

Scientific documentation of depositional levees bordering the paths of debris flows and avalanches dates back more than a century [e.g. *Stiny*, 1910; *Heim*, 1932], and modern work adds quantitative rigour to such documentation [*Conway et al.*, 2010, e.g.]. Early eye-witness accounts of the levee-formation process include that of *Sharp and Nobles* [1953], who noted that levees formed as resistive, coarse-grained debris-flow snouts were shouldered aside by advancing finer-grained debris. Thus, scientific observers have long recognised the important role of heterogeneous debris-flow architecture during levee

formation: high-friction, coarse-grained snouts are displaced laterally by low-friction, fine-grained tails. Implicitly, this view also recognises the importance of grain-size segregation, which contributes to the heterogeneous flow architecture.

Pioneering quantitative work on debris-flow mechanics and levee formation, especially that by *Johnson* [1965, 1970]; *Johnson and Rodine* [1984], acknowledged the heterogeneous character of debris flows but sought to simplify the phenomenon to make it more amenable to analysis. Thus, Johnson adopted a homogeneous Bingham model as a substitute for a more complicated "Coulomb-viscous" model of debris-flow rheology. Whereas Johnson himself remained keenly aware of the limitations imposed by the Bingham idealisation, other investigators predicated their interpretations on its veracity. Even today, some researchers base their interpretations of debris-flow levee formation on the Bingham idealisation [e.g. *Mangold et al.*, 2010]. Such interpretations assume that levees form as a consequence of inherent material yield strength, independent of influences of internal flow dynamics or heterogeneous flow architecture.

Evidence contradicting the Bingham model of levee formation comes not only from field observations but also from reproducible large-scale experiments involving flows of $\sim 10\ \mathrm{m}^3$ of heterogeneous, water-laden debris [i.e. *Iverson*, 1997; *Major*, 1997; *Major and Iverson*, 1999; *Iverson et al.*, 2010]. In these experiments coarse grains (i.e., gravel) became concentrated at flow fronts as a result of size segregation, and levee formation appeared to involve the same shouldering aside of coarse snout debris noted by *Sharp and Nobles* [1953]. A key aspect of the process, well-documented with sensor data, was the persistence of a nearly liquefied, low-strength state of fine-grained debris in the core of flows core. This mobile core material advected some of its downstream momentum into the resistive,

coarse-grained snouts, thereby providing motive force to drive the snouts forward and produce the "shouldering" effect. However, some features of deposition became obscured because trailing watery debris tended to overtop the snout and levees that were emplaced by the head of the flows. The experiments also lacked high-resolution particle tracking during the levee formation process, thereby leaving many unanswered questions about the internal flow dynamics that result in characteristic depositional patterns.

2. Methodology

We used the flume of *Iverson et al.* [2010] to study the effect of particle size segregation on the flow propagation and deposit. The USGS debris-flow flume consists of a straight concrete channel 95 m long, 2 m wide and 1.2 m deep, inclined at 31° to the horizontal (figures 1 and 2). In the lowest 8.5 m the slope transitions smoothly to 4°, before the flume opens onto a concrete runout pad, 25 m long and inclined at ∼2.4°. At 12.5 m from the top of the flume, two 2 m-high vertical doors form gates of a hopper that allows water-saturated sediment to be held and released. The flume walls and the runout area are smooth, but most of the length of the flume bed, between 6 m downslope of the hopper and 3.5 m upslope from the flume mouth, is roughened with bumps 16 mm high and spaced 50 mm apart. We report the results of two experiments, run on 25th and 27th August 2009, using initial charges of 10 m^3 of water-saturated sand (0.0625–2 mm; 33%) and gravel (2–32 mm; 66%) with a trace of mud (< 0.0625 mm), called 'SG' by *Iverson et al.* [2010]. *Iverson et al.* [2010] give full details of the experimental set up and 'SG' properties, and show that these experiments are reproducible.

When the flume hopper gates open, the wet sediment behind them collapses and accelerates down-slope, reaching the flume mouth in ∼10 s (figure 3). As the sediment mixture

travels down the flume, it develops a gravel-enriched snout followed by finer and wetter material; some coarse particles bounce far ahead of the snout. The debris then discharges onto the runout pad, forming an elongated deposit. Movie 1, in the dynamic content accompanying this paper, shows a debris-flow in progress at the USGS flume. In previous experiments [*Iverson*, 1997; *Major*, 1997; *Major and Iverson*, 1999; *Iverson et al.*, 2010], after the debris flow had extended onto the runout area and deposited a well-formed leveed mound, there was a tendency for a succession of water-rich roll-waves in the latter part of the flow to override and so erode and partly bury the initial deposit, making it difficult to sample and interpret.

To focus on the initial runout and deposition in our experiments, we truncated the flow shortly after the head discharged from the flume mouth and diverted much, but not all, of the watery flow tail. To do this a reinforced plywood barrier attached to the backhoe of a tractor was forcefully and rapidly dropped obliquely across the flume mouth as the discharge began to wane, ~ 5 s after the flow had first reached the runout pad (figures 1 and 2). The diverted flow was then partly channelled by concrete barriers away from the runout pad and partly backed up, depositing material between the flume sidewalls. The diversion of the watery tail meant that the last material to pass under the diverter before the flow-head truncation was of a similar grain-size distribution and water content to the initial charge. In the minutes after the diverter had been deployed, only a small quantity of water and fine particles leaked into the proximal part of the initial deposit, insufficient to erode the deposited levees.

During passage of the debris flows down the flume, continuous measurements of flow thickness, bed-normal stress and bed pore-fluid pressure were made 32 m, 66 m and 80 m

downslope from the hopper gates (figure 3). The speed of propagation of the flow front, and the flow thickness and stresses at 32 m and 66 m, are nearly identical for the two experiments, and they are very close to the mean behaviour measured in previous experiments with similar experimental conditions [*Iverson et al.*, 2010, figure 12]. At 80 m below the gates (2.5 m upslope from the flume exit), the initial peaks in flow thickness and stresses, ~14 s after gate opening, are larger in the experiment of 27th August, indicating a more substantial flow head at this location in this experiment. The relative increases in all quantities late in the 27th August flow merely reflect the backing-up of the tail of the flow against the flow diverter, which was emplaced 16–18 s after gate opening.

2.1. Particle tracking and surface velocity calculation

To investigate the kinematics of the flow and deposition during the debris-flow runout, the surface velocity field and the evolution of the boundary between flow and deposit at the surface were measured from high speed overhead photographs. To assist in this process, the debris flows were marked by adding coloured tracers onto their surface. Approximately 1600 painted wooden cubes, of side length 2 cm, were placed close-packed in rows on a board over the flume near the exit (figure 2) and were dropped onto the flow surface steadily over a period of 3 s as flows discharged from the flume mouth. The cubes were painted one of four colours, which were dropped in sequence. As well as providing markers to indicate velocity fields, the positions of the cubes in the deposits, whether on the surface or in the interior, provided information about the deposition order and processes. Movie 2 shows an overhead view of the runout of the 25th August experiment, in which the seeding of tracer cubes onto the flow surface and the operation of the flow diverter can be seen.

Measurements of the surface velocity field were made from sequences of 105 images taken during the 2.5 s period when the flow front was between ~5 m and 10 m beyond the flume mouth. Two sequentially triggered Casio EX-F1 cameras were used, mounted above the runout area on an overhead cable and triggered remotely. The temporal resolution was 60 frames per second for 1 s and 30 frames per second for the subsequent 1.5 s; the spatial resolution was approximately 3.5 mm per pixel. Calibration of the cameras was achieved by painting a 1-metre grid of markers on the runout area. The markers were identified in the experimental image sequences and used to calculate a least-squares fit of the camera position and orientation (which varied slightly throughout the image sequences because the camera mount was freely suspended) and the radial distortion function of the lenses. The mean calibration error was typically ≤ 6 mm.

Surface flow velocities were calculated using Particle Tracking Velocimetry (PTV). Approximately 1000 coloured tracer particles and natural gravel particles were identified in each image, and the location of each was tracked over ~25 adjacent frames by custom PTV software. Each particle track was checked manually and was discarded if a particle had been incorrectly identified between images, or if the motion of a tracer particle on the flow surface did not reflect the velocity of the flow around it. The latter occurrence was almost entirely confined to the first 1–2 m of runout, where tracers that had just been seeded were liable to roll across the flow surface briefly before becoming stably incorporated into the flow. Particle velocities were then calculated using a centred finite-difference time derivative of the particle positions, and the velocity field interpolated linearly on a Delaunay triangle mesh of the particle positions. The precision of the velocity measurements was 8.9 mm s^{-1}, or approximately 0.5% of a typical flow velocity. Positional accuracy of

the velocity estimates was limited by the distance travelled by a particle between two adjacent frames, and by the size of the comparison 'window' used to determine particle positions. Both of these were ∼7 cm for the data presented in this paper.

3. Description of the flow runout and deposition

After discharging from the flume, the debris flows of 25th and 27th August continued onto the runout pad, respectively, for 12 m and 9.5 m before complete deposition occurred. These runout distances differ little from those observed in similar experiments in which flows were not beheaded by the flow diverter [*Iverson et al.*, 2010, figure 17]. During the runout, both flows deposited continuously as material near the front of the flow slowed in a flow 'head' region, and was deposited in levees that defined a flow channel of near-constant width (figure 4*a*).

The time-evolution of the channelised flow through to eventual complete deposition in the experiment of 25th August is shown in figure 4(*b*), in which the downstream location of the flow head and extent of the levees is plotted. Most of the runout distance is attained in the first 5 s after the flow exits the flume, during which both the flow front and head propagate downstream at a near-steady velocity of $2.0\,\mathrm{m\,s^{-1}}$. The levees form approximately 3.5 m behind the front. Towards the end of the flow, as the flux of material at the flume exit wanes, the levee formation slows dramatically, practically stopping streamwise levee accretion. At this time, ∼5–8 seconds after the flow reaches the runout pad, propagation of the flow front slows while material in the centre of the channel remains in motion, causing the flow head to widen slightly to form a bulbous snout.

The majority of the deposit is formed between ∼1.5 and 5 s after the flow exits the flume, when the debris flow head advances and levees accrete downstream quite steadily.

Although the volume of sediment used in the experiments is limited by practical considerations, we infer that in natural flows of longer duration, this near-steady regime of flow and deposition may be responsible for the majority of the organisation of deposits. Thus the interactions between flow kinematics, granular segregation and levee deposition in this regime, especially in the flow head, are of great interest.

The experimental deposit of 25th August is shown in figure 4(c), with the time when each part of the surface of the flow became stationary indicated by colouring, showing the spatial order of surface deposition. The main process in the runout, the steadily advancing flow front and downstream-accretion of levees, is illustrated in this figure. Until the flow is diverted at $t \approx 5$ s, figure 4(c) shows that the levees form only through streamwise accretion, with no progressive widening of the levees once they have been deposited.

After the deployment of the flow diverter, the abrupt cessation of flow from the flume changes the runout substantially, and two further processes occur. At around 6–6.5 s, the height of flow in the channel drops rapidly, and leads to a widening of the levees inwards behind the head region. Immediately afterwards, material in the leveed channel and most of the head stops near-simultaneously at ~6.5–7.5 s and slight lateral bulging of the head is evident. While these later processes influence the experimental flow deposits described later, they are not as relevant to natural debris flows as the process of steady front-propagation and streamwise levee accretion that occurs during most of the runout.

Figure 4(c) shows the time of deposition at the surface; it is possible that underlying material may have deposited somewhat sooner than that on the surface, due to vertical progressive aggradation [c.f. *Major*, 1997]. At the margins of the flow, the flow head reaches a downstream location only 1.5 s before deposition of the levee occurs at the

surface; this is therefore the longest period over which vertical progressive aggradation could occur in the levees. It is probable that vertical aggradation in the levees occurs much more rapidly than this: image sequences taken from ground level looking perpendicular to the accreting levee wall show that at the surface, the boundary separating flowing from deposited material is inclined at approximately 45° to the horizontal (and propagates downstream with the flow head at $2.0\,\mathrm{m\,s^{-1}}$). Material at the highest point on the levee therefore deposits only ~ 0.1 s after that at ground level (at the same downstream location) indicating a rapid vertical aggradation. By contrast, in the central channel, vertical progressive aggradation is quite possible, and is a likely cause of the near-simultaneous stopping of surface material after the flow tail is diverted.

Figure 5 shows a sequence of side-on views of the 25th August debris flow, taken at 0.2 s increments, from which the near-steady propagation of the debris flow front is evident. The extent of the progressively growing levees is indicated by arrows, upstream of which the leveed channel is of uniform height. The flow head raises above the height of the channel, and exhibits the steep front and thin precursory flow seen in natural single-surge debris flows [*Sharp and Nobles*, 1953; *Pierson*, 1986]. During the experiments we observed approximately two travelling waves behind the resistive flow front, which progress downstream at approximately the front propagation speed. The amplitude and the position of these waves (with respect to the flow front) evolve slowly with time, which causes a temporal variation in flow head height that can be seen in figure 5. Additionally, there is a component of repeated front steepening and collapse which affects the size of the thin precursory surge ahead of the flow. However, both these unsteady phenomena

are minor in comparison to the overall steady propagation of the flow front, as evidenced by the highly uniform width and height of the deposited levees.

4. Particle Paths

The incremental formation of levees is demonstrated in figure 6 by tracing the path of two sequences of five particles, each of which enters the runout area at the same transverse location. An animation of this figure is shown in movie 3. Before deposition, the particle sequences form two parallel lines in the central flowing channel, with particle 1 furthest downstream. This is the case in figure 6(a), where only particles 1 and 2 have entered the field of view. In figure 6(b), particles 3–5 have moved into view, following the same parallel paths. Particles marked 1 and 2 have reached the flow head region and have been transported laterally outwards; particles marked 1 have deposited on the levee surface. In figure 6(c), particles 1–3 have deposited in the levee, and particle 4 is being advected towards the edge of the flow. In figure 6(d), all particles have deposited in the levees, with the location of deposition reversed from that which originally existed in the flow: particles marked 5 are now the furthest downstream. This reversal of longitudinal position is also evident from the colour of the tracer cubes deposited in the levees. The cubes were seeded onto the flow surface in four colours in sequence (shown in movie 2): pink first, followed by green, then yellow, then orange. Figure 7 shows a photograph of the deposited levee, pink tracers are located in the proximal part of the levee, with green, yellow and orange found progressively farther downstream.

Only about half of the tracer cubes that were placed on the flow surface remained on the surface of the final deposit; the remainder were found buried within the deposit interior. Figure 8 shows the trajectories of a set of particles that at $t = 2\,\mathrm{s}$ lie in a transverse line

across the flow, ~ 1.5 m beyond the flume exit. At $t = 3.2$ s particles that were near the edge of the flow, marked with circles, remain on the surface after being advected into the levees in the same manner as the particles in figure 6. In contrast, particles that were near the centre of the channel, marked with crosses, reached and passed over the advancing flow front, and were then buried by material which followed. Particles on the flow surface can therefore be divided into two distinct sets: those near the flow margins which remain on the surface and are advected onto the levee surface, and those nearer the flow centreline, which are transported to the flow front and buried by subsequent material.

Figure 9 shows the surface velocity field of the flow of August 25th at $t = 3.5$ s, the same time as is shown in figure 4(a). The surface velocity is indicated by arrows, with deposited material (defined as having surface velocity $\leq 20\,\mathrm{mm\,s^{-1}}$) denoted by dark shading. At their full development, the levees occupy approximately half the flow width and the channelised flow between them is directed entirely down-slope, with a rounded velocity profile. The maximum downstream surface velocity at $t = 3.5$ s is $6.1\,\mathrm{m\,s^{-1}}$, with a variation of less than $\pm 2\%$ along the leveed section from $x = 1.5$ m to $x = 4.5$ m. The velocity profile and the levee width similarly exhibit only small streamwise variation. The levees and flow upstream of the head are therefore largely independent of the downstream coordinate x. The rounded Poiseuille-like velocity profile in the leveed channel is observed also in some natural debris-flows [*Pierson*, 1986]. Transverse and vertical shear rates are both of order $20\,\mathrm{s^{-1}}$ in the leveed channel, indicating that horizontal stresses – commonly neglected in depth-integrated flow models – may play an important role in the dynamics of levee-channelled debris-flows.

Within the flow head, material across the entire width of the flow is in motion, with the surface velocity close to the flow front almost uniformly $3\,\mathrm{m\,s^{-1}}$, about 50% faster than the propagation speed of the front. Away from the flow axis a transverse velocity component in the flow head, typically $\sim 0.75\,\mathrm{m\,s^{-1}}$, advects particles away from the axis and towards the flow margins. An animation of the surface speed of the runout from $t = 3.2$–$4.6\,\mathrm{s}$ is shown in movie 4. The characteristics of the channelised flow behind vary only slightly throughout that period, indicating that the velocities shown in figure 9 are typical of those in the regime of steady front propagation and levee formation.

4.1. Flow and deposition in a moving reference frame

The constant speed of propagation of the flow head and streamwise accretion of levees (figure 4*c*), together with the constant width and similarity of flow velocity profiles of the levee-channelled flow behind the head (figure 9*a*) indicate that the flow is best understood in a frame moving with the flow front, at the constant propagation speed of $2.0\,\mathrm{m\,s^{-1}}$. Figure 9(*b*) shows the surface velocity field at $t = 3.5\,\mathrm{s}$, in the frame moving at the speed of the front. In this reference frame, the velocity field is steady and the flow margins stationary, which implies that particle paths, such as those in figures 6*d* and 8*b*, coincide exactly with flow streamlines. In the moving frame, material moving downstream more slowly than the flow front, such as that in the levees and in the slowly moving outer parts of the leveed channel, appears to move 'backwards' away from the flow front, whereas material moving faster than the flow front, such as that in the channel centre, moves 'forwards' towards it. Movie 5 shows an overhead view of the runout in the frame moving with the flow front, in which the steady nature of the flow and the transport of material towards and away from the flow front can be seen. We emphasise that, as indicated in

figure 9(a), no material moves upstream in a stationary frame. The apparent movement of material 'backwards' in the moving frame simply reflects that slowly-moving or stationary material is left behind by the advancing flow front.

The correspondence of particle paths with streamlines in the moving frame means that the particles highlighted in figure 6, which each start at the same transverse distance from the flow axis, all follow the same streamline through the flow head. Accordingly, they are transported through the flow in the same manner, but are reversed in order as they migrate from the central channel (in which the flow is faster than the front propagation, or 'forwards' in figure 9b) to the levees (in which the flow is 'backwards' in figure 9b).

In figure 9b, streamlines originating close to the central flow axis follow a path through the head and intersect the flow boundary. Streamlines originating farther from the flow axis curve back on themselves (corresponding to the flow being slowed to below the propagation speed of the front) and connect to a levee. These two surface flow patterns are demarcated by a white dashed line, and correspond to the two behaviours identified in figure 8, where particles either reach the flow boundary and are overpassed by subsequent material, or remain on the surface as they are advected into the levees.

4.2. Three-dimensional flow model

Particle tracking directly yields only the surface velocity field. To understand the three-dimensional structure of the flow, we model the flow field mathematically and consider the effect of an assumed vertical velocity profile. Such profiles are difficult to measure experimentally, but some inferences about the internal velocity profile can be made from observations of the surface velocity field.

To make such inferences, a model is constructed in which the shape and velocity field of the flow are prescribed functions, which are chosen to closely match the observed debris-flows. Motivated by the experiments, the flow is assumed to be steady in the frame moving at the constant front speed u_F. We also assume that the compressibility of the debris-flow is negligible. This assumption is motivated by the near-incompressibility of both water and particle constituents of the debris-flows, and by the observation that the debris remains substantially water-saturated throughout the duration of the flow.

We use the coordinate system (x, y, z, t) (illustrated in figure 2) in the stationary frame, and (ξ, y, z) in a frame moving with the flow front, where x is the down-stream coordinate in the stationary frame, y is the cross-stream coordinate, z the slope-normal coordinate, t is time and $\xi = x - u_F t$ is the down-stream coordinate in the moving frame. The lack of a time coordinate in the frame moving with the flow front reflects the steady nature of the flow in this frame.

Denoting the flow velocity in the stationary frame by $\mathbf{u}(x, y, z, t) = (u, v, w)$, the assumption of incompressible flow implies that $\mathbf{u}$ is divergence-free

$$\frac{\partial u}{\partial x} + \frac{\partial v}{\partial y} + \frac{\partial w}{\partial z} = 0\,, \tag{1}$$

which places a strong restriction on the possible velocity fields.

In the stationary frame, the depth-averaged flow velocity $\bar{\mathbf{u}} = (\bar{u}, \bar{v})$ is defined by

$$\bar{u} = \frac{1}{h}\int_0^h u\,dz, \quad \bar{v} = \frac{1}{h}\int_0^h v\,dz\,. \tag{2}$$

The depth-averaged velocity is linked to the flow height by the depth-averaged mass balance equation

$$\frac{\partial h}{\partial t} + \frac{\partial}{\partial x}\left(h\bar{u}\right) + \frac{\partial}{\partial y}\left(h\bar{v}\right) = 0\,, \tag{3}$$

obtained by integrating (1) in z and applying kinematic boundary conditions at the surface and base of the flow. This depth-averaged mass balance equation is a key part of shallow-layer avalanche and debris-flow models [*Savage and Hutter*, 1989; *Gray et al.*, 1999; *Iverson and Denlinger*, 2001; *Gray et al.*, 2003]. In the moving frame, the flow is steady and (3) reduces to

$$\frac{\partial}{\partial \xi}\left(h\left(\bar{u}-u_F\right)\right)+\frac{\partial}{\partial y}\left(h\bar{v}\right)=0\,, \tag{4}$$

or, in the moving-frame depth-averaged velocities $\bar{u}'=\bar{u}-u_F$, $\bar{v}'=\bar{v}$,

$$\frac{\partial}{\partial \xi}\left(h\bar{u}'\right)+\frac{\partial}{\partial y}\left(h\bar{v}'\right)=0\,. \tag{5}$$

This divergence-free form allows a streamfunction ψ to be defined [e.g. *Batchelor*, 1967], which satisfies

$$\frac{\partial \psi}{\partial y}=h\bar{u}',\quad \frac{\partial \psi}{\partial x}=-h\bar{v}'\,. \tag{6}$$

We now construct empirical functions that approximate the flow's shape and velocity field. In plan-view, the flow boundary is described by $y=\pm y_0(\xi)$ (for $\xi\leq 0$), where

$$y_0(\xi)=W\sqrt{\tanh\left(-\frac{\xi}{W}\right)}\,, \tag{7}$$

is a function that represents the rounded front and constant width channel. The half-width of the debris flow is given by the constant W, here set to 1 m to match the width of experimental flows. The flow depth is similarly modelled by the function

$$h(\xi,y)=\frac{H}{W}\left(\frac{y_0^{2n}-y^{2n}}{y_0^{2n-1}}\right)\,, \tag{8}$$

where H is the maximum debris-flow depth of 25 cm and $n=4$ is a constant which reflects the observed height profile of the experimental debris-flows. The flow outline y_0 and depth h are illustrated in figure 10(a).

The depth-integrated flow velocity is constructed through (6) using an empirical stream-function

$$\psi(\xi, y) = \frac{HU}{W^2}\left(k y y_0^2 - \frac{k}{2n+1}\frac{y^{2n+1}}{y_0^{2n-2}} - \frac{1}{2m+1}\frac{y^{2m+1}}{y_0^{2m-2}} + \frac{1}{2n+2m+1}\frac{y^{2n+2m+1}}{y_0^{2n+2m-2}} \right), \tag{9}$$

where the constant $m = 2$ reflects the observed velocity field in the debris-flow head, and $k = (2n+1)/((2m+1)(2n+2m+1))$. The constant U scales the flow velocity, and is here set to $2.321\,\mathrm{m\,s^{-1}}$ in order to reproduce the experimentally observed front propagation speed of $2.0\,\mathrm{m\,s^{-1}}$. Contours of ψ, which are streamlines of the depth-integrated velocity field, are illustrated in figure 10(b).

To determine a three-dimensional velocity field $\mathbf{u}$ from the depth-integrated velocities $\bar{\mathbf{u}}$, the vertical velocity profile is required. We consider a single-parameter family of velocity profiles,

$$(u, v) = \bar{\mathbf{u}}\left(\alpha + 2(1-\alpha)\frac{z}{h}\right), \tag{10}$$

which are consistent with (2). The parameter α controls the amount of shear within the bulk of the flow compared to the amount of slip at the base. For physically realistic velocity profiles, $0 \le \alpha \le 1$: when $\alpha = 1$, $(u, v) = \bar{\mathbf{u}}$, and a plug-flow profile is produced; when $\alpha = 0$, $(u, v) = 2\bar{\mathbf{u}}\hat{z}/h$ and there is linear shear with depth throughout the flow, and no basal slip.

The flow velocity in the frame moving with the flow front, denoted by $\mathbf{u}'(\xi, y, z) = (u', v', w')$, is defined by $\mathbf{u}' = \mathbf{u} - (u_F, 0, 0)$. The horizontal components of the velocity in

the moving frame are then

$$u' = -u_F + (\bar{\mathbf{u}}' + u_F)\left(\alpha + 2(1-\alpha)\frac{z}{h}\right), \tag{11}$$

$$v' = \bar{\mathbf{v}}'\left(\alpha + 2(1-\alpha)\frac{z}{h}\right). \tag{12}$$

The vertical component of velocity is obtained by integrating the mass conservation equation in the moving frame with respect to z,

$$w'(\xi, y, z) = \int_0^z \frac{\partial u'}{\partial \xi} + \frac{\partial v'}{\partial y}\, dz', \tag{13}$$

which evaluates to

$$w' = u_F(1-\alpha)\frac{z^2}{h^2}\frac{\partial h}{\partial \xi} - (\nabla \cdot \bar{\mathbf{u}}')\left(\alpha + 2(1-\alpha)\frac{z}{h}\right) z\,. \tag{14}$$

The motion of a particle through this velocity field is given by

$$\frac{dr_x}{dt} = u\,, \quad \frac{dr_y}{dt} = v\,, \quad \frac{dr_z}{dt} = w\,, \tag{15}$$

where $\mathbf{r} = (r_x, r_y, r_z)$ is the particle location. As before, in the frame moving with the flow front, these particle paths coincide with streamlines of the three-dimensional flow.

Figure 11 shows streamlines of the model debris flow for three different vertical velocity profiles that satisfy (10), varying from plug-flow ($\alpha = 1$) to uniform simple shear ($\alpha = 0$). The three rows of plots show the assumed vertical velocity profiles, the surface velocities in the stationary frame and surface streamlines (particle paths) in the frame moving with the flow front. The surface velocities shown in the second and third columns are directly comparable with the experimentally measured surface velocities shown in figure 9(a) and 9(b), respectively.

The simplest velocity profile is that of uniform plug-flow, shown in figure 11(a, b, c), in which the flow moves entirely by basal slip. In this case, the flow in the x–y plane is

equal to the depth-averaged flow velocity everywhere. As a result, the surface streamlines in 11(c) coincide with those in figure 10(a) and do not intersect the frontal boundary of the flow. No surface material is transported to the front and overpassed, and the surface velocity at the flow front is identical to the rate of flow propagation. This is qualitatively unlike the experimental surface velocity field shown in figure 9(b).

Another possible flow profile is uniform simple shear, illustrated in figure 11(d, e, f). In this case the flow has a linear velocity gradient with no basal slip. Almost all the surface streamlines in this case intersect the frontal boundary of the flow, corresponding to almost all the surface material dropping over the front and being buried, rather than being advected into the levee surfaces. Again, this behaviour is unlike that in the experimental debris flows.

Figure 11(g, h, i) shows a velocity profile for $\alpha = 0.5$ that exhibits shear as well as some basal slip. The value of α is chosen to match the experimental observation that the surface velocity at the flow front is 50% faster than the front propagation rate. The surface streamlines in this case (figure 11i) closely resemble those observed in the experimental flow; surface streamlines near the centre of the channel reach the front, but towards the edges of the channel surface streamlines remain on the surface and are returned into the levees. We conclude that vertical shear is present in the experimental debris flows, combined with some component of basal slip or a rapidly-shearing boundary layer at the flow base, leading to a velocity profile similar to that depicted in figure 11(b). Direct evidence of shear in the flow is provided also by video recordings of the advancing flow front, which show particles and tracer cubes on the flow surface being advected over the flow front and buried by the subsequent flow.

The effect of the vertical velocity profile on the three-dimensional transport of material through the flow head is shown in figure 12. The green shaded areas indicate the regions at the back of the flow head where material moves more slowly than the flow front (that is, where u' is negative). In the moving frame, this condition corresponds to the regions where material leaves the flow head. Conversely, the area shaded pink represents the region where material enters the flow head. The curved lines show solutions of the transport equation (15), which are the paths taken by particles that enter the head in the region shaded pink, flow through it, and leave it in the region shaded green. The incompressible and steady nature of the flow in the moving frame implies that the mass flux entering the head exactly matches the mass flux leaving it. This mass balance has important consequences for the particle size-distribution in the flow head, and is discussed further in section 7.1.

In figure 12a and in movie 6, the three-dimensional particle paths are shown for the case of uniform plug flow. Material enters the head along the central axis of the flow, is advected outwards, and leaves along the flow margins. It can be shown from (14) and (15) that when there is no vertical shear, the relative height of a particle in the flow $\mathbf{r}_z/h$ remains constant.

In the case of simple shear, shown in figure 12b and in movie 7, material enters the head largely along the surface of the flow and leaves it in a layer at the base. There is very little transverse transport of particles, but instead they are advected over the flow front and to the base of the flow in a 'caterpillar-track' motion. The thick black line indicates the boundary between surface material which passes over the flow front and that which remains on the surface; in the case of plug flow (a), all particles initially on the surface remain there, and there is no overpassing of material.

Figure 12*c* and movie 8 show a combination of shear and basal slip, as inferred from the debris-flow experiments. The particle paths reflect a combination of transverse motion away from the flow centreline and vertical transport of particles from near the surface of the flow to near the base, through passing over the flow front. Material leaves the flow head predominantly in two lateral levees, but also in a thin layer at the base of the flow. In the stationary frame this material leaving the head is the slowest-moving in the flow, indicating that it may deposit readily.

5. Deposit Granulometry

Grain-size distributions were sampled from initial charges and along four transects in the August 25th and August 27th deposits (figures 13, 14 and 15). Three transverse transects and one axial transect each comprised three to six sample sites. At each sample site, a thin-walled steel tube 19 cm in diameter was inserted into the deposit and the material within it carefully excavated either from the top and bottom halves of the deposit (in the August 25th deposit), or from the top, middle and bottom thirds (in that of August 27th).

Sieve analyses yielded measures of dry mass in nine one-ϕ bins (each containing grains with effective diameters varying over a factor of two) between 0.0625 mm (1/16 mm) and 32 mm, and in one bin for particles smaller than 0.0625 mm. In order to highlight the evolved grain-size distributions that result from granular segregation, we normalise the deposit granulometric results against the granulometry of the initial charge in the hopper. For each experiment, the grain-size distribution of the initial charge is taken to be the unweighted mean of the grain-size distributions of the four samples taken in the hopper. To normalise a sample, the proportion of dry mass in each size bin is divided

by the corresponding proportion in the mean initial charge grain-size distribution. Figure 13 depicts the mean initial charge histograms for both experiments (*a* and *b*), and the relative abundance plot showing the grain-size distribution of the August 27th initial charge normalised against that of the August 25th experiment (*c*). The range of the vertical scale is from 0 (complete depletion) to 2.5 times enrichment relative to the initial charge. The initial charges of both experiments are bimodal, with peaks at ∼0.3 mm and ∼12 mm corresponding to the constituent sand and gravel components respectively. The initial charges from the two experiments are generally similar (that is, the relative abundances are close to unity), although the 4–8 mm particles are roughly doubled in abundance in the August 27th charge (∼12% as opposed to ∼6%).

In addition to using the initial charge grain-size distribution as a base for the normalisation, the mean grain-size distribution shown by [*Iverson et al.*, 2010, figure 5*a*], calculated from 20 samples of the same sand and gravel mixture, was also used as a normalisation base. This mean distribution is close to the bimodal distribution of the initial charges in our experiments, though it has a somewhat smaller proportion of the largest clasts (16–32 mm). Similar relative enrichment and depletion patterns are found if samples are normalised against this alternative particle-size distribution.

The relative abundance plots in figures 14 and 15 show that in general there is coherence across a range of neighbouring size bins, such that it seems justified to discuss three general classes of grains. We distinguish: *coarse* particles, from 8–32 mm; *fine* particles, from 0.0625–8 mm; and *very fine* particles, < 0.0625 mm. The coarse and fine fractions correspond generally, but not exactly, to the two peaks of the bimodal particle-size distribution of the initial charge (figure 13); the smallest gravel particles (of diameter 2–8 mm)

segregate in the same manner as the sand and so are classified as fine. The very fine particles comprise less than 2% of the initial charge, so we concentrate on the relative abundances of the coarse and fine classes. The settling velocity of the very fine particles is $\leq 3.2\,\mathrm{mm\,s^{-1}}$. We infer that this very fine fraction is strongly coupled with, and advected by, the water and that it does not play a significant role in the granular segregation that is marked within the flume and continues in the runout reach. The same inference was made by *Iverson* [1997]. In our experiments we diverted most of the trailing watery flow. Water laden with very fine particles may, however, have influenced flow mobility via elevated basal pore-fluid pressure just behind the head of the flow in the flume [*Iverson et al.*, 2010]. Video of the debris flow deposition viewed from above shows a late appearance of a watery surface layer (visible as light brown sediment in movie 2), which at least in part relates to pore-water expulsion. We infer that some of the relative enrichment in very fine sediment in uppermost layers (for example in figure 14, sample sites 13–15) results from its elutriation upwards with expelled pore-water [*Kim and Lowe*, 2004].

The August 25th deposit (figure 14), in the proximal transect at $x = 3\,\mathrm{m}$, exhibits a strongly enriched concentration of coarse material and depletion of fine, to approximately half of its initial concentration, throughout the outer parts of the levees (sample sites 1 and 4). At the centre of the leveed channel (site 3), the size distribution is closer to that of the source material, with a consistent relative depletion of the largest particles ($d > 16\,\mathrm{mm}$); no overall size grading is evident. At site 2, the basal enrichment of coarse and depletion of fine is taken to reflect the inner low flank of the levee. These relationships are evident in the medial transect, at $x = 7\,\mathrm{m}$, although the enrichment of coarse material in the levees (sites 5, 6, 9 and 10) is less marked than in the proximal

transect. The samples from the centre of the channel (sites 7 and 8) show slight coarse material depletion but otherwise little deviation from the source material composition. In the transect at $x = 10\,\mathrm{m}$, the levees (sites 11, 12, 16 and 17) are again distinguished by some relative enrichment of coarse and depletion of fine throughout, but in the centre (sites 13–15) there is also some depletion of fines, as there is in the longitudinal transect to the front (sites 18–21). Overall, the August 25th deposit shows a proximal to distal progressive loss of the coarsest particles (16–32 mm).

The August 27th deposit was sampled at three levels at each site, but only at the centre and along transects through one levee (figure 15). The levee samples (sites 22, 25 and 28) exhibit strong relative enrichment of coarse particles and corresponding depletion of fine ones. These also show a vertical organisation in which the relative enrichment of the coarsest particles is most marked at the top and bottom, with less enrichment in the middle. Samples nearer the deposit axis at $x = 2\,\mathrm{m}$ and $x = 6.5\,\mathrm{m}$ (sites 23 and 26) intersect levee material in the lower two thirds and at both of these sites the overall vertical organisation is normal (coarse-tail) grading. At the centre of the leveed channel in these transects, the deposits (sites 24 and 27) show slight coarse depletion but otherwise no strong or consistent departures from the source material concentrations of coarse and fine particles.

6. Coarse Tracer Pebbles

In the August 27th experiment, $\sim$600 pebbles with average diameter of $\sim$20 mm, typical of the largest particles in the initial charge, were painted white and placed in a rectangular patch no more than one particle thick on the runout area, 2 m from the exit of the flume, shown in figure 2. The objective of this part of the experiment was to illustrate the fate

of the coarse particles that pass over the flow front and become buried as it advances. As the debris-flow front advanced over the tracer pebbles, they were incorporated into the buried material, and thereafter reflected the paths of those large particles which reached the flow front and were overpassed at $x \approx 2\,\mathrm{m}$. The deposit was gradually removed by trowel, so as to reveal the plan-view position and (in some cases) height of the pebbles, which were recorded (figure 16).

The tracer pebbles occupied a wishbone shaped region in the deposit, becoming progressively elevated and dispersed throughout the deposit down-stream. Within 3 m of the pick-up area (the blue rectangle in figure 16) pebbles were clustered in two parallel bands along the inner sides of the levees, with numerous pebbles $\geq 5\,\mathrm{cm}$ above the deposit base $\sim 2\,\mathrm{m}$ from source and with a complete absence of pebbles in the centre of the channel. Beyond $\sim 3\,\mathrm{m}$ from source many pebbles were elevated $\leq 12\,\mathrm{cm}$ above the deposit base, mainly in a broad zone centred on the flow axis, with few pebbles within 0.5 m of the deposit margin. The height attained by the tracer pebbles shows a clear increase with downstream distance, most marked between 3.5 m and 5 m downstream from the flume exit (1.5–3 m from the pick-up area), where particles are positioned up to 15 cm above the base. This positioning reflects a maximum rise of 15 cm in $\sim 2.7\,\mathrm{m}$ of transport, or a streamwise climb angle of $\sim 3°$.

The increase in elevation provides evidence for size-segregation during runout of the debris flow. The possibility that the stones reached a pre-existing deposited region, and were then raised above the runout pad through 'ramping' (rolling up the inclined surface of a deposited region), is not consistent with the path of the tracer pebbles through the flow head, from their introduction at the flow front to deposition in the progressively accreting

levees. The typical rise velocity of the segregating pebbles can only be estimated, since the time of deposition of particles in the interior of the flow is not known. However, there is evidence (in section 3) that deposition of levees occurs rapidly throughout the flow depth, and so the deposition time of particles in the levees is close to the stopping time of the surface material at that point. The tracer pebbles were over-run between $t = 1.1$ s and $t = 1.5$ s, and the deposition of the levee surface at $x = 5$ m, where particles reached 15 cm above the base, occurred at $t = 3.5$ s. This indicates a maximum rise rate of 6.3–7.5 $\mathrm{cm\,s^{-1}}$. Tracer pebbles in the levee near $x = 5$ m were distributed quite uniformly between ground level and 15 cm above the runout pad; a typical rise rate is therefore half this, $\sim 3.5\ \mathrm{cm\,s^{-1}}$.

Between 5 m and 8.8 m downstream, where the most distal tracer pebble was located, the pebbles were distributed approximately uniformly in height within the bottom two-thirds of the deposit, ≤ 17 cm above the base. No tracers occurred in the uppermost 5 cm of the deposit and very few within 10 cm of the top surface. This distribution is illustrated in figure 17, which shows the deposit of the 27th August experiment, with ~ 5 cm of material excavated from a sector of the flow. Two white tracer pebbles, the closest to the surface in this section of the deposit, are visible on the surface of the excavation. To the left of the photograph, a transect through the deposit at $x = 7$ m shows a scattered distribution of tracer pebbles in the lower part of the flow, as illustrated in figure 16.

7. Segregation and Recirculation

The combined occurrence during the runout of particle size-segregation, vertical shear and overpassing of material at the flow front leads to a net transport of coarse and fine

particles to different locations in the flow and deposit. We now combine the velocity field of the flume runout inferred in section 4.2 with a simple model for bidisperse particle segregation proposed by *Gray and Thornton* [2005] to predict the distribution of large and small particles throughout the flow. We relate this distribution to observed grain-size distributions sampled from the deposit. While the bidisperse model describes the segregation of only two species of particle, the experimental debris-flows contain a continuous range of particle sizes. However, the bimodal distribution of the initial charge and the coherence of enrichment or depletion across neighbouring size bins suggests that this bidisperse segregation model may be applied to the flume runout, with coarse (8–32 mm) and fine (0.0125–8 mm) volume fractions corresponding to large and small fractions respectively.

The particle segregation and transport model of *Gray and Thornton* [2005] describes the time-evolution of the small-particle volume fraction ϕ^s in an incompressible bidisperse granular flow. The model equation can be written as

$$\frac{\partial \phi^s}{\partial t} + \frac{\partial}{\partial x}\left(\phi^s u\right) + \frac{\partial}{\partial y}\left(\phi^s v\right) + \frac{\partial}{\partial z}\left(\phi^s \left[w - q(1-\phi^s)\right]\right) = 0\,, \tag{16}$$

where $\mathbf{u} = (u, v, w)$ is the prescribed bulk flow velocity field, q is the (positive) segregation speed and $\mathbf{k}$ the unit normal vector in the positive z-direction. The bracketed term $w - q(1-\phi^s)$ corresponds to the vertical velocity of small particles. When $q = 0$ this term reduces to the bulk vertical velocity and the equation reduces to the tracer equation. In the case $\phi^s = 0$ the vertical velocity is simply $w - q$, representing a small particle descending through a bulk flow of pure large particles at a speed q. In this bidisperse model the large-particle volume fraction is simply equal to $\phi^l = 1 - \phi^s$, and (16) can be

rewritten in terms of this variable as

$$\frac{\partial \phi^l}{\partial t} + \frac{\partial}{\partial x}\left(\phi^l u\right) + \frac{\partial}{\partial y}\left(\phi^l v\right) + \frac{\partial}{\partial z}\left(\phi^l \left[w + q(1-\phi^l)\right]\right) = 0\,. \tag{17}$$

The corresponding vertical velocity of large particles $w + q(1 - \phi^l)$ is equal to the bulk vertical velocity if $q = 0$. The case $\phi^l = 0$ represents a large particle rising through the bulk flow of pure small particles at speed q.

Gray and Thornton [2005] show that this model predicts that the rise of large particles eventually leads to a surface layer of pure large particles, separated from pure small particles beneath by a sharp interface (a hyperbolic shock in particle number density). When combined with a shearing flow in which material at the surface moves faster than that at the base, this layered structure leads to enhanced transport of large material towards the front of the flow. *Gray and Ancey* [2009] consider the implications of this transport on the distribution of large and small particles in a two-dimensional granular avalanche. They show that the segregation model of predicts an accumulation of large particles at the flow front, which is separated from the flow behind by a lens-shaped region of mixed large and small particles known as a breaking size-segregation wave [*Thornton and Gray*, 2008]. The segregation occurring within the breaking size-segregation wave causes a recirculating region of large particles in the flow head, while small particles segregate downwards and are transported away from the front.

In real granular flows, large and small particles are rarely separated by a sharp interface owing to diffusive remixing, which acts to smooth the interface. This effect was added to the segregation model by *Gray and Chugunov* [2006]. While for simplicity we present the results below without diffusive remixing, the qualitative results are unchanged by the addition of small amounts of diffusion.

To close the model, the bulk velocity field and segregation rate within the flume runout are required; the bulk velocity field $\mathbf{u}$, with a vertical velocity profile corresponding to $\alpha = 0.5$, and a typical segregation rate of $0.035\,\mathrm{m\,s^{-1}}$ are inferred in sections 4.2 and 6 respectively.

We consider in particular the solution in the centre plane $y = 0$, indicated by black particle paths in figure 12. On this plane the transverse velocity v is zero, which means that y-derivatives of ϕ no longer appear in (16). The solution for ϕ on $y = 0$ therefore uncouples from the solution for $y \neq 0$, and (16) reduces to an equation in two spatial variables:

$$\frac{\partial \phi}{\partial t} + \frac{\partial}{\partial \xi}(u\phi) + \frac{\partial}{\partial z}\left(\phi\left[w - q(1-\phi)\right]\right) = -\phi\frac{\partial v}{\partial y}\,. \tag{18}$$

where u, w, q and $\partial v/\partial y$ are prescribed by the velocity field. The term on the right-hand side represents the flux of particles away from the flow centreline by the transverse velocity strain $\partial v/\partial y$. At the flow surface $z = h$ and base $z = 0$, the boundary condition on ϕ is that no flux of particles occurs across the flow boundary, which when no diffusive remixing occurs, implies that $\phi = 0$ or $\phi = 1$ [*Gray and Chugunov*, 2006, equation 2.24]. Far upstream of the front we assume that particles in the flow have segregated to form a layer of coarse material (taken to be 5 cm thick) on top of a layer of fine material.

Figure 18 shows the steady solution of the segregation equation (16) on the centre plane of the debris flow. In figure 18(a) the concentration ϕ^s is shown, with coarse-particle-enriched regions indicated by dark shading. The model predicts a pure coarse-particle layer on the surface of the runout, which 'wraps around' the advancing flow front and creates a coarse-particle region at the base of the flow which extends $\sim$0.8 m behind the front. In the interior of the flow, a roughly elliptical region of mixed coarse and

fine particles—a breaking size-segregation wave—extends from 0.3 m to 3.7 m behind the front. The coarse-rich front and surface layer, and breaking size-segregation wave resemble those found by *Gray and Ancey* [2009] for a two-dimensional avalanche.

Figure 18(b) shows the model particle paths, which provide an explanation for the distribution of coarse and fine particles observed in the experiments. As in section 4.2, vertical shear means that material near the base of the flow moves more slowly than the advancing front, and so moves backwards in the moving frame. Correspondingly, material near the surface moves faster than the front and so is transported forwards. Coarse particles (indicated by black lines) at the flow surface are transported forwards and descend the rounded front of the flow to reach the base. Here they are overpassed and are transported back away from the front, forming the coarse-particle layer at the flow base. As these coarse particles begin to re-segregate up through the flow, material at the flow base transitions from coarse-enriched near the front to coarse-depleted farther upstream. As the rising coarse particles reach the upper part of the flow, they are again transported towards the flow front, but their segregation is stopped before they reach the flow surface by the coarse layer of particles occupying the top ~ 5 cm of the flow. The coarse-enriched surface layer effectively acts as a lid, preventing further particles from segregating.

We consider the particle size-distributions measured on the centre plane of the August 27th deposit, and compare these to the coarse and fine particle concentrations predicted by the model and shown in figure 18(a). A direct comparison between these predictions and the observed deposit cannot be made, since the model predicts particle concentrations not in the deposit but in the steady-state flow regime. The particle-size distribution in

the deposit will correspond to that in the flow only if the flow ceased motion everywhere instantaneously, 'freezing' the size distribution into the deposit. In the central channel, deposition at the flow surface occurred rapidly across the streamwise length of the runout (figure 4*c*), but it is quite possible that progressive vertical aggradation occurred along the centreline in the latter stages of the runout. As a consequence, features near the flow base that were deposited before the runout ceased will be observed farther upstream in the deposit than in the steady-state flow prediction.

Figure 19 shows the relative particle abundance plots for sites along the central axis of the deposit. At sites 31 and 32, 1.25 m and 0.55 m upstream of the deposit termination, coarse material is enriched both at the surface and base of the deposit, with no evidence of such enrichment at samples taken from the middle of the deposit. This pattern is consistent with the surface and basal layers of coarse enrichment predicted by the segregation model at $\xi = -0.55$ m and $\xi = -1.25$ m (figure 18*a*). At site 32, 0.55 m upstream from the deposit termination, there is a strong contrast between coarse-enriched top and bottom samples and the middle sample which shows no such enrichment, despite the deposit thickness being only 15 cm. This evidence implies that the thickness of the coarse-enriched layer is no larger than 5 cm, or approximately three coarse-particle diameters.

In contrast to the surface samples at sites 31 and 32 (≤ 1.25 m upstream of the deposit termination), the surface samples at sites 24, 27 and 30 (8–2.5 m from the termination) indicate lesser or no coarse enrichment. After the flow diverter was brought down, the final surface particles to pass under it reached $x = 7.5$ m on the deposit axis, approximately 2.5 m upstream of the deposit termination. The coarse-depleted material at the deposit surface upstream of this at locations 24, 27 and 30 therefore represents a combination of

material beneath the flow surface which was revealed when the flow continued to shear down-stream following the deployment of the flow diverter, and of debris which encroached under the diverter itself. The top samples at sites 31 and 32 indicate the composition of the flow surface prior to the application of the diverter, and their strong coarse enrichment is consistent with a coarse layer covering the flow surface during the runout.

At the base of the deposit, coarse particles are enriched at samples 31–32, within 2.5 m from the deposit termination, and coarse-depleted farther upstream. The most strongly enriched base sample is the farthest-downstream at site 32, which reflects the re-segregation of the basal coarse-particle layer up through the flow as material at the base travels away from the front. By 4 m upstream of the front, at site 27, segregation lifted coarse particles completely out of the basal layer, which is not coarse-enriched.

The path of the coarse particles forming a basal layer at the front of the flow was measured directly in the experimental debris flows with the large tracer pebbles, which were representative coarse particles introduced into the flow at the base of the flow front. The observed rise of these pebbles to a maximum height of 5–10 cm below the deposit surface is consistent with the upward movement of coarse particles in figure 18(b), with the halting of segregation by the overlying coarse-particle layer approximately 5 cm below the flow surface.

7.1. Discussion: coarse-particle mass balance

In the three-dimensional debris-flow velocity field calculated in section 4.2, the mass fluxes entering and leaving the flow head were equal, due to the flow being incompressible and steady in the moving frame. The segregation model captures an important additional characteristic of the debris-flow runout: that the fluxes of both coarse or fine particles

entering a region must each be balanced by a corresponding flux of coarse or fine particles leaving that region. Figure 18(b) shows that along the centre-plane, upstream of the flow head, the flow has three distinct layers: at the surface, coarse particles are advected towards the flow front; beneath these, fine particles are advected towards the flow front; and at the flow base, fine particles are advected away from the flow front. In the centre-plane the fluxes in these three layers result in a net flux of material towards the flow front, which is removed from the centre-plane by the transverse flux $-\phi\partial v/\partial y$. These fluxes can be calculated from the solution of the segregation equations plotted in figure 18. Of the fine material transported towards the front in the middle of the flow centre-plane, 68% descends to the base of the flow and flows away from the head, following the dashed white lines in figure 18(b). The remainder of the fine material, and all of the coarse surface material transported to the flow front are removed from the centre-plane by transverse strain of the flow velocity field. The composition of material leaving the centre-plane through transverse shear is 78% coarse. This percentage represents a substantial coarse enrichment from the inflow flux, which is 28% coarse. In summary, the model shows that of the material transported into the flow head, fine particles mostly leave the head at the base of the central channel, whereas coarse particles are transported outwards in a transverse direction.

If the particle fluxes into and out of a flow region do not balance, a steady solution to the segregation equation cannot exist, and the volume fraction of coarse and fine material within the flow evolves with time. This unsteady state occurs if the inflow flux of particles is sufficiently coarse-enriched that the flux of coarse particles entering the flow head is greater than that which can leave the head through transverse motion. In this situation,

the segregation equation predicts that the flow head is composed of pure coarse particles, with the downstream length of the coarse-particle head growing in time. This solution neglects the feedback of such a coarse-particle-enriched head on the bulk velocity field; in natural debris flows, the growing resistance to flow of the coarse-enriched head is likely to slow and block the flow behind [*Iverson*, 1997; *Major and Iverson*, 1999]. This blockage is likely to either halt the flow, or to cause a breakout of the channelised flow through existing emplaced levees, or the splitting of a single leveed channel into two. The formation of fingered deposits with a lobe-and-cleft morphology, as compared to elongated leveed channel deposits, may therefore indicate a greater flux of coarse levee-forming clasts to the flow front.

The formation of either a steady or a growing coarse-particle head has also been observed in solutions of the segregation model in two-dimensional avalanches [*Gray and Ancey*, 2009]. The avalanches studied by *Gray and Ancey* are similar to those considered here in that they have a rounded flow front, are steady in a frame moving with the propagation speed of the front, and have vertical shear which leads to the enhanced transport of a coarse surface-layer towards the flow front. However in a two-dimensional avalanche, the flow considered by [*Gray and Ancey*, 2009] is uniform in the transverse direction, implying that there is no transverse flux of material out of the flow head (that is, that $\partial v/\partial y = 0$). *Gray and Ancey* [2009] find that the enhanced transport of coarse material in the surface-layer to the flow front, without a corresponding flux of coarse particles away from the front, results in a growing coarse-particle head at the flow front. This mechanism for the formation of coarse-particle fronts is purely kinematic, and is captured by the depth-integrated size segregation model of *Gray and Kokelaar* [2010].

In the small-scale two-dimensional avalanche experiments of *Gray and Ancey* [2009], a coarse-particle layer is deposited at the flow base. Motivated by this, *Gray and Ancey* added deposition to the model and demonstrated that the resulting flux of (deposited) coarse particles out of the head at the base of the flow allows a steady solution to be found, analogous to the way in which the transverse flux of coarse material out of the head allows a steady solution in a three-dimensional avalanche. The large-scale debris-flow experiments described in this paper indicate that in an unconfined debris-flow, the primary deposition of coarse particles is in lateral levees, rather than at the flow base.

The solutions to the segregation equation in a shearing granular avalanche, both in the two-dimensional depositing flow of *Gray and Ancey* [2009] and in the centre-plane of the three-dimensional solution presented here, contain a breaking size-segregation wave close to the flow front. *Gray and Ancey* [2009] show that in two dimensions, large particles recirculate within this breaking size-segregation wave, following closed streamlines. In the three-dimensional velocity field, figure 18(b) indicates that the coarse particles instead spiral inwards to a stagnation point within the breaking size-segregation wave where coarse particles on the centreline become stationary in the moving frame. In this region, the outward-directed transverse velocity components advect material which is not exactly on the flow centre-plane out towards the flow margins.

8. Conclusion

Coarse-particle-rich levees formed in our debris-flow experiments by rapid progressive streamwise accretion. A model for their formation includes both upward segregation of coarse particles and shear within the flow, which cause enhanced transport of coarse

material to the flow front. A diverging transverse velocity field in the head then transports this coarse material to the flow margins, where it deposits as a levee.

Each stage in the levee-formation process was directly observed in our experiments. Size-segregation was measured using coarse tracer particles, which rise at a typical rate of $3.5\,\mathrm{cm\,s^{-1}}$, about 1% of the typical speed of the channelised flow, $\sim 4\,\mathrm{m\,s^{-1}}$. This segregation rate is sufficient, even within the short duration of the experimental flows, to result in a substantial coarse enrichment of the upper part of the flow. Vertical shear within the flow was inferred from measurements of the surface velocity field and front propagation rate, and supported by direct observations of surface particles being advected to the advancing flow margin and transferred to the base of the flow. The surface velocity field (figure 9) demonstrates that the lateral transport of material from the central channel into the levees occurs entirely within the flow head.

Figure 20 shows a sketch of a typical trajectory of a coarse particle through the flow, summarising the mechanisms present in the formation of coarse-particle-rich levees. Particle size-segregation causes a coarse particle in the channel to rise to near the flow surface, where vertical shear transports it to the flow head. If the particle is sufficiently close to the flow axis (as shown in figure 8) it reaches the flow front, where it is transported to the base of the flow and overpassed. The particle again segregates upwards until it reaches the coarse-enriched layer covering the flow surface, then recirculates within the flow head. During recirculation, material is advected away from the flow centre-plane by the transverse component of the velocity. In the moving frame, coarse particles therefore follow helical spiral trajectories within the flow head and move progressively farther towards the flow margins; this path is sketched in figure 20. Near the flow margins, particles

throughout the depth of the flow move more slowly than the flow front (as indicated by the green shading in figure 12). When a coarse particle is advected into this region, it ceases recirculation and is transported back away from the flow front. As it moves out of the flow head, the particle reaches the deposition surface of the progressively-accreting levee and comes to rest.

The mechanisms governing this motion of the coarse particles through the flow head to form coarse-enriched levees have been demonstrated in debris flow experiments, but are generic to a wide variety of geophysical and grain flows. The kinematic nature of the model presented here means that it depends only on particle size-segregation and the flow velocity field. It therefore has the potential to describe the formation of coarse-particle levees in debris flows, pyroclastic density currents [*Branney and Kokelaar*, 2002; *Félix and Thomas*, 2004] and snow avalanches [*Gray and Kokelaar*, 2010], despite the wide variety of mechanisms that govern the complex and spatially-varying rheology of these flows [*Iverson and Vallance*, 2001].

Acknowledgments. Chris Johnson acknowledges support from NERC DTG NE/G523747/1 and an EPSRC DTA. Nico Gray, Peter Kokelaar and Anthony Thornton were supported by NERC grant NE/E003206/1, and Nico Gray additionally by an EPSRC Advanced Research Fellowship (GR/S50052/01 and GR/S50069/01).

References

Bagnold, R. A. (1954), Experiments on a gravity-free dispersion of large solid spheres in a Newtonian fluid under shear, *Proc. R. Soc. A*, *225*(1160), 49–63.

Batchelor, G. K. (1967), *An introduction to fluid dynamics*, Cambridge Univ. Press.

Branney, M. J., and B. P. Kokelaar (2002), *Pyroclastic density currents and the sedimentation of ignimbrites*, Geological Soc. Publishing House.

Conway, S. J., A. Decaulne, M. R. Balme, J. B. Murray, and M. C. Towner (2010), A new approach to estimating hazard posed by debris flows in the Westfjords of Iceland, *Geomorphology*, *114*(4), 556–572.

Félix, G., and N. Thomas (2004), Relation between dry granular flow regimes and morphology of deposits: formation of levées in pyroclastic deposits, *Earth Planet. Sci. Lett.*, *221*(1-4), 197–213.

Gray, J. M. N. T., and C. Ancey (2009), Segregation, recirculation and deposition of coarse particles near two-dimensional avalanche fronts, *J. Fluid Mech.*, *629*, 387–423.

Gray, J. M. N. T., and V. A. Chugunov (2006), Particle-size segregation and diffusive remixing in shallow granular avalanches, *J. Fluid Mech.*, *569*, 365–398.

Gray, J. M. N. T., and B. P. Kokelaar (2010), Large particle segregation, transport and accumulation in granular free-surface flows, *J. Fluid Mech.*, *652*, 105–137.

Gray, J. M. N. T., and A. R. Thornton (2005), A theory for particle size segregation in shallow granular free-surface flows, *Proc. R. Soc. A*, *461*(2057), 1447–1473.

Gray, J. M. N. T., M. Wieland, and K. Hutter (1999), Free surface flow of cohesionless granular avalanches over complex basal topography, *Proc. R. Soc. A*, *455*(1985), 1841–1874.

Gray, J. M. N. T., Y. C. Tai, and S. Noelle (2003), Shock waves, dead zones and particle-free regions in rapid granular free-surface flows, *J. Fluid Mech.*, *491*, 161–181.

Heim, A. (1932), *Bergsturz und Menschenleben*, Fretz & Wasmuth, Zürich.

Iverson, R. M. (1997), The physics of debris flows, *Rev. Geophys.*, *35*(3), 245–296.

Iverson, R. M., and R. P. Denlinger (2001), Flow of variably fluidized granular masses across three-dimensional terrain: 1. Coulomb mixture theory, *J. Geophys. Res*, *106*(B1), 537–552.

Iverson, R. M., and J. W. Vallance (2001), New views of granular mass flows, *Geology*, *29*(2), 115.

Iverson, R. M., M. Logan, R. G. LaHusen, and M. Berti (2010), The perfect debris flow? Aggregated results from 28 large-scale experiments, *J. Geophys. Res.*, *115*(F3), F03,005.

Johnson, A. M. (1965), A model for debris flow, Ph.D. thesis, Pennsylvania State University.

Johnson, A. M. (1970), Physical processes in geology, *W. H. Freeman, New York*.

Johnson, A. M., and J. R. Rodine (1984), Debris flow, in *Slope instability*, edited by D. Brunsden and D. B. Prior, pp. 257–361, John Wiley, New York.

Kim, B. C., and D. R. Lowe (2004), Depositional processes of the gravelly debris flow deposits, South Dolomite alluvial fan, Owens Valley, California, *Geosci. J.*, *8*(2), 153–170.

Major, J. J. (1997), Depositional processes in large-scale debris-flow experiments, *J. Geol.*, *105*(3), 345–366.

Major, J. J., and R. M. Iverson (1999), Debris-flow deposition: Effects of pore-fluid pressure and friction concentrated at flow margins, *Geol. Soc. Am. Bull.*, *111*(10), 1424–1434.

Mangold, N., A. Mangeney, V. Migeon, V. Ansan, A. Lucas, D. Baratoux, and F. Bouchut (2010), Sinuous gullies on Mars: Frequency, distribution, and implications for flow properties, *J. Geophys. Res*, *115*, E11,001.

Middleton, G. V. (1970), Experimental studies related to problems of flysch sedimentation, *Flysch Sedimentology in North America*, pp. 253–272.

Middleton, G. V., and M. A. Hampton (1976), Subaqueous sediment transport and deposition by sediment gravity flows, in *Marine sediment transport and environmental management*, vol. 218, edited by D. J. Stanley and D. J. P. Swift, John Wiley, New York.

Pierson, T. (1986), Flow behavior of channelized debris flows, Mount St. Helens, Washington, in *Hillslope processes*, edited by A. D. Abrahams, pp. 269–296, Allan and Unwin.

Pouliquen, O., and J. W. Vallance (1999), Segregation induced instabilities of granular fronts, *Chaos*, *9*, 621.

Pouliquen, O., J. Delour, and S. B. Savage (1997), Fingering in granular flows, *Nature*, *386*, 816–817.

Savage, S. B., and K. Hutter (1989), The motion of a finite mass of granular material down a rough incline, *J. Fluid Mech.*, *199*, 177–215.

Savage, S. B., and C. K. K. Lun (1988), Particle size segregation in inclined chute flow of dry cohesionless granular solids, *J. Fluid Mech.*, *189*, 311–335.

Sharp, R. P., and L. Nobles (1953), Mudflow of 1941 at Wrightwood, southern California, *Geol. Soc. Am. Bull.*, *64*(5), 547–560.

Stiny, J. (1910), *Die Muren*, Verl. der Wagnerischen Univ.-Buchhandl. Innsbruck.

Thornton, A. R., and J. M. N. T. Gray (2008), Breaking size segregation waves and particle recirculation in granular avalanches, *J. Fluid Mech.*, *596*, 261–284.

Thornton, A. R., J. M. N. T. Gray, and A. J. Hogg (2006), A three-phase mixture theory for particle size segregation in shallow granular free-surface flows, *J. Fluid Mech.*, *550*,

1–25.

Vallance, J. W., and S. B. Savage (2000), Particle segregation in granular flows down chutes, in *IUTAM Symposium on Segregation in Granular Flows*, edited by A. D. Rosato and D. L. Blackmore, p. 31, Kluwer Academic Pub.

Figure 1. The USGS debris-flow flume, near Blue River, Oregon. This photo shows a debris flow $\sim$ 14 s after it has been released from the hopper (top centre). The head of the debris-flow has reached the runout pad at the bottom of the flume, and has coloured tracers on its surface which were dropped onto it as the flow exited the flume mouth. A wooden barricade, held above the flume mouth with the back-hoe of a tractor, allows the initial stages of the debris flow runout to pass beneath it unimpeded. The barricade is dropped across the flume mouth once the bulk of the flow has passed, diverting the watery flow 'tail'.

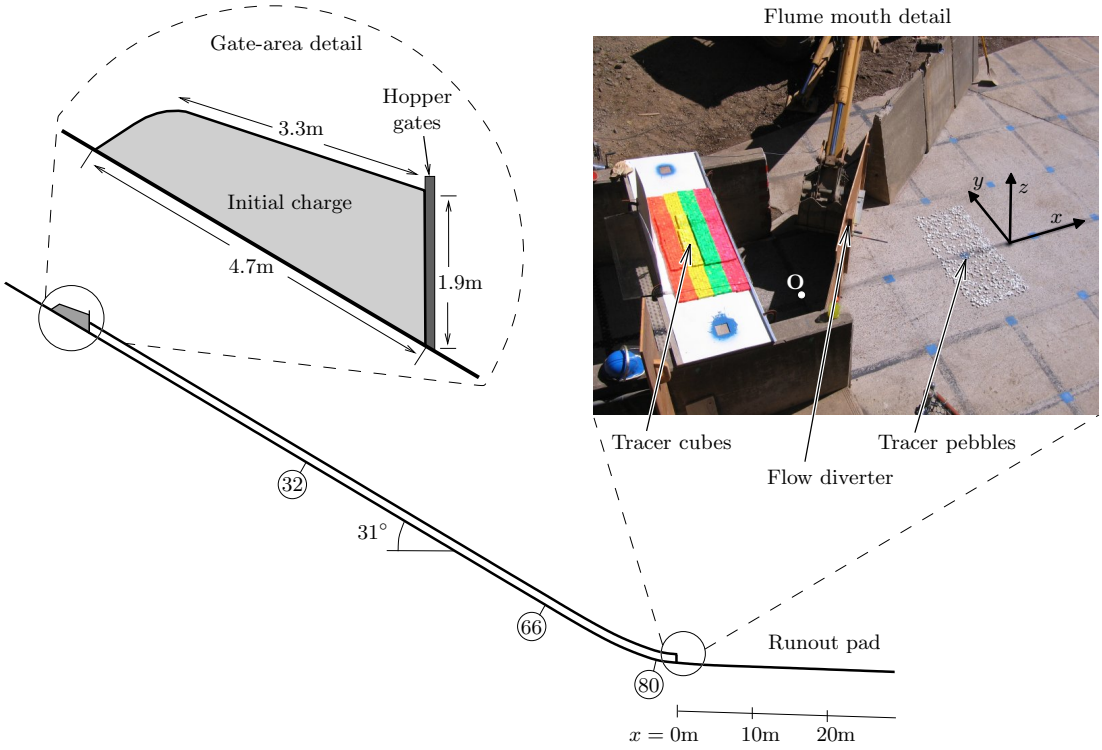

Figure 2. Longitudinal profile of the USGS debris-flow flume and runout pad, showing the location of the flow height, normal stress and pore pressure sensors, 32 m, 66 m and 80 m below the headgates. The left inset shows the shape of the initial 10 m^3 charge of sediment. The right inset is a photograph of the flume mouth area, showing the orientation of the xyz coordinate system. The origin O is located at on the surface of the runout pad, at the centre of the flume mouth.

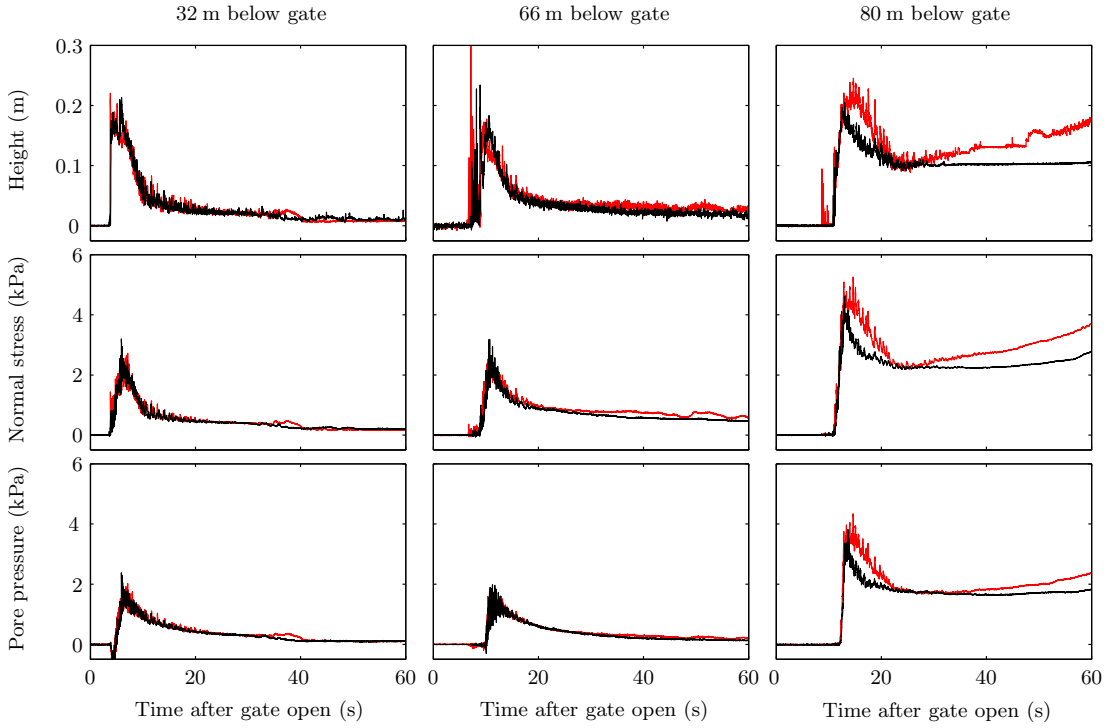

Figure 3. Flow depth, basal normal stress and basal pore pressure measurements for the experiments of 25th August (black) and 27th August (red). Measurements are taken at three locations: 32 m, 66 m and 80 m downslope of the headgates.

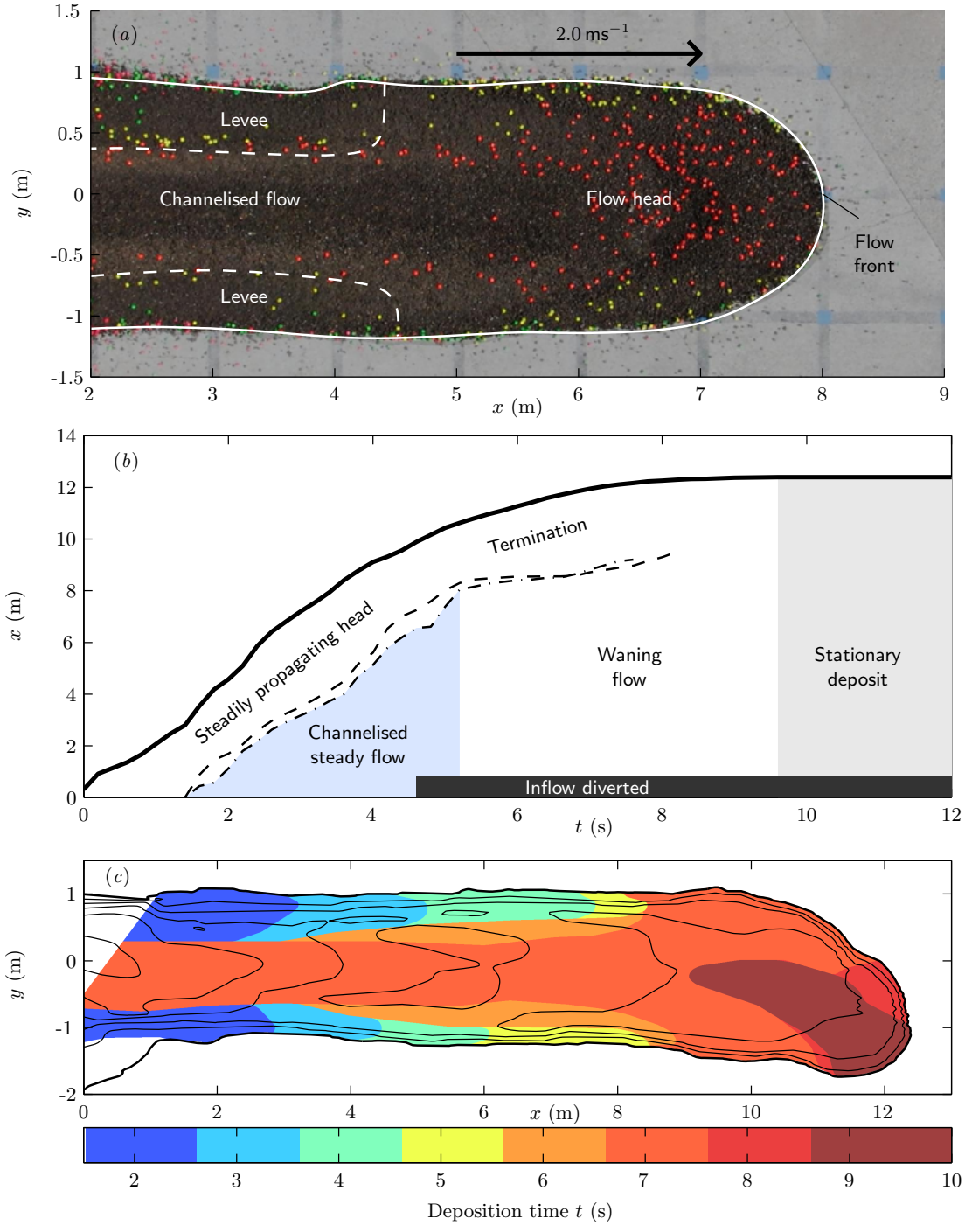

Figure 4. (*a*) Overhead view of the 25th August debris-flow runout, 3.5 s after it first reached the flume mouth. The main features are the flow head, which forms the distal 3.5 m of the flow, and a channelised flow bounded by stationary levees that extend back to the flume. The flow head propagates at a steady velocity of $\sim 2.0\,\mathrm{m\,s^{-1}}$, progressively extending the levees and the length of the channelised flow. (*b*) Downstream location of the flow front (solid line) and maximum downstream extents of left and right levees (dashed and dot-dashed lines respectively), as functions of time. (*c*) Timing of surface deposition, indicated by colour. Contours show deposit thickness, with 5 cm spacing.

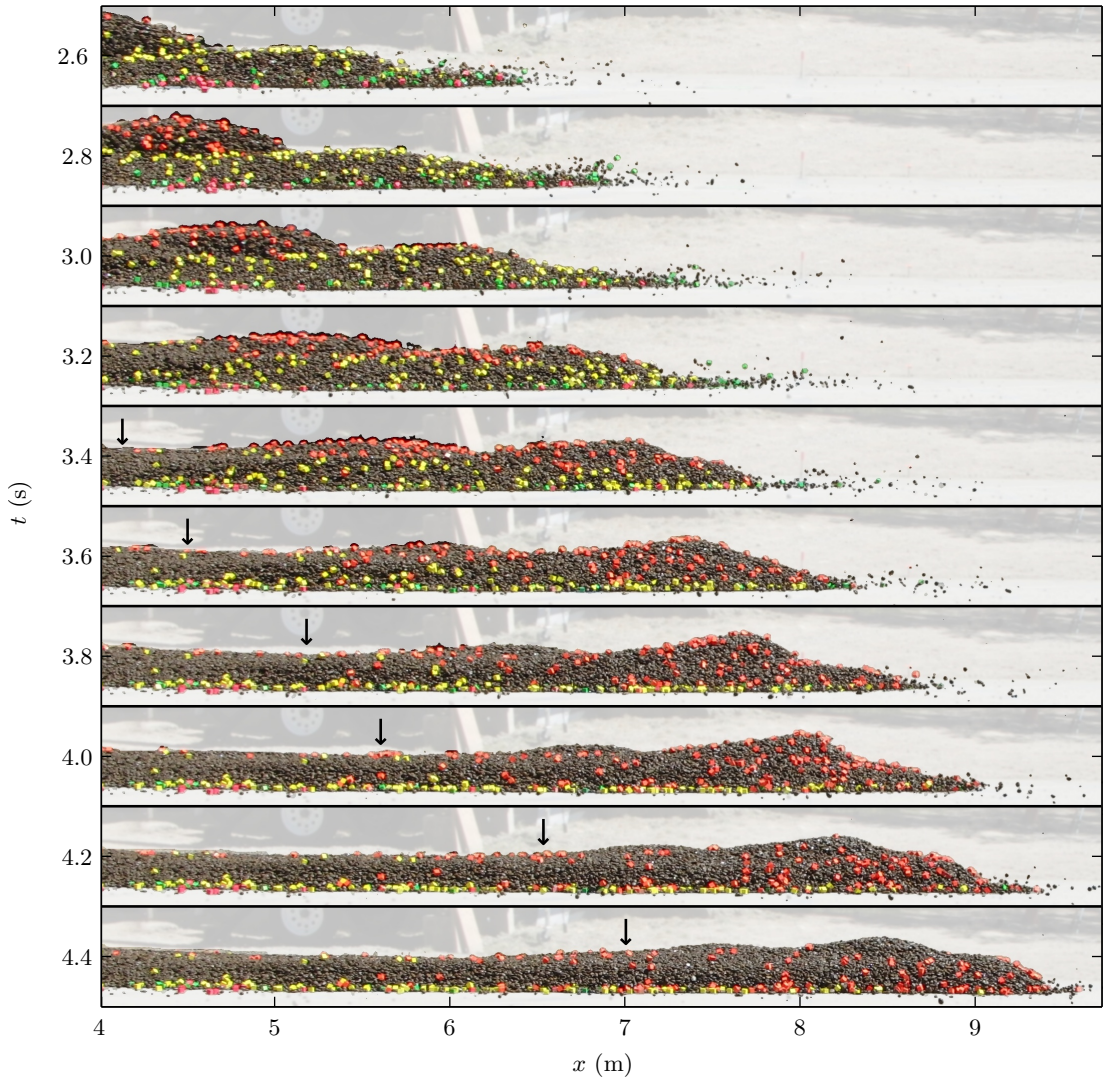

Figure 5. Time-sequence of side-view photographs of the August 25th debris-flow runout. The arrow indicates the maximum downstream extent of the deposited stationary levee. The vertical scale of each photograph covers ∼60 cm.

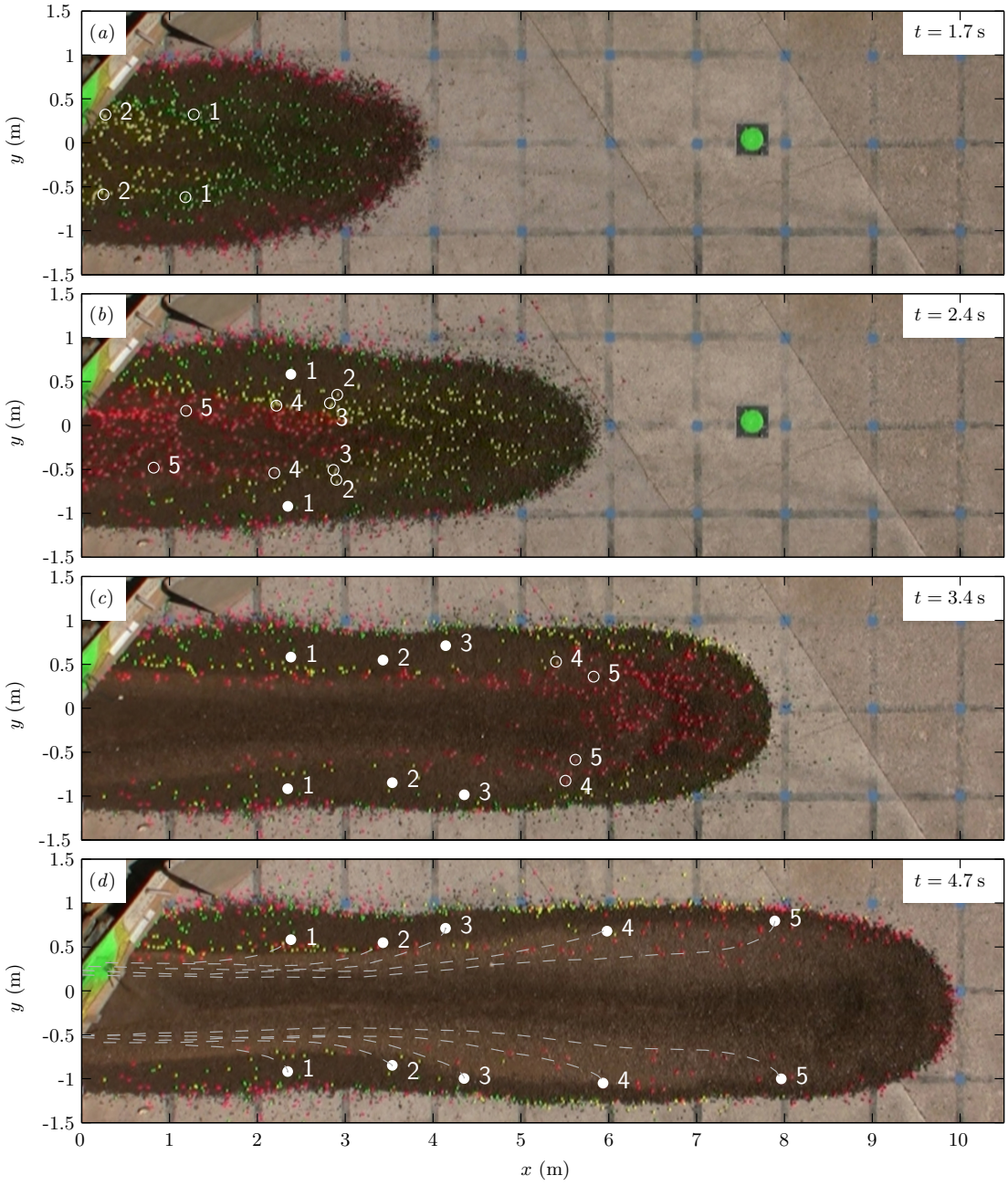

Figure 6. Overhead views of surface trajectories of particles in the August 25th experiment. Between each frame (*a*–*d*), the flow advances by 2 m. Moving particles are marked with open circles, and deposited particles with filled circles. In (*a*), particles marked 1 are farthest downstream in the flow, followed by particles 2–5 in sequence (3–5 out of frame). As the flow progresses, those particles closest to the flow front are advected outwards and deposited (*b*–*c*). The sequence of particles when deposited (*d*), is reversed from that in the flow, with particles marked 5 farthest downstream. An animated version of this figure is shown in movie 3.

Figure 7. Oblique ground-level photograph of the August 25th experimental deposit, looking upslope from the deposit termination. Tracer cubes deposited on the surface lie on or near the levee walls at the flow margins, rather than in the central channel. The tracer cubes are deposited in coloured bands, from orange cubes near the deposit termination (foreground), then yellow, then green, then pink cubes near the flume mouth. This pattern represents a reversal of the order in which the cubes were seeded onto the flow surface; the last cubes to be seeded onto the flow (orange), were deposited furthest from the flume mouth.

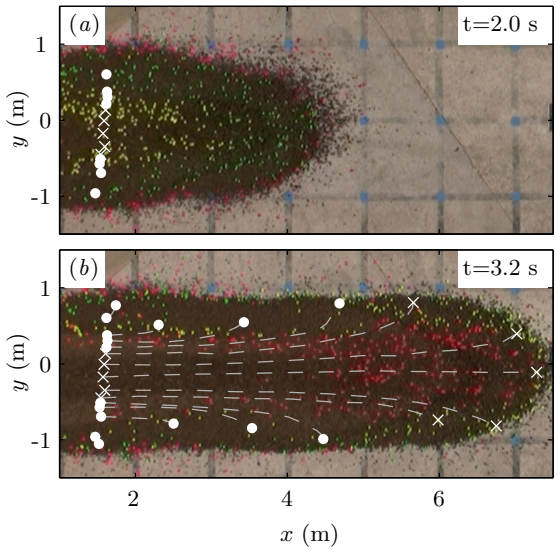

Figure 8. Surface and burial trajectories of particles in the August 25th experiment. Particles close to the flow axis, marked with crosses (a), are advected over the flow front and become buried (b). Particles farther away from the flow axis, marked with dots, remain on the surface and are deposited on the surface of the levees.

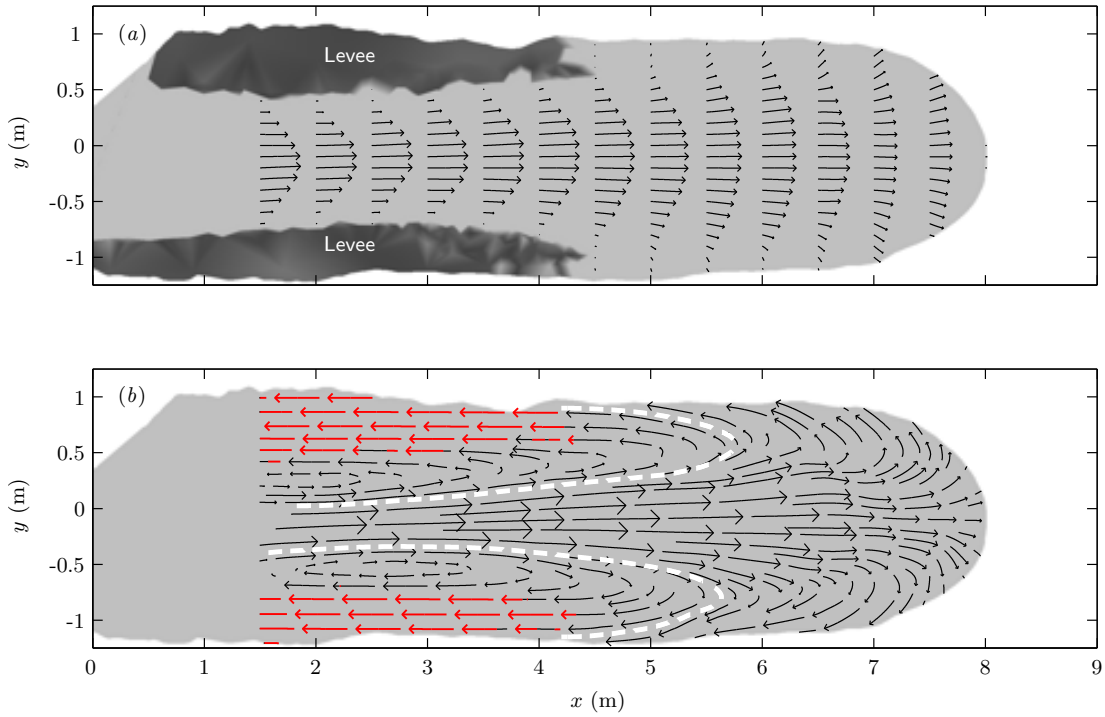

Figure 9. Surface velocities in the experiment of August 25th, 3.5 s after the flow reached the flume mouth (corresponding to the snapshot shown in figure 4*a*). In (*a*) the surface velocity field is shown in a stationary frame. In (*b*) the same velocity field is shown, but in a frame moving at the speed of the head, at 2.0 m s^{-1}. In this frame the velocity field is steady. Material that is effectively stationary, taken to be that moving at less than 4 cm s^{-1}, is indicated with darker shading in (*a*) and with red arrows in (*b*). The white dashed line in (*b*) demarcates particles near the centre of the flow which reach the flow boundary and are buried from those which remain on the surface and are advected onto the surface of the levees.

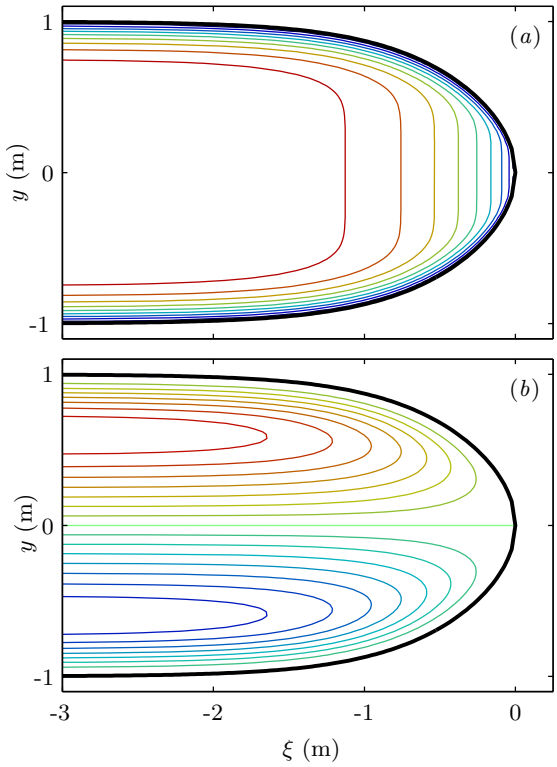

Figure 10. Functions chosen to model the debris flow head. In (a), contours of h are shown at intervals of 2.5 cm. In (b) contours of ψ are shown, which are streamlines of the depth-integrated velocity field $(\bar{u}, \bar{v})$. The thick black line indicates the deposit outline at $y = \pm y_0(\xi)$.

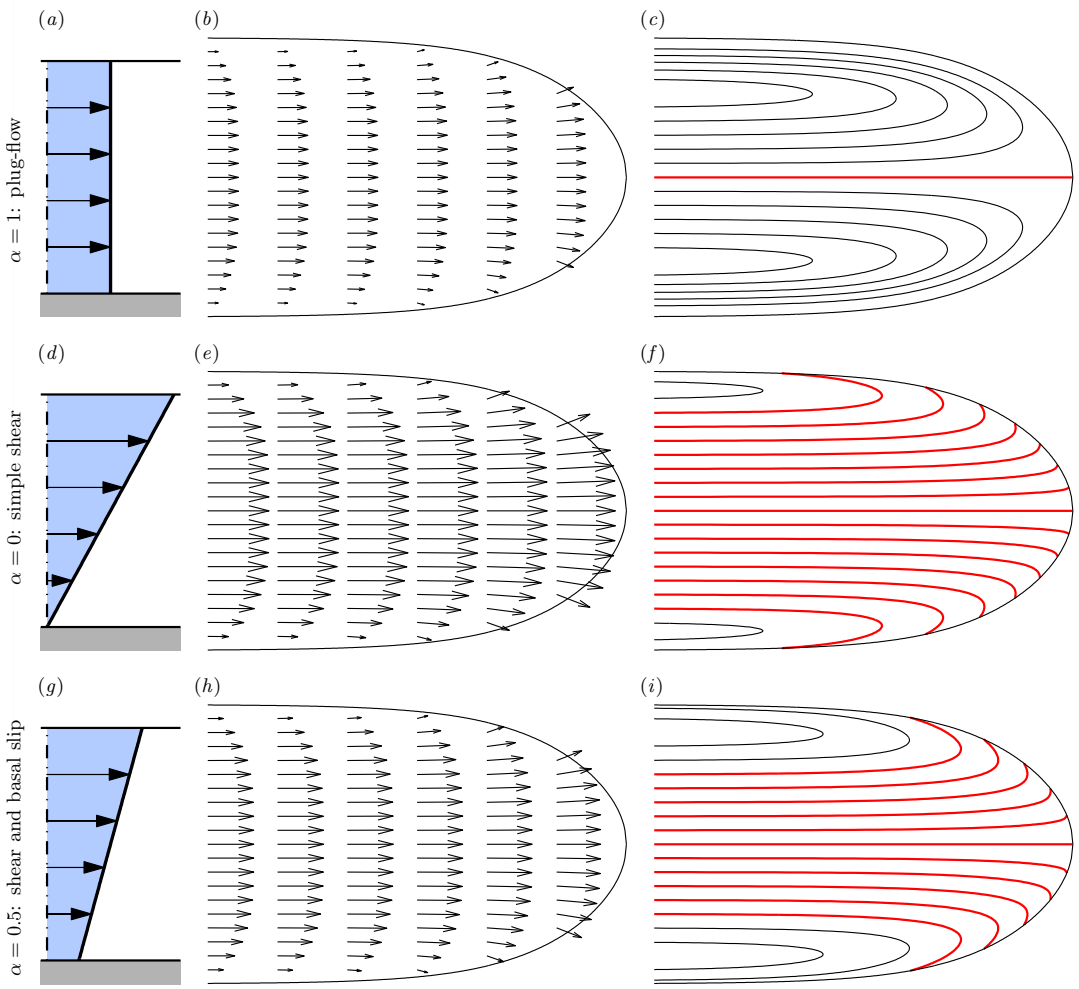

Figure 11. Velocity profiles and resulting surface velocity fields in the debris-flow head, with the flow velocity field given by (11) and (14). The vertical velocity profiles (a,d,g), surface velocity fields in the stationary frame (b,e,h) and streamlines in a frame moving with the flow front (c,f,i) are each shown for three different velocity profiles. The top row (a,b,c) shows plug-flow ($\alpha = 1$), the middle row (d,e,f) simple shear ($\alpha = 0$), and the bottom row (g,h,i) shows a combination of shear and basal slip that is inferred from the debris-flow experiments, where $\alpha = 0.5$. The surface velocities in the stationary frame are identical for all vertical velocity profiles, up to a scaling factor. The surface streamlines in the moving frame that reach the front of the flow are shaded red; the proportion of material on the flow surface that reaches the flow front and is overpassed is strongly dependent on the extent of internal shear.

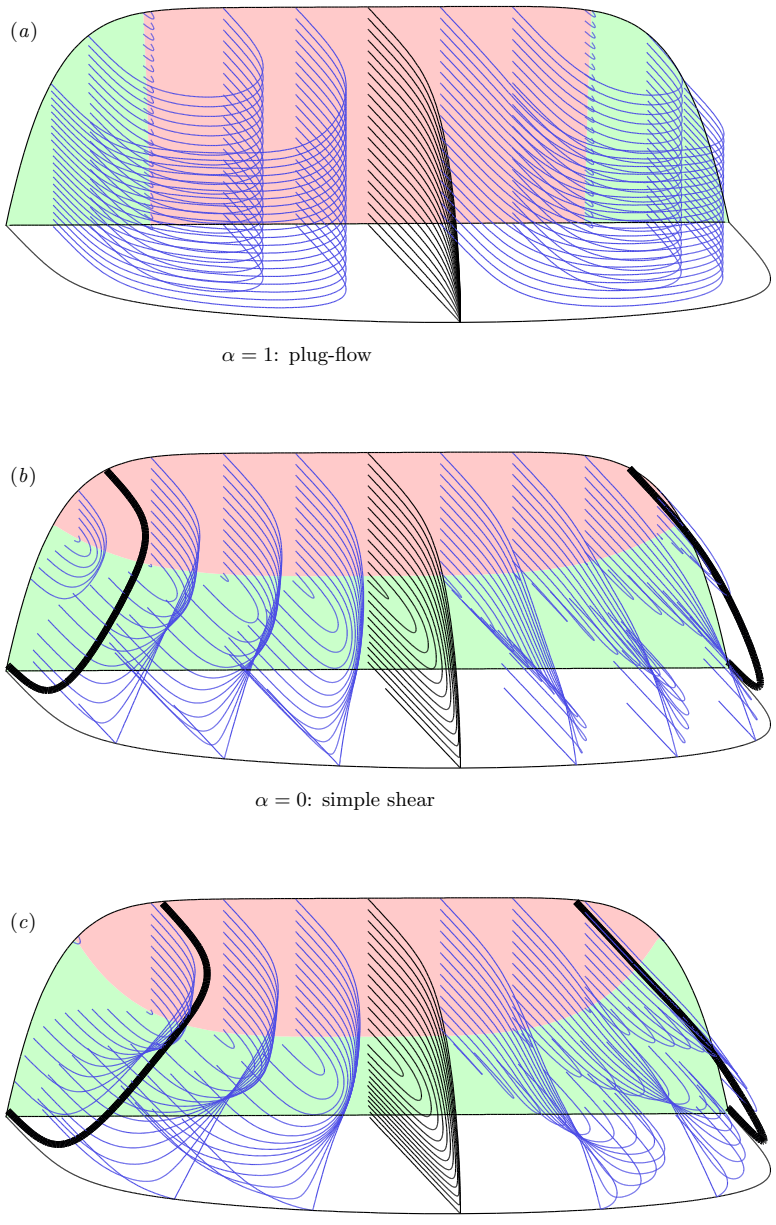

Figure 12. Three-dimensional particle paths within the flow head, with the flow velocity field given by (11) and (14). Pink shading indicates the regions at the back of the head where material is moving downstream more quickly than (and therefore towards) the flow front. Green shading indicates material is moving downstream more slowly than (and therefore away from) the flow front. In plug-flow (a), all streamlines coincide with the depth-integrated streamlines, and material in the head is transported laterally from the central channel to the flow margins. In the case of simple-shear (b), material from the top half of the flow, which is moving faster than the rate of propagation of the flow head, is transferred to the base of the flow as it passes over the flow front, with very little transverse motion. At the intermediate velocity profile of $\alpha = 0.5$ present in the flume flow (c), material travelling through the flow head is both transported laterally within the flow head, and to the base of the flow as it passes over the flow front.

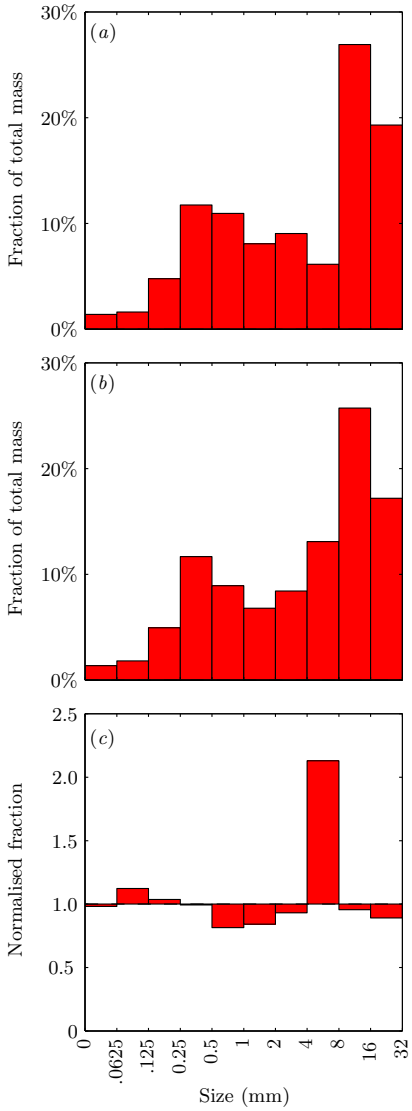

Figure 13. (*a*) Mean grain-size distribution of initial charge used in the August 25th experiment. (*b*) Mean grain-size distribution of initial charge used in the August 27th experiment. (*c*) Relative abundance plot showing the grain-size distribution of the August 27th initial charge normalised against that of the August 25th experiment. The axes for this histogram are the same as those used in the miniature plots in Figures 14 and 15, where histogram bars indicate enrichment (values > 1) and depletion (values < 1) of material in each grain-size class relative to the particle-size distribution of the relevant initial charge.

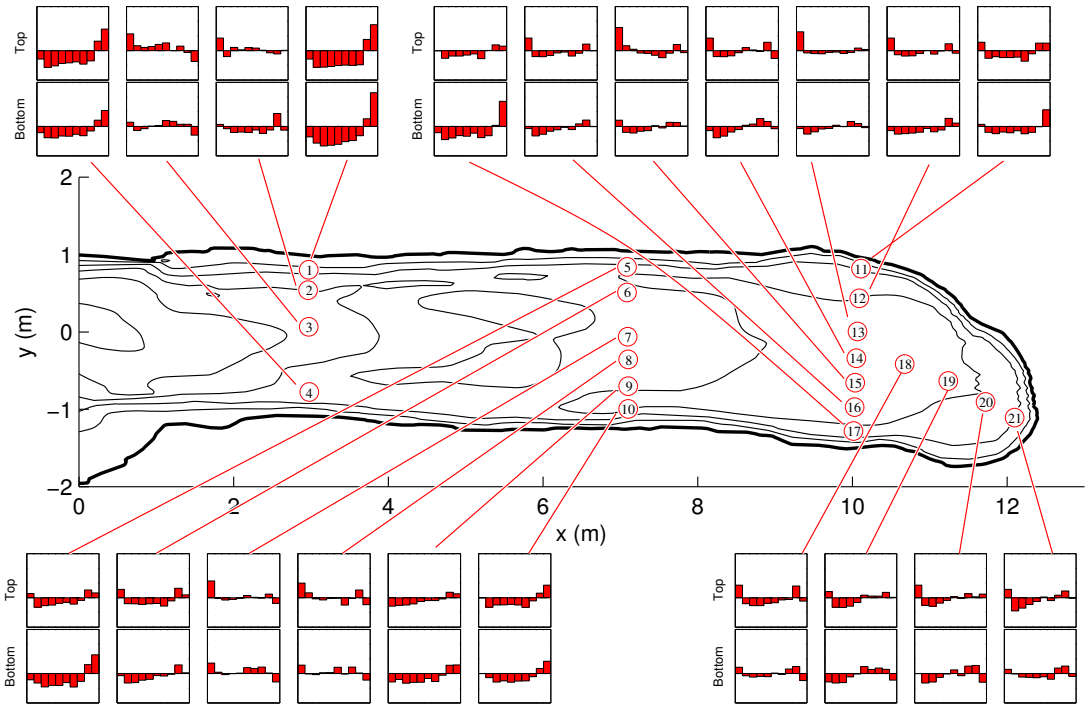

Figure 14. Relative abundance plots of deposit granulometry in the 25th August experiment. Axes for the plots are as for figure 13(c): coarse material is to the right and fine material to the left. Contours show deposit thickness, with 5 cm spacing; the thicker line indicates the deposit margin.

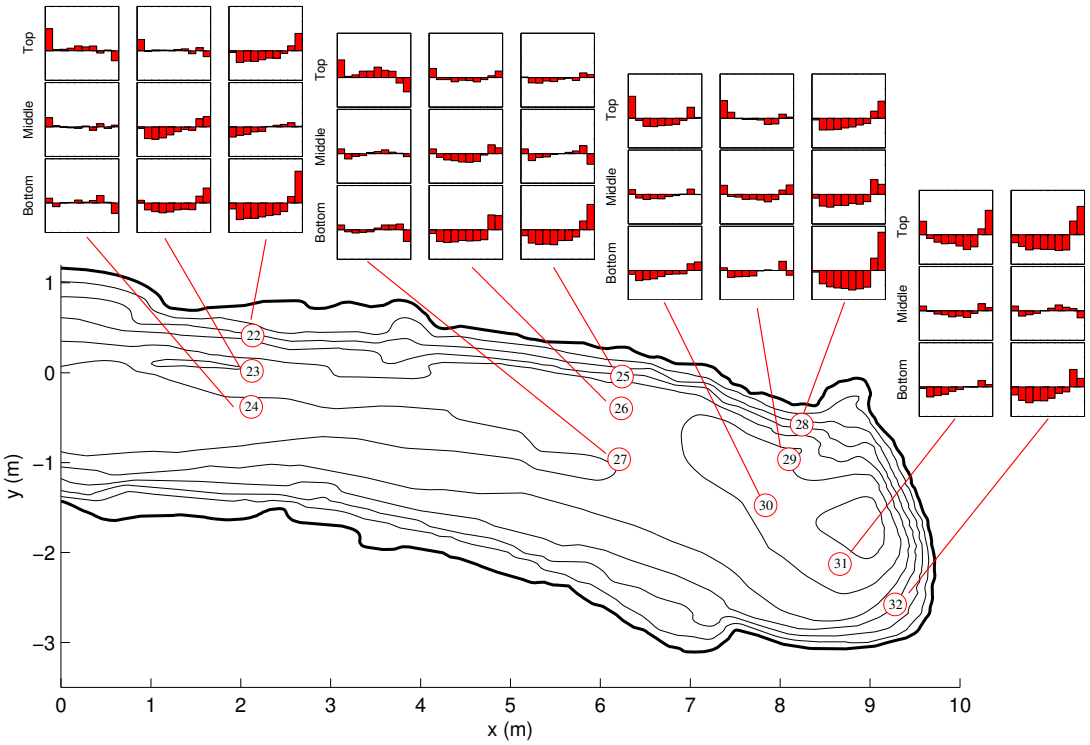

Figure 15. Relative abundance plots of deposit granulometry in the 27th August experiment. Axes for the plots are as for figure 13(c): coarse material is to the right and fine material to the left. Contours show deposit thickness, with 5 cm spacing; the thicker line indicates the deposit margin.

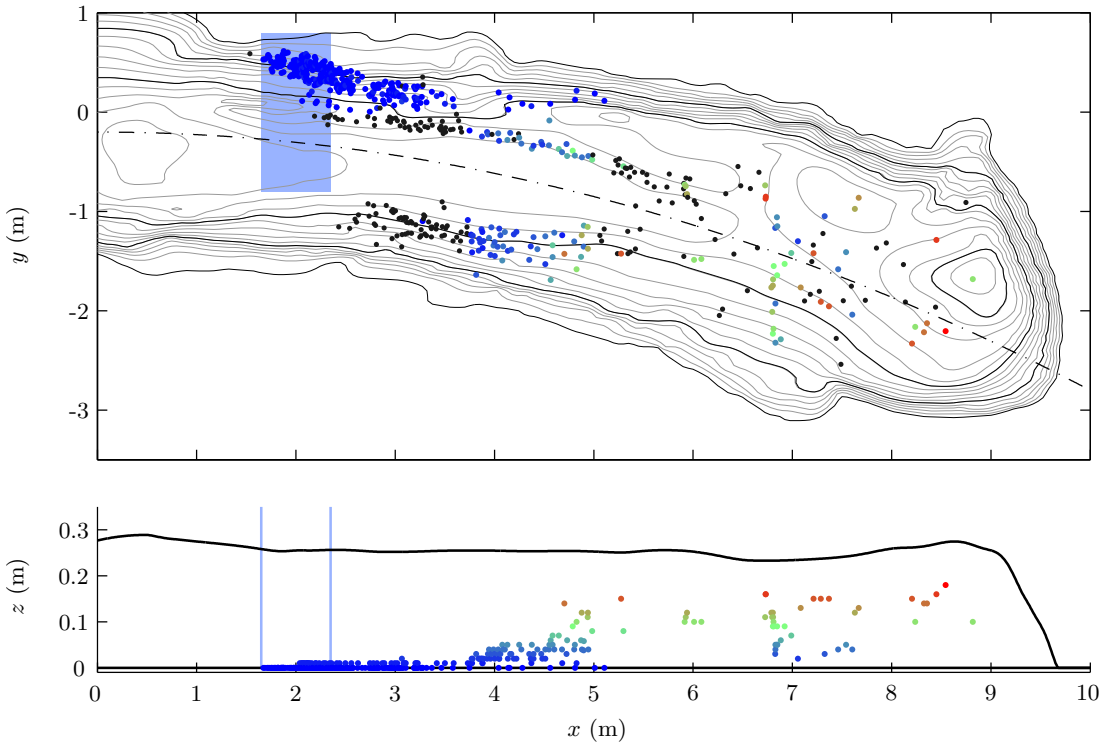

Figure 16. Positions of tracer pebbles in the August 27th deposit. Pebbles were initially distributed uniformly in a rectangular area (shaded blue) 2 m downstream of the flume exit. Pebbles are coloured according to their height in the deposit; no heights were recorded for stones plotted in black. In the overhead view (top), contours of deposit thickness are every 2 cm, with heavy-line contours every 10 cm. The flow centreline is indicated by the dot-dashed line. In the side view (bottom), the depth of the deposit along the centreline is indicated by the solid line. Note the 4.6× vertical exaggeration.

Figure 17. Photograph of the 27th August deposit termination. Approximately 5 cm of surface material has been removed from a sector of the deposit, uncovering two white tracer stones. The surface material removed, like that visible behind the excavated sector, is strongly coarse-enriched. White lines on the undisturbed deposit surface are topographic contours, determined by laser leveling and applied with paste.

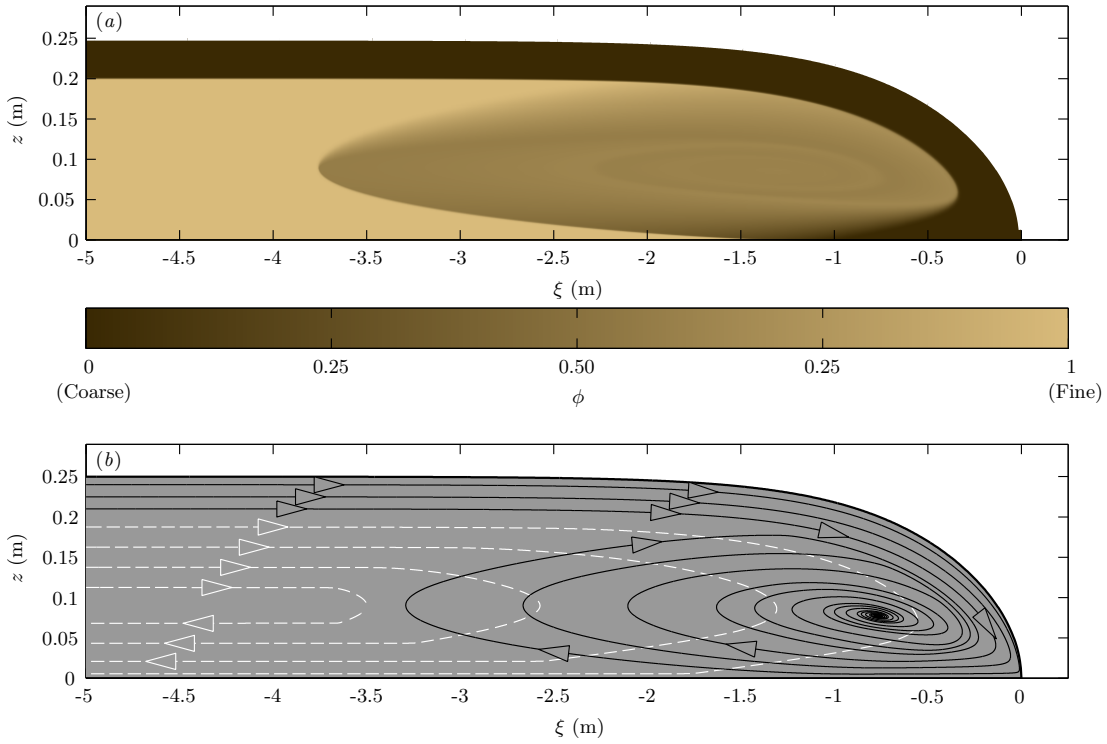

Figure 18. Solution of the segregation equation (16) in a velocity field resembling the central plane of the debris-flow runout. (a) shows small-particle concentration ϕ; (b) shows paths of coarse particles (black lines) and fine particles (dashed white lines).

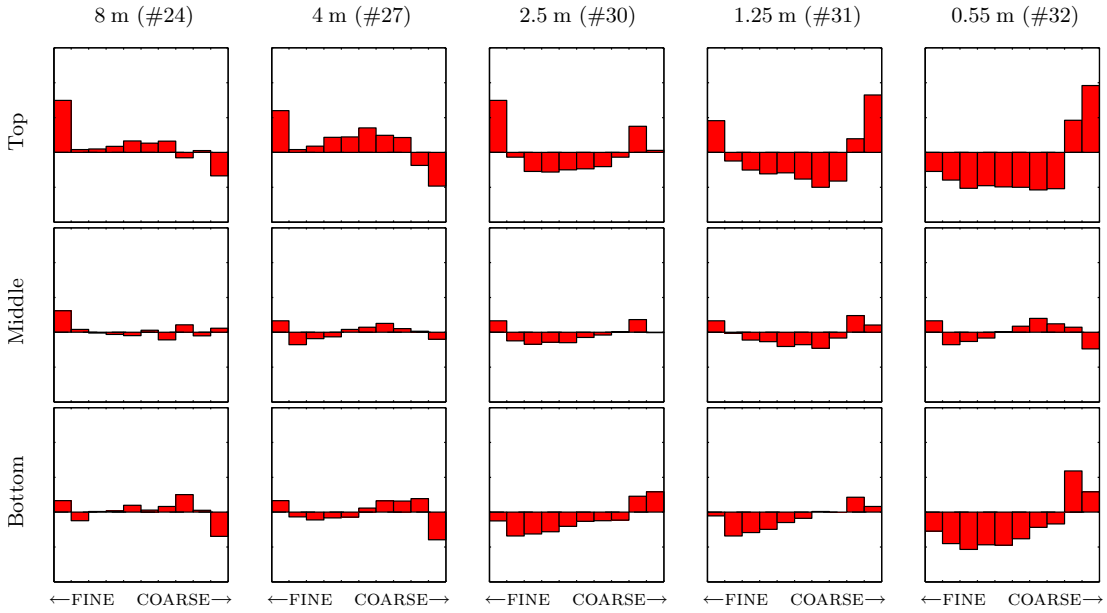

Figure 19. Relative abundance plots of deposit granulometry in the central channel of the 27th August experiment. Samples are labeled by their site number and by their distance upstream of the deposit termination at $x = 9.7$ m. Axes for the plots are as for figure 13(c).

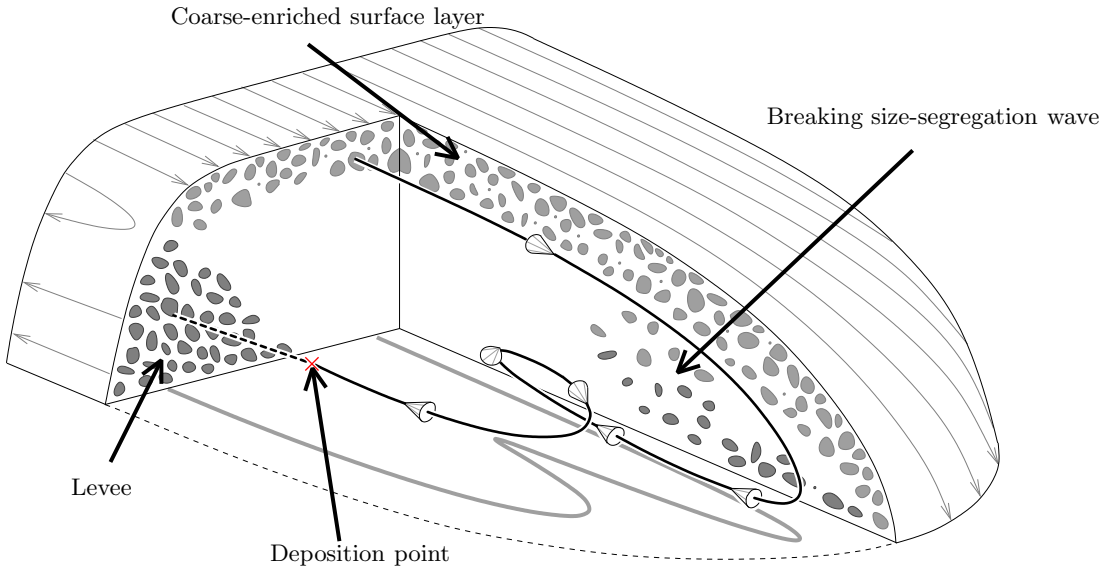

Figure 20. A cutaway sketch showing a moving-frame view of the coarse-enriched regions and the three-dimensional path of a segregating coarse particle through the debris-flow head. Coarse particles with light shading are those moving downstream faster than (and therefore towards) the flow front. Coarse particles with darker shading are stationary or moving slower than the flow front; these include those in the levees and at near the base of the flow. The path of a typical coarse particle in the surface layer near the centre of the flow is shown. The particle is transported into the flow head and is overpassed when it reaches the flow boundary. Now at the base of the flow, it moves more slowly than the advancing flow front, and begins to segregate upwards as part of a breaking size-segregation wave. The particle may recirculate a number of times within the flow head, but is continually advected away from the flow centreline, towards the sides of the flow. The particle deposits when it becomes part of the progressively accreting levees.

3. Granular jets and hydraulic jumps on an inclined plane

Publication 2: *Granular jets and hydraulic jumps on an inclined plane*

Granular jets and hydraulic jumps on an inclined plane

C. G. JOHNSON and J. M. N. T. GRAY

School of Mathematics and Manchester Centre for Nonlinear Dynamics, University of Manchester, Oxford Road, Manchester, M13 9PL, UK

(Received 7 October 2009 and in revised form 20 December 2010)

A jet of granular material impinging on an inclined plane produces a diverse range of flows, from steady hydraulic jumps to periodic avalanches, self-channelised flows and pile collapse behaviour. We describe the various flow regimes and study in detail a steady-state flow, in which the jet generates a closed teardrop-shaped hydraulic jump on the plane, enclosing a region of fast-moving radial flow. On shallower slopes, a second steady regime exists in which the shock is not teardrop-shaped, but exhibits a more complex 'blunted' shape with a steadily breaking wave. We explain these regimes by consideration of the supercritical or subcritical nature of the flow surrounding the shock. A model is developed in which the impact of the jet on the inclined plane is treated as an inviscid flow, which is then coupled to a depth-integrated model for the resulting thin granular avalanche on the inclined plane. Numerical simulations produce a flow regime diagram strikingly similar to that obtained in experiments, with the model correctly reproducing the regimes and their dependence on the jet velocity and slope angle. The size and shape of the steady experimental shocks and the location of sub- and super-critical flow regions are also both accurately predicted. We find that the physics underlying the rapid flow inside the shock is dominated by depth-averaged mass and momentum transport, with granular friction, pressure gradients and three-dimensional aspects of the flow having

comparatively little effect. Further downstream the flow is governed by a friction-gravity balance, and some flow features, such as a persistent indentation in the free surface, are not reproduced in the numerical solutions. On planes inclined at a shallow angle, the effect of stationary granular material becomes important in the flow evolution, and oscillatory and more general time-dependent flows are observed. The hysteretic transition between static and dynamic friction leads to two phenomena observed in the flows: unsteady avalanching behaviour, and the feedback from static grains on the flowing region, leading to leveed, self-channelised flows.

---

1. Introduction

It is a familiar observation that a jet of fluid impinging normally on a horizontal plane generates a thin, circular region of rapid radial flow surrounded by a stationary hydraulic jump, beyond which lies a thicker, slower moving fluid layer. The first analysis of this situation, in the case of inviscid fluid, is due to Lord Rayleigh (1914). The problem has since been extensively studied, and has been generalised to cover various fluid-dynamical phenomena such as viscosity (Watson 1964), internal interfaces (Thorpe & Kavcic 2008), non-Newtonian rheology (Zhao & Khayat 2008) and surface tension (Bush & Aristoff 2003). We examine in this paper the related situation of a vertical jet of granular material impinging on an inclined plane, shown schematically in figure 1. There are three key differences from Rayleigh's analysis: the flow of grains rather than of fluid, the impingement of the jet at an oblique angle, and the effect of gravity on the flow down the inclined plane.

Several related problems of jet impingement and subsequent flow have previously been considered. The oblique impact of a fluid jet on a horizontal surface is described by

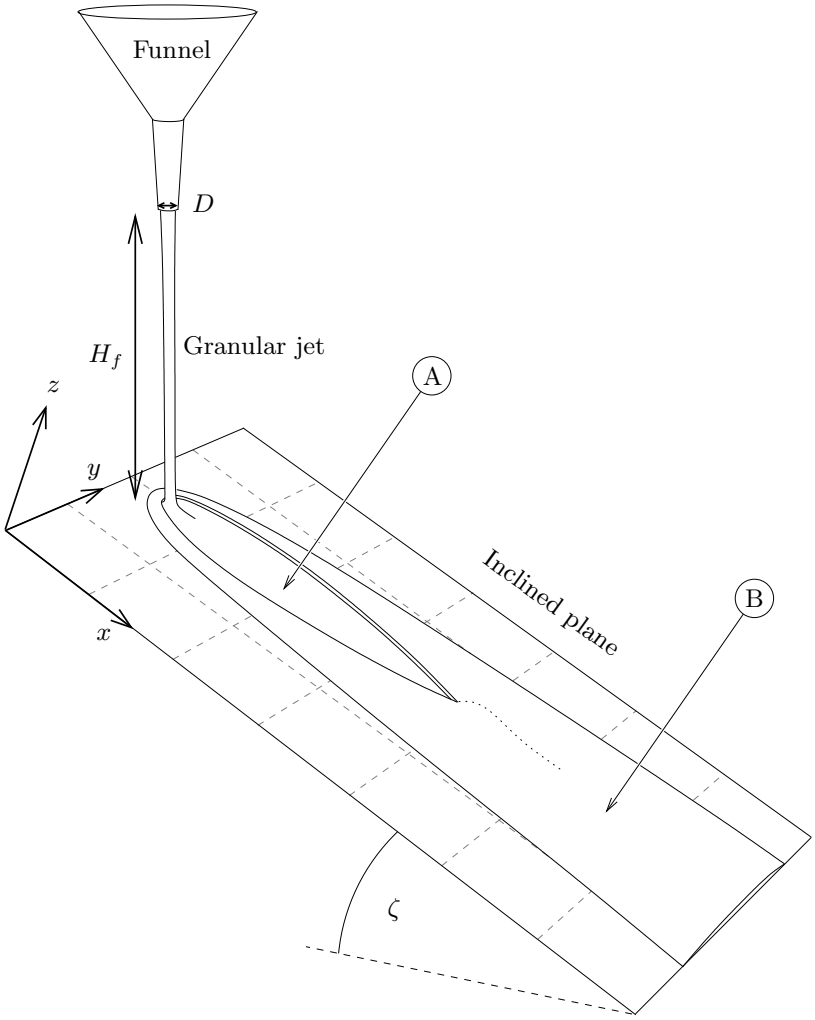

FIGURE 1. Diagram of the experimental apparatus. The granular jet impinges on the inclined plane, spreading into a region of thin, fast flow (A). The granular material then passes through a jump, becoming thicker and slower (B), and flows down the plane, which is inclined at an angle ζ to the horizontal.

Kate, Das & Chakraborty (2007), who observe the circular hydraulic jump of Rayleigh in flows generated by a vertical fluid jet, and an elliptical hydraulic jump for jets with impingement angles within 65° from normal. For angles greater than this, when the jet impinges near-tangentially, closed hydraulic jumps with sharp corners are observed. These are attributed to two phenomena: the interaction of the jet with the hydraulic jump and, by analogy with compression shocks of gas dynamics, the presence of Mach stems. Edwards *et al.* (2008) consider theoretically the normal impingement of a fluid jet on a plane inclined at an angle. In this situation, the predicted hydraulic jump is

not closed, but instead forms an open curve resembling a parabola. The flow is similar to the sheet of flow generated by two symmetric impinging jets (Taylor 1960; Bush & Hasha 2004), in that the more slowly-moving fluid outside of the shock forms a tube-like structure, which is small in width compared to the size of the enclosed thin film. This separation of scales is exploited to model the outer region as a 'mass tube', a line initially of unknown position, which carries mass and momentum fluxes. Coupling this to analytic solutions of a shallow-water model for the inner fast-moving region allows the location of the shock to be calculated. In the granular case, the problem of a jet of sand impinging normally on a horizontal plane is examined experimentally by Boudet *et al.* (2007). The behaviour found is similar to that in the fluid case, in that the granular jet transitions to a thin, fast, radial flow on impact with the plane, which is bounded by a annular jump in the layer thickness. In contrast to the fluid behaviour, the basal friction between the granular material and the horizontal plane slows the radial flow, and leads to the material outside the jump becoming stationary. The jump then propagates inwards, towards the point of jet impact.

Interest in the granular problem, and in granular flows in general, stems from the widespread use of granular materials, and the considerable problems encountered in understanding their behaviour. The flow of granular materials is central to the modelling of debris-flows (Iverson 1997) and snow avalanches (Gruber & Bartelt 2007; Cui, Gray & Jóhannesson 2007) in geophysics, to problems of transport, mixing and crushing of grains and powders in industry, and to problems of soil stability and mechanics (Mitchell & Soga 2005) in civil engineering. Granular materials exhibit a wide range of behaviour, including solid-like, liquid-like and gas-like states, depending on factors such as grain density, granular temperature and shear stress (Rajchenbach 2000; Liu & Nagel 1998).

2. Governing equations of shallow granular flows

Granular flows of small aspect ratio (those in which the flow depth is much less than its horizontal extent) are common in free-surface flows on an inclined surface, whether at laboratory or geophysical scales. Such flows have been successfully modelled using shallow-layer models (Grigoryan *et al.* 1967; Eglit 1983; Savage & Hutter 1989; Gray, Wieland & Hutter 1999). A major difference between these depth-averaged models and fluid hydraulic or shallow-water systems is in the form of friction present at the base of the granular flow, either a Coulomb friction for smooth slopes (Savage & Hutter 1989) or a more complex friction model (that of Pouliquen & Forterre 2002, for example) for dry granular flows on rough slopes. Such friction laws, in contrast to viscous or turbulent friction modelling in shallow fluid layers, have the ability to hold a pile of material stationary on an inclined surface.

In common with the fluid-dynamical case, the hyperbolic equations of shallow-layer granular flow predict the formation of shocks, which correspond to *granular jumps*, the granular analogue of hydraulic jumps. These have been observed and studied in dense granular avalanches in chutes (Savage 1979; Brennen, Sieck & Paslaski 1983) and in flowing surface layers (Gray & Hutter 1997). More recently, two-dimensional oblique shocks have been observed in granular avalanches (Gray, Tai & Noelle 2003), which are quantitatively predicted by a similar analysis to that of hydraulic theory (Rouse 1949; Hákonardóttir & Hogg 2005; Gray & Cui 2007; Vreman *et al.* 2007). Density, or compression shocks have also been observed in granular materials, both in the regime of a granular gas (Rericha *et al.* 2002), where they are analogous to the shocks observed in compressible gas dynamics, and in dense avalanche flows (Eglit, Kulibaba & Naaim 2007).

In a shallow-avalanche model, the flow is assumed to be incompressible, and is repre-

sented in terms of its depth-averaged velocity $\mathbf{u}$, and height h. The governing equations are those of conservation of mass and momentum. Our coordinate system is defined such that the x-axis is oriented in the down-slope direction, the y-axis in the cross-slope direction and the z-axis is the upward pointing normal to the plane, completing a right-handed Cartesian coordinate system (figure 1) with the origin at the point of jet impingement. The components of the velocity $\mathbf{u}$ in the x and y directions are denoted u and v respectively.

We present the equations in the non-dimensional form of Savage & Hutter (1989). Dimensional variables, denoted by a tilde, are related to their non-dimensional counterparts by the equations

$$\tilde{h} = Hh, \;\; (\tilde{x}, \tilde{y}) = L(x, y), \;\; (\tilde{u}, \tilde{v}) = \sqrt{Lg}\,(u, v), \;\; \tilde{t} = \sqrt{L/g}\,t\,, \tag{2.1}$$

where H and L are typical length-scales of the flow thickness and horizontal extent respectively. Defining the small aspect ratio $\epsilon = H/L$, the non-dimensional equations for conservation of mass, and momentum in the x and y directions are then (Gray *et al.* 2003)

$$\frac{\partial h}{\partial t} + \frac{\partial}{\partial x}(hu) + \frac{\partial}{\partial y}(hv) = 0\,, \tag{2.2}$$

$$\frac{\partial}{\partial t}(hu) + \frac{\partial}{\partial x}(hu^2) + \frac{\partial}{\partial y}(huv) + \frac{\partial}{\partial x}\left(\frac{1}{2}\epsilon h^2 \cos\zeta\right) = hs_x\,, \tag{2.3}$$

$$\frac{\partial}{\partial t}(hv) + \frac{\partial}{\partial x}(huv) + \frac{\partial}{\partial y}(hv^2) + \frac{\partial}{\partial y}\left(\frac{1}{2}\epsilon h^2 \cos\zeta\right) = hs_y\,. \tag{2.4}$$

The source terms

$$s_x = -\mu\frac{u}{|\mathbf{u}|}\cos\zeta + \sin\zeta\,, \tag{2.5}$$

$$s_y = -\mu\frac{v}{|\mathbf{u}|}\cos\zeta\,, \tag{2.6}$$

encompass both the effects of friction between the material and the inclined plane (through the basal friction coefficient μ), and the component of gravity in the x-direction.

Note that if we define $\hat{h} = \epsilon h$ then (2.2)–(2.6) can be rewritten in terms of the variables $(\hat{h}, \mathbf{u})$ in a form that is completely independent of ϵ. The parameter ϵ may therefore be chosen arbitrarily. Here however we use the scalings (2.1) and retain ϵ in the equations to emphasise that the dominant balance in the avalanche equations is between the acceleration and source terms.

A Froude number

$$Fr = \frac{|\mathbf{u}|}{\sqrt{h\epsilon\cos\zeta}} \tag{2.7}$$

is defined as the ratio of flow speed to the speed of inertia-gravity waves. In steady flows, the Froude number relates directly to the way information is propagated by these waves. Information, in the form of small disturbances, is able to propagate in all directions in subcritical regions, where $Fr < 1$. In supercritical regions, where $Fr > 1$, information is unable to propagate against the direction of the flow (Courant & Hilbert 1962; Weiyan 1992). In supercritical flows the hyperbolic structure of the equations allows for discontinuities in the solution, or shocks, at which the assumption of smoothness implicit in the formulation of (2.2–2.4) is invalid. A relationship between the solution values on either side of the shock is instead given by the jump conditions

$$[\![h(\mathbf{u}\cdot\mathbf{n} - v_n)]\!] = 0\,, \tag{2.8}$$

$$[\![h\mathbf{u}(\mathbf{u}\cdot\mathbf{n} - v_n) + \tfrac{1}{2}\epsilon h^2\cos\zeta\mathbf{n}]\!] = 0\,, \tag{2.9}$$

derived from the mass and momentum conservation equations in integral form. The jump bracket $[\![\cdot]\!]$ denotes the change in continuum variables over a shock, $\mathbf{n}$ is a vector normal to the shock and v_n is the shock speed.

3. Experimental observations

Our experimental setup is shown in figure 1. A funnel with a circular mouth of diameter D, in the range 8–15 mm, is held at a distance H_f above an inclined plane. Granular material flowing from the funnel impinges on the inclined plane and generates a thin free-surface flow, or avalanche, on the plane. The surface of the plane is made of untreated hardboard, which is rough at scales below approximately 100 μm. The funnel is fed from another hopper with larger flow rate to prevent variations in the supplied mass flux caused by a varying level of material in the lower funnel. The variation in mass flux delivered by the funnels, measured across 0.6 s samples, is less than 1.6%. We observe no long-term variability in the flow (caused, for example, by changing environmental conditions) in this setup.

The granular material used in the experiments presented in this paper is soft masonry sand, sieved to a diameter $d \leqslant 600$ μm. The experiments were also performed with glass 'deco' beads of two sizes, $75 \leqslant d \leqslant 150$ μm and $500 \leqslant d \leqslant 750$ μm, and with nonpareil sugar grains with $d \approx 1000$ μm. The flow on the plane is qualitatively independent of the type of granular material, exhibiting the same regimes of flow for all the materials tried. The flow in the region where the jet impacts the plane, however, is sensitive to particle properties. A small proportion of the granular material falling from the funnel does not transition to flow over the inclined plane at the point of impingement, but instead bounces off the plane, forming a sparse cloud of fast-moving grains. This proportion increases with funnel height (a behaviour attributable to the decreasing density of the jet as it falls) and becomes the dominant behaviour of the flow for sufficiently large H_f. For glass beads and sugar grains, a substantial proportion of the jet becomes airborne when $H_f \gtrsim 15$ cm (for $D = 15$ mm), a sufficiently low height that flows can be observed only in a very restricted parameter space. The corresponding maximum H_f for sand is much higher,

approximately 50 cm. Results are therefore presented only for sand in this paper. The maximum funnel height is also limited by a clustering instability in falling granular jets, resembling that of the Rayleigh-Plateau instability for fluids (Royer *et al.* 2009). The instability has its onset at a distance greater than 50 cm from the funnel for $D \geqslant 8$ mm, and is therefore not a significant source of mass flux variation in the current experiment. For the range of funnel widths used, the requirement that the flow transitions smoothly to a flow over the inclined plane restricts the maximum H_f to a lower level than that enforced by the onset of the jet instability.

We consider primarily the flow after its impact with the plane. Depending on the slope angle, funnel height and funnel width, this flow exhibits a wide range of behaviours, resulting from the interaction between the momentum imparted to the flow by the falling granular material, friction between the plane and the granular material, and gravity.

3.1. *Steady teardrop-shaped granular jumps*

In the first flow regime, the falling jet generates a region of thin, fast-moving flow, which meets slower-moving material surrounding it at a granular jump. Boudet *et al.* (2007) demonstrated that on a horizontal plane, material behind this shock is stationary and the shock propagates inwards toward the point of impingement. However, for planes inclined at a sufficiently steep angle, the material flows on both sides of the granular jump, leading to a stationary granular jump surrounded by a steady flow.

Such a steady-state flow, for $\zeta = 26.7°$, $H_f = 30$ cm is shown in figure 2. In the region of fast, thin supercritical flow within the shock, the flow velocity is predominantly radial, away from the point of impingement. Across the closed granular jump surrounding this region, the flow height rapidly increases and flow velocity normal to the shock rapidly decreases. In the region surrounding and downstream of the shock, grains flow more slowly, and largely in the downslope direction. In the flow shown in figure 2 the hydraulic

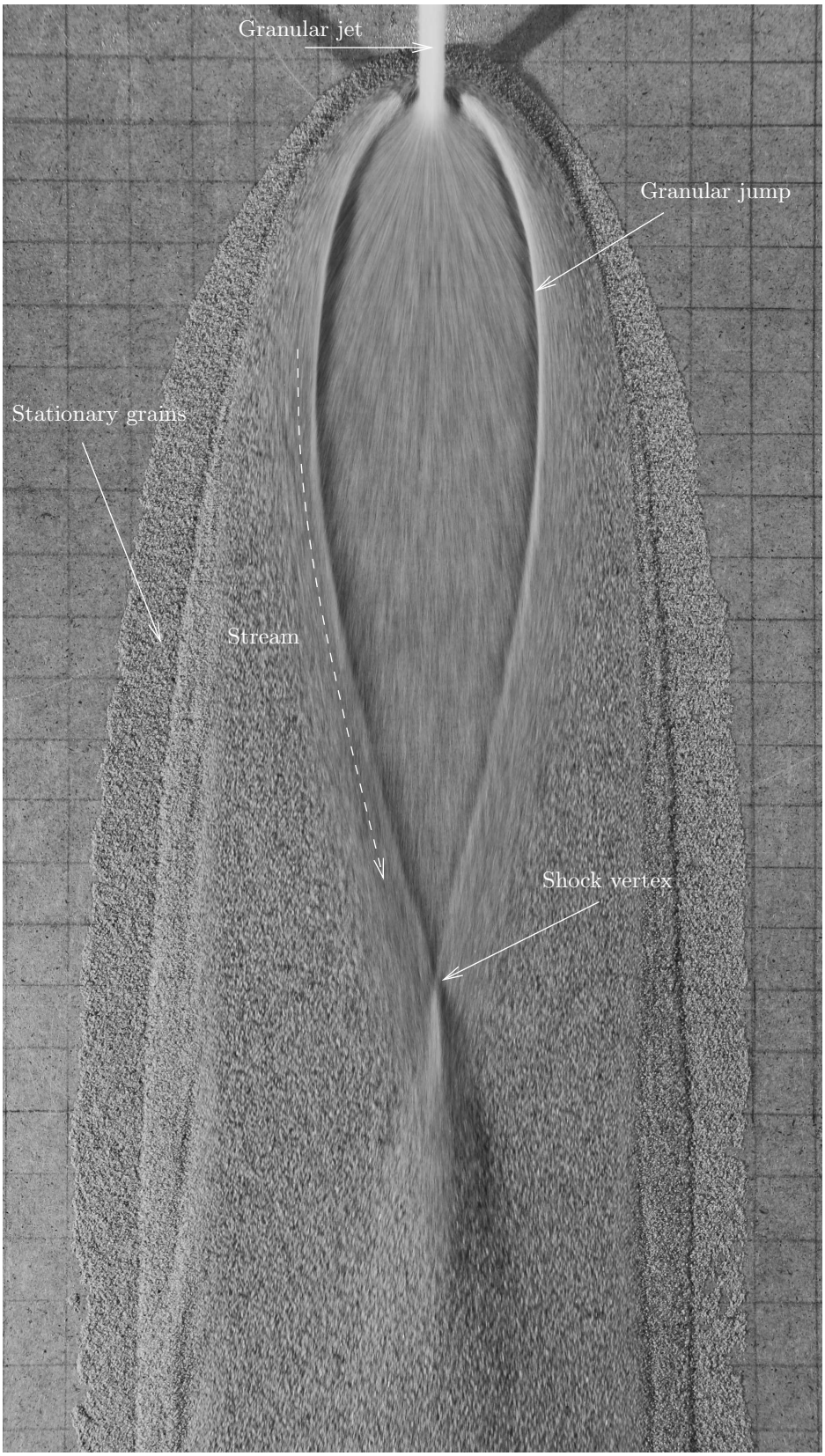

FIGURE 2. A teardrop-shaped shock in sand for $\zeta = 26.7^\circ$, $H_f = 30$ cm, $D = 15$mm. Grid squares are at 2 cm intervals, in this and subsequent figures. The shutter speed is 1/80 s.

jump is teardrop-shaped, with the shock displaying a single vertex directly downslope of the point of impingement.

The motion blur in still photographs of the experiment taken over a range of shutter speeds allows an estimation of surface flow velocities to be made, with an accuracy of about $\pm 10\%$. The thin radial flow surrounding the point of impingement has a speed of approximately 0.99 ms^{-1}. Substantial velocity variations exist in the thicker flow surrounding the jump, with the fastest velocities, approximately 0.4 ms^{-1} being observed close to the jump, where the flow is almost parallel to the line of the shock. This forms two fast-moving streams of material in the thicker flow, which meet at the vertex of the teardrop-shaped shock. At this oblique collision of the two streams, material is forced upwards into a narrow 'spout' normal to the inclined plane; this transfer of momentum to an orthogonal plane resembles that observed in the fluid chains generated by impinging fluid jets (Bush & Hasha 2004) or to the jets observed in shallow fluid flows at high Froude number (Edwards *et al.* 2008). A stream of fast-moving flow continues downstream of this, along the centreline of the flow. Far downstream, the centreline flow speed is approximately 0.11 ms^{-1}.

The thickness of the flow is of order 1 mm inside the shock, and 1 cm outside of it. This leads to Froude numbers of approximately 10 inside the shock, 1.4 in the fast-moving streams outside the shock, and 0.3 in the surrounding flow; the flow is therefore supercritical in a region including the shock, and transitions to subcritical flow downstream.

Figure 3 shows a time-sequence of the formation of the teardrop-shaped shock. The first material to strike the plane spreads into a thin radially-flowing layer (figure 3*a,b*). This layer is slowed by friction, and, upslope of the point of impingement, by gravity. The upslope flow becomes stationary approximately 0.25 s after the jet impact (figure 3*c*); this forms a shock in flow height that propagates inwards and wraps around the

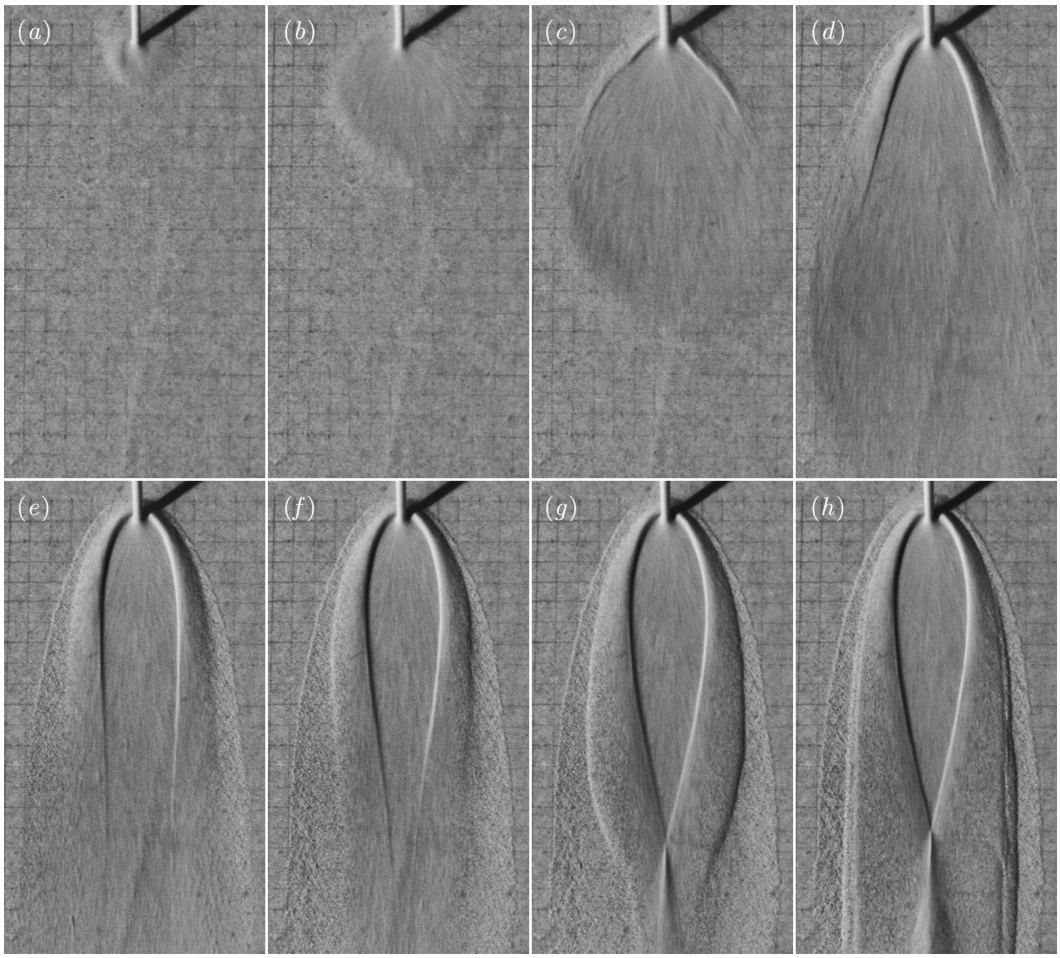

FIGURE 3. Time sequence of the formation of a teardrop-shaped shock, for $\zeta = 26.7^\circ$, $H_f = 30$ cm, $D = 15$ mm. Times after jet impact are: (a) 0.02 s, (b) 0.1 s (c) 0.26 s (d) 0.50 s (e) 1.0 s (f) 1.5 s (g) 2.0 s (h) steady-state. A movie showing the time-dependent evolution of this flow is available with the online version of this paper.

point of impingement (figure 3d–f) as the amount of granular material outside the shock increases. Unlike the case of impingement on a horizontal plane, material on both sides of the shock is flowing. The inward movement of the shocks causes them to collide after approximately 1.5 seconds, forming a closed shock. The slower material outside the shock forms a down-slope flow (figure 3g), which reaches a steady state (figure 3h).

In the initial stages of the flow, before the steady state is reached, a thin layer of stationary grains is deposited on the inclined plane outside the flowing region. These particles, labelled in figure 2, have no effect on the flowing region: they can be brushed away without affecting the flow. The interface between flowing and stationary grains

exhibits small stick-slip fluctuations in all flows. However, in the flows described up to section 6, these fluctuations have a negligible effect on the steady flow. Observation of the steady flows for 30 minutes showed continued small fluctuations, but no long-term evolution of the flowing region.

3.2. *Steady blunted jumps*

For shallower slope inclination angles, a second steady-state regime exists that displays the same radial flow inside a closed granular jump as before, but in which the shock is blunted, as shown in figure 4. The sharp vertex of the teardrop-shaped shock is replaced by a normal shock which lies across the slope. When the two streams of flow in the thicker layer of material adjoining the shock reach this normal shock, they are in part directed toward each other, following the line of the closed shock, and in part detach from the shock and decelerate rapidly to form part of the down-slope flow. The speed of flow downstream of the shock is about $0.07\ \mathrm{ms}^{-1}$.

In the centre of the cross-slope jump, a complex three-dimensional interaction between three flow streams is observed: the material from the inner region, flowing directly downstream, encounters both a normal shock and the components of the two streams that have been diverted toward one another. The flow at the shock overturns, and resembles a static continuously breaking wave. The overturning of the flow at the shock has some resemblance to the recirculation observed in two-dimensional propagating granular bores by Gray *et al.* (2003). As a result of this interaction between the streams, the downstream flow is thickest in two broad regions either side of a thin trench along the axis of symmetry, a configuration which persists in the flow downstream. For smaller ζ and greater H_f, the region enclosed by the hydraulic jump becomes wider in the y-direction, and shorter in the x-direction; in this case, two parallel trenches can be generated, forming a

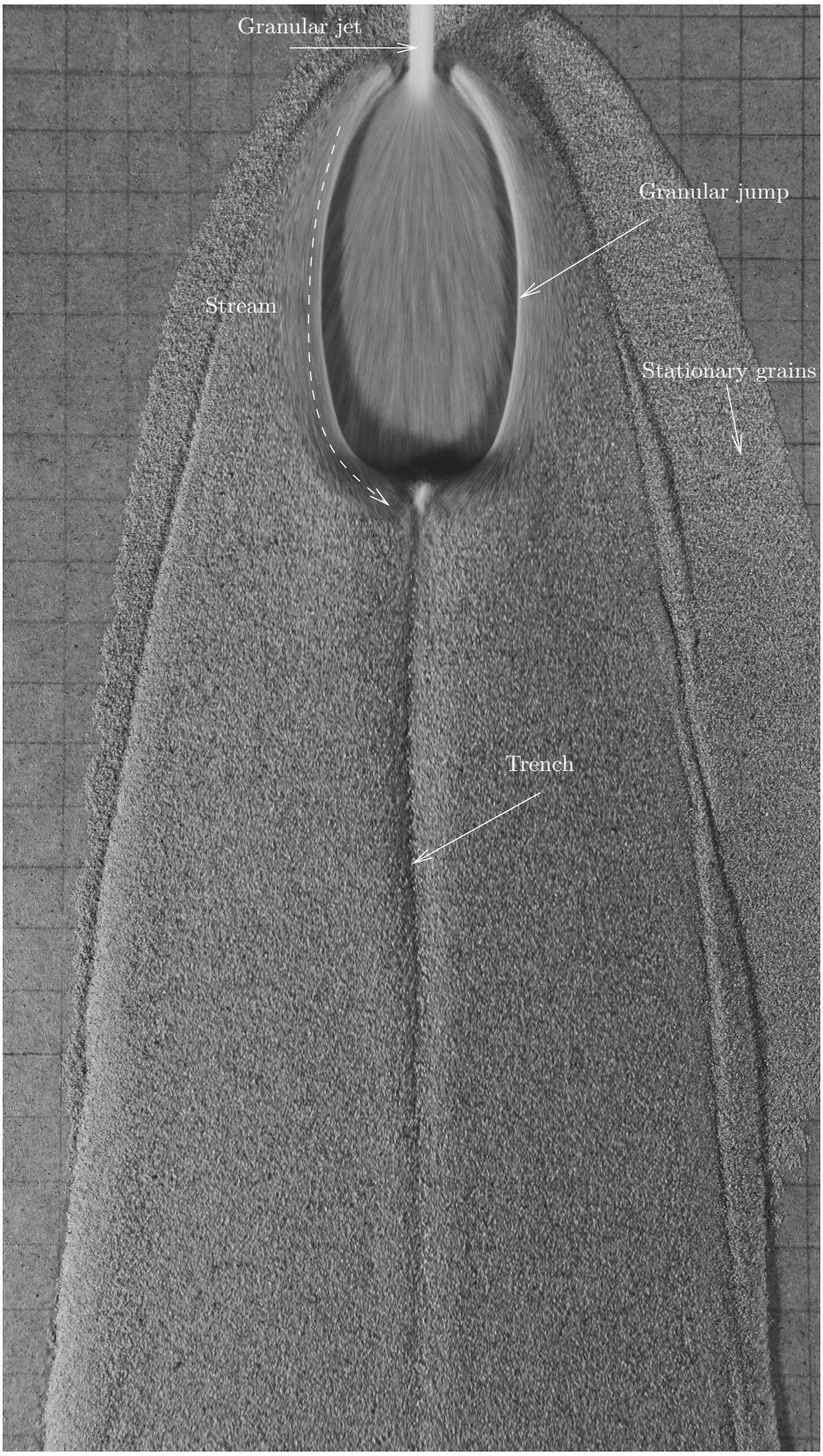

FIGURE 4. A blunted shock in sand, $\zeta = 25.4^\circ$, $H_f = 30$ cm, $D = 15$ mm. The shutter speed is 1/80 s.

w-shaped indentation in the downslope flow. A movie, available with the online version of this paper, shows the complex flow in this region.

A phase diagram of the flow regimes for $D = 50$ mm is shown in figure 5. Teardrop-shaped shocks (denoted by $\times$) are observed in all flows where $H_f > 10$ cm and $\zeta > 26.5°$; blunted shocks (denoted by $\circ$) are observed in a more limited range of slope angles, $24.5° \lesssim \zeta \lesssim 26.5°$ and only for $H_f > 9$ cm. We attribute the different behaviour in the two regimes to whether the Froude number is greater or less than unity in the material immediately downstream of the radial flow region. This was determined experimentally by introducing a small disturbance onto the flow, for example with the point of a pin; if the flow is subcritical, the disturbance propagates in all directions, whereas for supercritical flow, the disturbance is limited to a wedge downstream of the pin. For teardrop-shaped shocks, the flow on the downstream side of the shock vertex is supercritical. Here, information can propagate only downstream, which explains the lack of visible influence of the shock interaction on the upstream flow, and the consequent sharp vertex. For blunted shocks, the material becomes subcritical as it passes through the cross-slope section of shock. In this subcritical flow, the effect of the collision between the shocks can propagate upstream, leading to the curved shock observed in experiments. The correspondence of Froude number with the flow regime is consistent with the observation that teardrop shocks occur at steeper slope inclinations, where the flow on the plane is faster and thinner (and thus of higher Froude number) than at lower inclinations. The decrease with increasing H_f of the critical slope inclination angle separating teardrop-shaped from blunted shocks (figure 5) is also consistent with this hypothesis, since the velocity of the flow at the inflow increases with H_f.

3.3. *Other steady regimes*

In addition to the blunted and teardrop-shaped shocks, two further regimes of steady-state flow exist in which a shock is not present. In the first of these, observed when $H_f \lesssim 10$ cm, the flow velocity in the region surrounding the impingement point is still supercritical, but the shocks become sufficiently diffuse (that is, the variation in flow occurs over a sufficiently large region) that they are indistinguishable from the surrounding flow. This is consistent with the observation of Gray & Cui (2007) that shocks in granular materials become diffuse at low supercritical Froude numbers. The second regime occurs in the range of inclination angles $23^\circ \lesssim \zeta \lesssim 24.5^\circ$, when the flow is sufficiently deep that it is subcritical everywhere. Since supercritical flow is required for a hyperbolic shock to exist, this flow also displays no shocks. These steady flows without shocks are denoted by + signs in figure 5. Unsteady flows, observed for $\zeta \lesssim 23^\circ$ and denoted by $\square$, exhibit a wide range of complex behaviour which is discussed in section 6.

In addition to the hardboard surface of the inclined plane, the experiments were tried with two other surface types: a smooth perspex sheet, and a sheet of hardboard roughened by gluing a layer of sand to it. The teardrop-shaped shocks, as well as the steady and unsteady flows without shocks were observed on all surface types. On the roughened surface, blunted shocks were observed, with the transition between teardrop and blunted shock regimes occurring at $\zeta \approx 35^\circ$ and unsteady flows observed below approximately 30°. The increased friction on the roughened slope is responsible for the increase in slope angle required to balance friction in the steady flow downstream. On the perspex surface, the transition between teardrop-shaped shocks and unsteady flows occurs over a narrow range of slope angles close to 22°, with blunted shocks occurring only in this

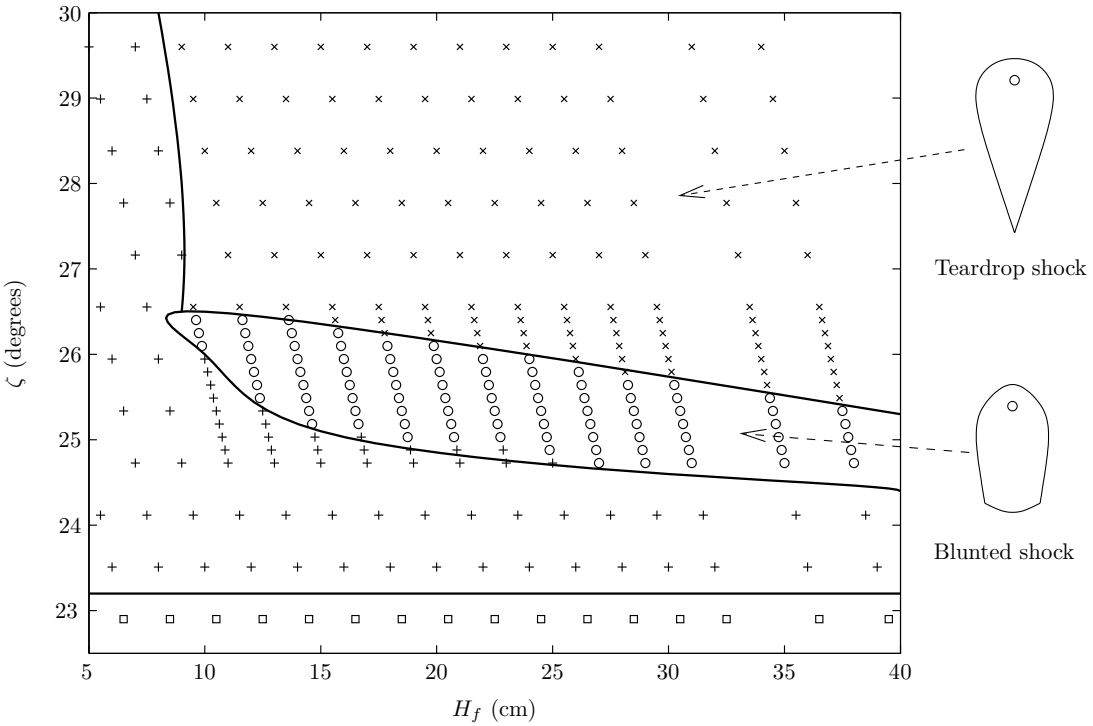

FIGURE 5. Experimental phase diagram, showing the dependence of flow regime on H_f and ζ, for $D = 15$ mm. Teardrop-shaped shocks are indicated by crosses ($\times$), blunted shocks by circles ($\circ$), and steady flows with no shock by plus signs ($+$). Unstable time-dependent flows are represented by squares ($\square$). All flows for $\zeta \gtrsim 23^\circ$ are steady.

small region of parameter space. This transition is consistent with a constant Coulomb friction coefficient for the flow over a smooth surface.

4. Friction law and impingement condition

4.1. *Friction law*

We seek to model the experimental flows using the shallow-layer avalanche model of (2.2–2.6). The use of this model is motivated by the shallowness of the flows in question, in which the aspect ratio of the flow is approximately 1/30. To close the system of equations, an expression for the basal friction coefficient μ is required. The basal friction was taken to be a constant by Savage & Hutter (1989) for Coulomb-frictional flows over smooth surfaces. For such a friction law, steady flows of uniform thickness are possible only at a single slope angle, when $\zeta = \tan^{-1}\mu$. More recently, Pouliquen (1999) performed

laboratory-scale experiments of flows of glass beads over a roughened bed, and observed steady uniform flows over a range of slope angles. They demonstrated a minimum height $\tilde{h}_{\rm stop}(\zeta)$ at which a steady flowing layer can exist on a slope inclined at an angle ζ, and found an empirical dependence of the ratio of flow height $\tilde{h}$ to $\tilde{h}_{\rm stop}$ on the Froude number,

$$Fr = \frac{|\mathbf{u}|}{\sqrt{h\epsilon\cos\zeta}} = \beta\frac{\tilde{h}}{\tilde{h}_{\rm stop}(\zeta)}\,, \tag{4.1}$$

where $\beta = 0.136$ is a measured constant for glass beads. In one-dimensional steady uniform flows, the cross-slope velocity $v = 0$ and the downslope source term $s_x = 0$, leading to the relation between the friction coefficient and slope angle

$$\mu = \tan\zeta\,. \tag{4.2}$$

Denoting the inverse of $\tilde{h}_{\rm stop}(\zeta)$ by $\zeta_{\rm stop}(\tilde{h})$, the function

$$\mu_{\rm stop}(\tilde{h}) = \tan\left(\zeta_{\rm stop}(\tilde{h})\right)\,, \tag{4.3}$$

leads, through the scaling law (4.1), to an equation for the friction coefficient

$$\mu = \tan\zeta = \mu_{\rm stop}(\tilde{h}_{\rm stop}(\zeta)) = \mu_{\rm stop}\left(\frac{\tilde{h}\beta}{Fr}\right)\,. \tag{4.4}$$

The form of the function $\mu_{\rm stop}$ is a fit to the experimental measurements of $\tilde{h}_{\rm stop}(\zeta)$, and takes the form of a transition between two friction angles ζ_1 and ζ_2, either

$$\mu_{\rm stop}(h') = \tan\zeta_1 + (\tan\zeta_2 - \tan\zeta_1)\frac{1}{1+h'/\mathcal{L}}\,, \tag{4.5}$$

as in Pouliquen & Forterre (2002), or in the Pouliquen (1999) form,

$$\mu_{\rm stop}(h') = \tan\zeta_1 + (\tan\zeta_2 - \tan\zeta_1)\exp(-h'/\mathcal{L})\,. \tag{4.6}$$

The friction angles used here are those measured by Pouliquen & Forterre (2002), $\zeta_1 = 21^\circ, \zeta_2 = 30.7^\circ, \zeta_3 = 22.2^\circ$. The parameter $\mathcal{L}$, which has the dimensions of length, depends on the granular material and surface properties of the plane and characterises the depth of flow over which a transition between the two friction angles ζ_1 and ζ_2 occurs. The friction law (4.4) is valid for flows in the steady regime where $\tilde{h} > \tilde{h}_{\rm stop}$, that is, for flows in which $Fr > \beta$.

For stationary material, the basal friction balances the lithostatic pressure and gravitational forces exactly, up to a maximum value corresponding to the coefficient of static friction $\mu = \mu_{\rm start}(\tilde{h})$. This is calculated, through (4.2), by measuring the maximum inclination angle at which a uniform layer of stationary material starts to move, and takes the form

$$\mu_{\rm start}(h') = \tan\zeta_3 + (\tan\zeta_2 - \tan\zeta_1)\frac{1}{1 + h'/\mathcal{L}}\,. \tag{4.7}$$

For flows of $0 < Fr < \beta$, we follow the method of Pouliquen & Forterre (2002) in interpolating between the static and steady-flow friction coefficients with a power function

$$\mu = \left(\frac{Fr}{\beta}\right)^{\gamma}(\mu_{\rm stop}(\tilde{h}) - \mu_{\rm start}(\tilde{h})) + \mu_{\rm start}(\tilde{h})\,, \tag{4.8}$$

where $\gamma = 10^{-3}$. The parameter $\mathcal{L}$ provides a convenient length-scale with which to non-dimensionalise the depth of the flow. We take $\mathcal{L} = 10$ mm, and non-dimensionalise the flow depth by setting $H = \mathcal{L}$ in the scalings (2.1). The horizontal length-scale L is chosen to be 0.5 m (a typical length of the closed granular jump and associated rapidly-flowing streams), giving $\epsilon = 1/50$.

The choice of a Pouliquen-type friction law rather than a Coulomb one is motivated by our observation of both steady uniform flows over a range of slope angles and a critical flow depth, dependent on slope angle, below which steady flow is not observed. In our

simulations of the experiment only small differences are found between results obtained with the friction law for glass beads, defined in (4.6) and (4.8) and a modified version for sand (Forterre & Pouliquen 2003, equation 4.17).

Close-up photographs of the fast radially flowing region inside the shock show that the flow is only a few grains thick. This is consistent with the observations of Boudet *et al.* (2007), for the impingement of a jet onto a horizontal plane, where the flow is approximately four grain diameters deep. The flow in this region appears less dense than that in the more slowly flowing regions outside the shock, and than the material at the point of impingement itself. In the region of thin flow, many particles are not in contact with any others: the assumption of an incompressible continuum is therefore invalid, and neither a lithostatic pressure nor a Pouliquen-type friction law would be expected here. These discrepancies are minimised by the small effect of internal pressure and basal friction in this region; the transport terms of (2.3–2.4) become large compared to the pressure gradient and frictional source terms. The exact choice of pressure and frictional models therefore has little effect in this region. Furthermore, the assumption of incompressibility can be relaxed by considering h not as the flow height, but as a measure of the amount of mass at a given point, as is possible when surface-gradient generated pressures are negligible. While we might not expect h to accurately represent the flow height in this region of sparse flow (indeed, a flow height may not even be clearly defined), the mass and momentum fluxes are predicted correctly. Since these are the quantities which determine the shock relations, the use of the shallow avalanche model in the fast-moving region is acceptable for predictions of the shock position.

We model the internal stresses in the granular material as an isotropic lithostatic pressure, in contrast to the Mohr-Coulomb rheology used by Savage & Hutter (1989). Simulations of the current problem have been compared with the earth-pressure coef-

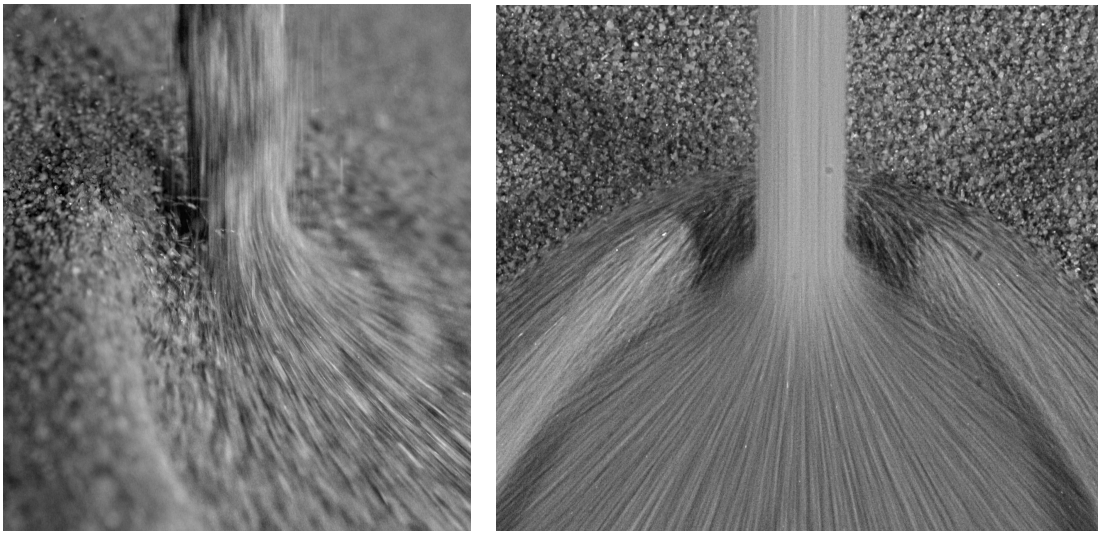

FIGURE 6. Photographs of impingement region, viewing across the slope (a) and normal to it (b). The vertically falling jet of material is converted to a thin, radial flow on impact with the plane. Above the point of impingement, particles are held almost stationary by the dynamic pressure of material flowing uphill from the point of impingement.

ficient firstly set to unity (e.g. Gray *et al.* 2003) in the isotropic case, and secondly determined by the two-dimensional formulation of Iverson & Denlinger (2001) in the case of a Mohr-Coulomb rheology. In the current problem, only small quantitative differences exist between the results of the two models; for simplicity the isotropic pressure assumption is made.

4.2. *Region of impingement*

The region of impingement, in which the flow transitions from a vertical jet to flow across the inclined plane, is shown in detail in figure 6. The flow here is fully three-dimensional, and the approximations made in the assumption of shallow-layer flow are invalid. We seek an alternative model for the flow in this region, and match it to the shallow-layer model, which is valid elsewhere, by applying appropriate boundary conditions on an interface separating the two model regions.

As in the case of the normal impingement examined by Boudet *et al.* (2007), a smooth transition from a falling jet of material to thin radial flow over a plane is observed,

but details of the three-dimensional flow in the region of impingement are unknown. In the case of normal impingement, the problem resembles the high aspect-ratio limit of granular column collapse, a problem which has received extensive study (Lajeunesse, Mangeney-Castelnau & Vilotte 2004; Lube *et al.* 2004; Doyle *et al.* 2007). Contact dynamics simulations of this problem for column aspect ratios up to 17 (Staron & Hinch 2005) predict a smooth transition from falling to thin-layer flow. This is consistent with our experimental observations for a continuous stream. Using a transparent plane to observe the flow from underneath, a single stagnation point forms beneath the jet and is surrounded by radial flow. For oblique impingements, the qualitative behaviour of the flow is similar, with a stagnation point observed under the jet impact region, surrounded by radial flow. The mass flux of the radial flow is no longer axisymmetric however, and becomes dependent on θ, the angle of a plane polar coordinate system in the xy-plane centred at the stagnation point.

In the absence of a granular rheology for this flow, we make the assumption that the flow in the region of impact can be modelled as an inviscid, irrotational, incompressible fluid. Under this assumption, the flow admits a solution which describes the transition of a jet of fluid to a radial flow across a plane (figure 7*a*). Our choice of this model is motivated by the qualitative similarity between its predictions and experimental observations. The granular impingement is subject to frictional energy losses, which are neglected in the ideal fluid model. An estimate of these losses in the case of normal impingement is given by Boudet *et al.* (2007), who found experimentally that the velocities in the radial flow generated by the normal impingement of a granular jet were 20–50% lower than would be expected if energy were conserved in the region of impingement. Therefore, while the ideal fluid model is expected to correctly predict the distribution of granular material onto the plane, a quantitative link to the velocity of the falling jet is not attempted.

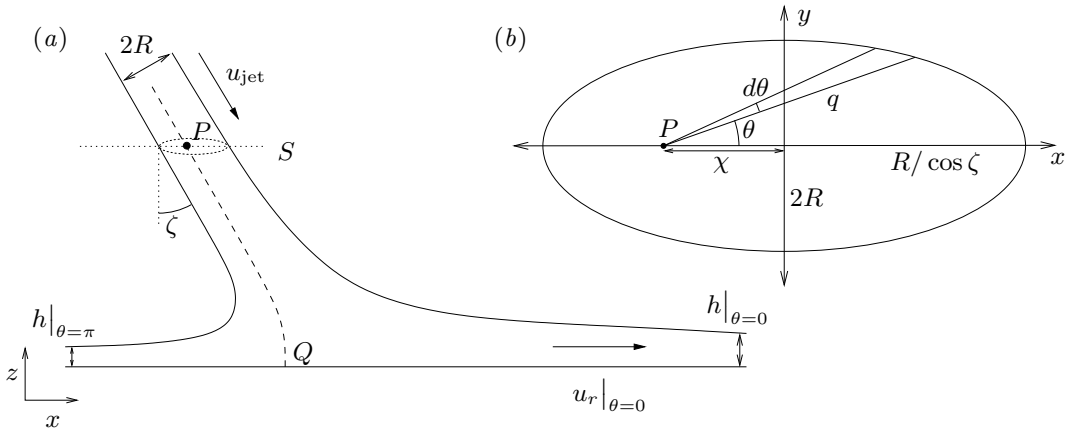

FIGURE 7. (*a*) Cross-section of the impingement region in the plane $y = 0$. The separation streamline is shown as a dashed line. (*b*) Section of the jet in the plane S, parallel to the inclined plane

The oblique impingement of a circular jet of inviscid fluid on a plane was first described by Schach (1934). More recently, the analogous situation of two symmetric colliding jets has been considered, both experimentally (Taylor 1960) and theoretically (Hasson & Peck 1964). The flow contains a stagnation point Q on the plane, connected to the incoming jet by a separation streamline. We consider a section of the jet through a plane S, parallel to the xy-plane and far from the impingement region (figure 7*b*), where the flow is parallel to the jet axis. The jet velocity through S is denoted $u_{\rm jet}$. The jet is cylindrical and of radius R, and thus its intersection with S is an ellipse of major axis $2R/\sin\zeta$ in the x-direction and minor axis $2R$ in the y-direction. The intersection point of the separation streamline with S is denoted by P. Symmetry about the plane $y = 0$ implies that P must lie on this plane, at a distance χ from the centre of the ellipse. The radial distance from the origin on the inclined plane is denoted r, and the radial velocity u_r.

Taylor (1966) showed that a full calculation of the three-dimensional flow in the region of impingement is required to determine how the outflow mass and momentum fluxes are distributed in θ. We follow Hasson & Peck (1964) in assuming that flow which enters the impingement region in the angular segment $\mathrm{d}\theta$ (figure 7*b*) remains in this segment throughout the flow. This approximation is justified by good quantitative agreement with

experimental results (e.g. Kate *et al.* 2007), and allows a solution for the outflow to be determined using global balance arguments alone. On this basis, we equate the mass flux through S in a segment $\mathrm{d}\theta$ with the mass flux leaving the impingement region on the inclined plane in the same segment, giving

$$q\,\mathrm{d}\theta\,\frac{q}{2}u_{\mathrm{jet}}\cos\zeta = r\,\mathrm{d}\theta\,hu_r, \tag{4.9}$$

where $q(\theta)$, defined in figure 7(b), is related to χ by the equation for an ellipse,

$$(q\sin\theta)^2 + (q\cos\theta - \chi)^2\cos^2\zeta = R^2. \tag{4.10}$$

For radial flow far from the impingement region, the flow velocities in the z direction are negligible. Applying Bernoulli's equation to a surface streamline then implies that the radial flow velocity u_r is equal to the jet velocity u_{jet} for all θ. The gravitational term in Bernoulli's equation can be neglected because the height of the impingement region H_{ir} is much smaller than the funnel height H_f; the fractional change in velocity due to gravity within the impingement region, which scales like H_{ir}/H_f, is therefore small. With velocity in the radial flow equal to u_{jet}, (4.9) simplifies to

$$hr = \frac{q^2}{2}\cos\zeta. \tag{4.11}$$

The remaining unknown χ is calculated from the conservation of momentum in the x-direction. Considering x-momentum fluxes through S and in the radial flow gives

$$\rho\pi R^2 u_{\mathrm{jet}}^2\sin\zeta = \int_0^{2\pi} h\rho u_r^2\cos\theta\, r\,\mathrm{d}\theta \tag{4.12}$$

which simplifies to

$$\pi\tan\zeta = \int_0^{\pi}\left(\frac{q}{R}\right)^2\cos\theta\,\mathrm{d}\theta\,. \tag{4.13}$$

Using (4.10) to evaluate q in terms of χ, if

$$\chi = R \tan \zeta \tag{4.14}$$

then

$$q = \frac{R \cos \zeta}{1 - \sin \zeta \cos \theta} \,. \tag{4.15}$$

It can be shown that this expression for q satisfies (4.13), providing a solution for χ. Through (4.10) and (4.11), the solutions for $\mathbf{u}$ and h at a distance r from the point of separation are:

$$\mathbf{u} = (u_{\text{jet}} \cos \theta, u_{\text{jet}} \sin \theta) \;, \tag{4.16}$$

$$h = \frac{R^2 \cos^3 \zeta}{2r \left(1 - \sin \zeta \cos \theta\right)^2} \,. \tag{4.17}$$

This solution reproduces the observed stagnation point and, qualitatively, the dependence on θ and ζ of the radial mass flux for oblique impingement.

It remains to match the analytical solution found for the impingement region to the flow elsewhere, modelled by the shallow-layer equations (2.2–2.4). The values for $\mathbf{u}$ and h given by (4.16, 4.17) describe the solution of the inviscid jet impingement problem when r is sufficiently large that flow velocities in the z direction are negligible. In addition, (4.16, 4.17) are solutions of the shallow layer model in the limits of no horizontal pressure gradients and source terms; these two limits are approached in the fast-moving flow of the impingement region. The boundary between the analytical solution in the impingement region and the surrounding shallow-water model is therefore chosen to be sufficiently far from the point of impingement that flow velocities in the z direction are small, but sufficiently close to the point of impingement that frictional and pressure-driven accelerations on the flow within this region can also be neglected.

This assumes that the flow within the impingement region is not affected by the flow outside it. This is invalid if the flow is subcritical anywhere on the interface separating the two modelling regions, since information can then propagate from the flow outside back into the impingement region. The solution of the inviscid jet impingement problem (4.16, 4.17) has Froude number increasing without bound for increasing radius; the condition of supercritical flow is therefore satisfied at sufficiently large r.

5. Numerical method and results

The system (2.2–2.4) is a set of nonlinear hyperbolic conservation laws that can be written in vector form

$$\frac{\partial \mathbf{w}}{\partial t} + \frac{\partial \mathbf{f}(\mathbf{w})}{\partial x} + \frac{\partial \mathbf{g}(\mathbf{w})}{\partial y} = \mathbf{s}\,, \tag{5.1}$$

where $\mathbf{w} = (h, hu, hv)^T$ is the vector of conserved variables, and $\mathbf{s} = (0, hs_x, hs_y)^T$. The flux functions $\mathbf{f}$ and $\mathbf{g}$ are given by

$$\mathbf{f} = \begin{pmatrix} hu \\ hu^2 + \epsilon h^2/2 \\ huv \end{pmatrix}, \quad \mathbf{g} = \begin{pmatrix} hv \\ huv \\ hv^2 + \epsilon h^2/2 \end{pmatrix}. \tag{5.2}$$

Several techniques exist for the numerical solution of such systems of conservation laws (LeVeque 1992). We elect to solve the equations using the finite-volume method of Jiang & Tadmor (1998), an extension to two-dimensional Cartesian grids of the Non-Oscillatory Central scheme of Nessyahu & Tadmor (1990). These methods are high-resolution, in the sense that flux limiters are used to obtain second-order accuracy away from the shocks, while remaining non-oscillatory in the region of discontinuities. For the numerical solutions presented here, the extended 'MinMod' limiter (Jiang & Tadmor 1998, equation 3.1) has been used with parameter $\theta = 2$. The choice of conserved variables in the vector

w, in conjunction with the non-oscillatory scheme, ensures that the numerical method is *shock-capturing*. Such methods are required to handle correctly the discontinuity in solution at a granular jump (Tai *et al.* 2001, 2002; Gray *et al.* 2003).

Downstream flow conditions strongly affect the formation of oblique shocks in granular flows (Gray & Cui 2007). In this problem, there are both sub- and super-critical regions present at the downstream boundary of the numerical domain, requiring either one or zero boundary conditions respectively (Weiyan 1992, page 111). This numerical boundary is treated by constructing a row of ghost cells outside the domain, with values determined by a linear extrapolation of the two final rows of interior cells, which is appropriate for both subcritical and supercritical outflow (LeVeque 2002, page 131). This boundary is sufficiently far downstream that the numerical solution is independent of its exact position. The numerical domain has sufficient extent in the y-direction that all material leaving it does so through the downstream boundary.

In order to apply the boundary conditions at the matching interface between the solution for the impingement region given by (4.16, 4.17) and the shallow-layer model elsewhere, we enforce (4.16, 4.17) in any finite volume cells which lie within a circular region of radius $R_{\rm imp}$, centred on the stagnation point Q. Since the impingement region solution and shallow-layer model solutions coincide here, the numerical solutions are expected to be insensitive to the point at which the two solutions are matched, provided that the conditions for the matching are satisfied. These conditions are that the velocities in the z-direction in the inviscid fluid model and horizontal pressure gradients and source terms in the shallow-layer model are negligible, and that the flow is supercritical everywhere on $r = R_{\rm imp}$. The value $R_{\rm imp} \approx 2R$ has been chosen, which satisfies these conditions for the simulated flow parameters. As expected, our numerical results are insensitive to the exact value of $R_{\rm imp}$.

5.1. *Teardrop-shaped shock*

Figure 8 shows a numerical solution of (2.2–2.4) exhibiting a steady teardrop-shaped shock, comparable to that seen in the experimental flow of figure 2. The slope inclination angle and funnel diameter are the same as those in the experimental flow, and the axes of figure 8 cover the same region as that shown in figure 2.

The unknown energy loss in the impingement region means that the funnel heights H_f in numerical solutions are not directly comparable to those in the experiments. Instead the speed of the radial flow inside the shock is compared. Under the ideal fluid model for the impingement region, (4.16) implies that the speed of flow leaving the impingement region on the inclined plane is $u_{\rm jet}$. Experimentally, we estimate this velocity to be approximately 0.99 ms^{-1} in figure 2: we therefore use $u_{\rm jet} = 0.99$ ms^{-1} for the numerical solutions in figures (8–10).

Figure 8(a) shows the location of the shock as a black line, with streamlines of the flow in grey. The region in which the flow is supercritical is shaded. The numerical solution reproduces well the region of fast radial flow surrounding the point of impingement (indicated by radial streamlines), the teardrop-shaped shock and the shape of the flowing region. The shock length is 0.28 m, close to the experimental result of 0.27 m.

The shaded region of supercritical flow outside the shock shows that the two supercritical streams on either side of the teardrop merge at the shock vertex to form a single stream. This is consistent with the experimentally observed region of supercritical flow in figure 2, which approximately corresponds to the region of motion blur. The streamlines in this region, which follow the line of the shock, further resemble the experimental flow. The structure of these streams is visible in figure 8(c), which shows the values of the flow variables u (dashed line) and h (solid line) along a cross-section at $x = 0.1$ m, through the closed shock. Inside the shock (which occurs at $y = \pm 0.04$ m), $u \approx 0.99$ ms^{-1} as

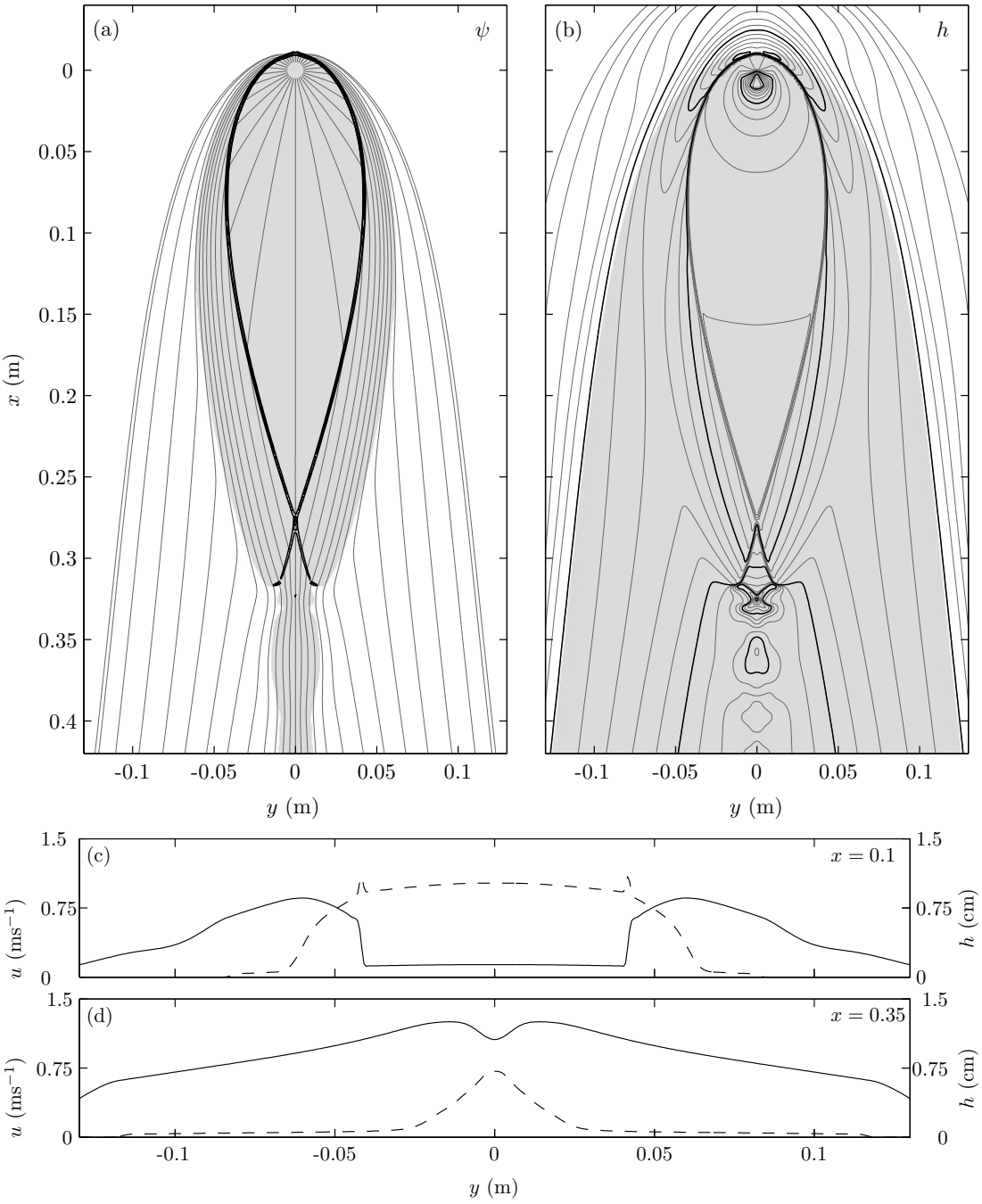

FIGURE 8. Steady-state numerical solution for ζ=26.7°, $u_{\text{jet}} = 0.99$ ms^{-1}, $D = 15$ mm. The axes correspond to the same regions shown in figures 2 and 4. In (a), the shading indicates supercritical flow ($Fr > 1$). The grey lines are streamlines, and the thick black line indicates the region of strongly converging flow velocity, an identifying feature of the shock. In (b), contours are of flow height, at intervals of 1 mm, with dark contours at intervals of 5 mm. Shading indicates the flowing region of material. Figures (c) and (d) show cross-sectional plots of flow variables, for $x = 0.1$ m and $x = 0.35$ m respectively. Down-slope velocity u is indicated by a dashed line and flow depth h by a solid line.

expected, and $h \approx 1.3$ mm, close to the experimental estimate of $h = 1$ mm. Across the shock, while h increases rapidly to about 6.5 mm, u is nearly continuous. (The peak in u at the location of the shock is a numerical artifact caused by the non-conservative form of u.) The continuity of u is due to the jump relation (2.9) which implies that velocity tangential to the shock (which is nearly in the downslope direction at $x = 0.1$ m) is continuous. It is this continuity of tangential velocity which causes the fast-moving streams of material to exist outside the shock. A substantial shear exists in the stream, as u decreases by an order of magnitude to approximately 0.05 ms^{-1} over 2.5 cm. At the vertex of the shock, the numerical solution exhibits a pair of shock reflections, leading to a weakening stream of shock interactions and reflections in the supercritical flow downstream of the shock vertex. The structure of these shocks resemble those described for supercritical shallow-water flows by Akers & Bokhove (2008). Experimentally, the flow in the region below the shock vertex is complicated by the formation of a spout, which is outside the scope of the thin-layer model (Edwards *et al.* 2008), but some evidence of a shock reflection, forming a triangular region downstream of the shock vertex, can be seen in figure 2. The extended chain of shocks below this is not observed in our experimental flows.

The flow thickness is shown by the contours in figure 8(b). The rapid increase in flow height across the teardrop-shaped shock is evident, as is the variation in thickness downstream of the shock vertex caused by the chain of shock interactions. The shaded region in figure 8(b) indicates flowing material. Surrounding and upslope of the flowing region, a region of stationary (unshaded) material is present. This is consistent with the location of stationary material in experimentally observed flows; material above the point of impingement is held stationary by the pressure of the upstream flow (figure 6), while

a thin layer of stationary material with $h \leqslant h_{\mathrm{stop}}$ surrounds the flowing region further down the plane (figure 2).

Figure 8(d) shows a cross-section at $x = 0.35$ m, through the flow just downstream of the shock. For $0.03 < |y| < 0.125$ m, u varies between $0.08\ \mathrm{ms}^{-1}$ and $0.04\ \mathrm{ms}^{-1}$. These velocities are within 20% of the velocity of a steady uniform down-slope flow of the same thickness profile (obtained from h by solving (4.4) for u). Along the centreline of the flow, at $x = 0.35$ m, the velocity is significantly larger at $0.7\ \mathrm{ms}^{-1}$, eight times faster than the steady uniform flow speed. This is part of the supercritical region downstream of the shock vertex in figure 8(a), and reflects the rapidly moving stream observed in experiments. Far downstream, the numerical prediction of centreline velocity is $0.12\ \mathrm{ms}^{-1}$, close to the experimental measurement of $0.11\ \mathrm{ms}^{-1}$.

The time-dependent flow which leads to the steady state shown in figure 8 is shown in figure 9. The evolution to the steady solution bears a strong resemblance to the experimentally observed transient flow in figure 3: the material upstream of the impingement point stagnates and a shock forms, separating the inner fast-moving region from the slower flow surrounding it. The shock propagates downslope and wraps around the radial flow region, eventually closing at the downstream vertex. This propagates back towards the impingement point until the flow reaches a steady state. As in the experimental observations, a region of stationary particles is formed outside the flowing region in the numerical solution in the initial stages (figure 8a–c) of the flow.

5.2. *Blunted shock*

Figure 10 shows a numerical solution at a lower inclination angle of $\zeta = 24.5°$, resembling the blunted shock regime observed experimentally (figure 4). In order to produce a comparable blunted shock, the slope angle in figure 10 is 0.9° lower than that in figure 4; we discuss this discrepancy in section 5.3. The shock in figure 10 is not closed at a

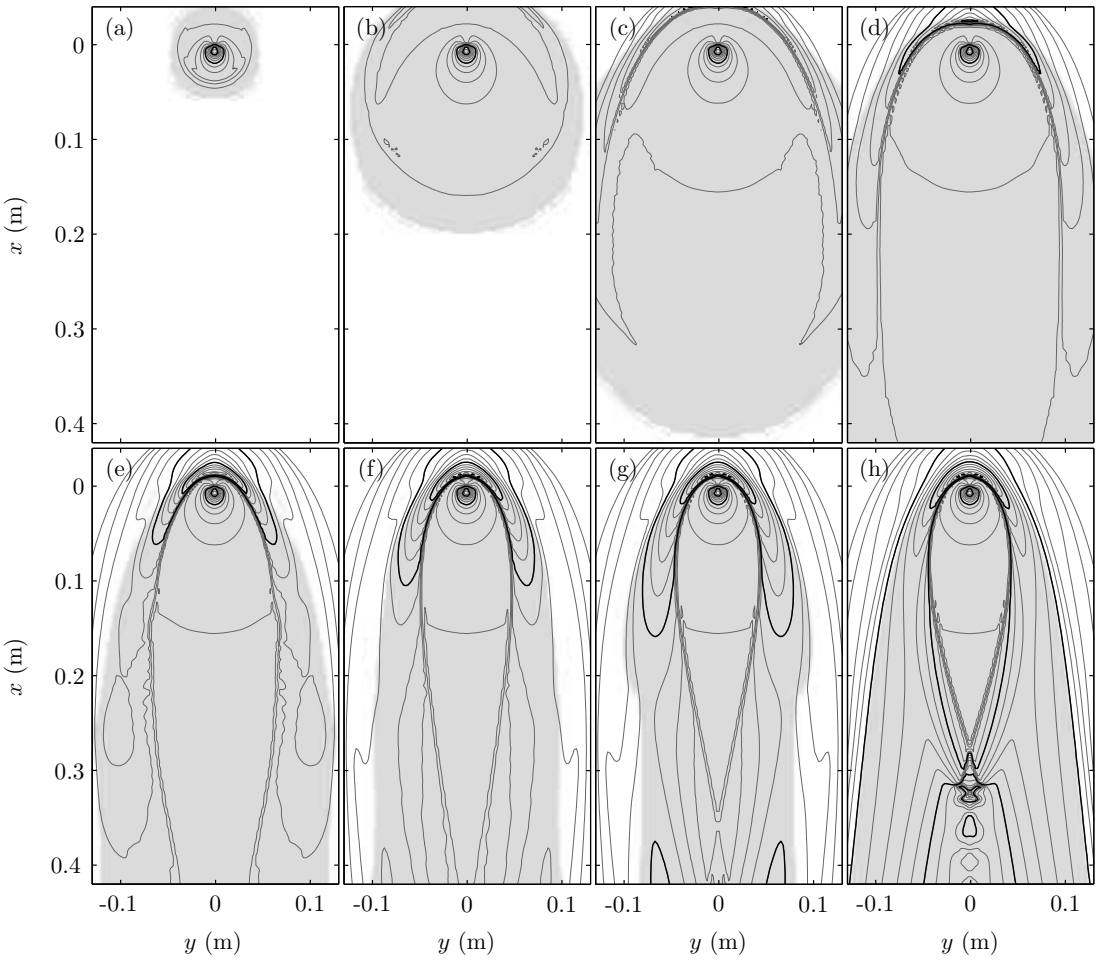

FIGURE 9. Time-sequence of the numerical solution of figure 8, with ζ=26.7°, $u_{\rm jet} = 0.99$ ms^{-1}, $D = 15$ mm. Contours and shading have the same meaning as in figure 8(b) The times after jet impact in each sub-figure are in the same ratio as those in figure 3: (a) 0.02, (b) 0.1, (c) 0.26, (d) 0.50, (e) 1.0, (f) 1.26, (g) 1.76, (h) steady-state. A movie showing the time-dependent behaviour of this solution is available with the online version of this paper.

sharp vertex, but by a curved shock lying across the slope. A transition from supercritical to subcritical flow occurs across this cross-slope shock, indicated by the shading in figure 10(a). For the thin-layer granular avalanche equations (2.2–2.4), Gray & Cui (2007) (p.121) show that such a transition implies that the shock is a strong shock. The strong shock meets the pair of shocks surrounding the point of impingement at shock interaction points. Each of these is the triple point of a Mach reflection, with the strong cross-slope shock forming the Mach stem. Two further line discontinuities are generated at each

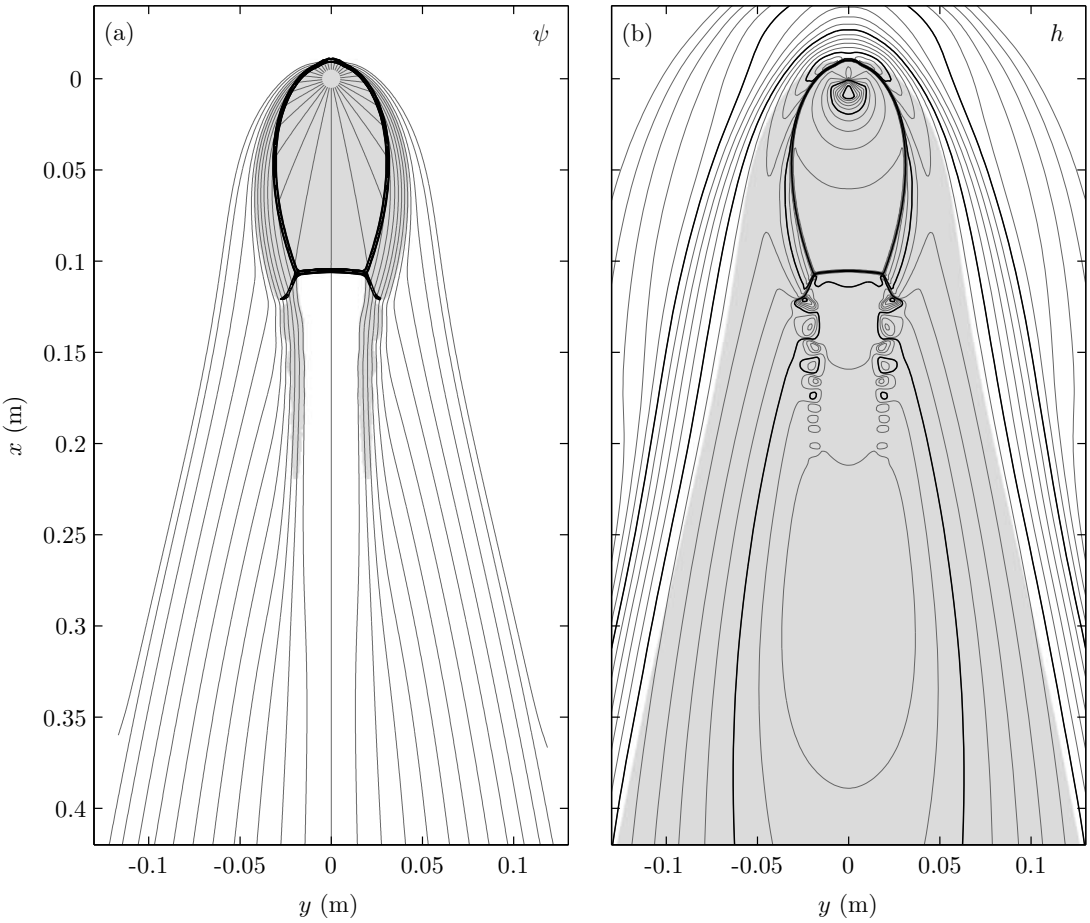

FIGURE 10. Numerical solution for ζ=24.5°, $u_{\rm jet} = 0.99$ ms^{-1}, $D = 15$ mm. The flow has reached the steady state. The meaning of contours and shading for (a) and (b) is as in figure 8(a) and (b) respectively. A movie showing the evolution to this steady state is available with the online version of this paper.

triple point, one a reflected shock and one a contact discontinuity. These are visible in figure 10(a), the reflected shock as a thick black line, and the contact discontinuity as the inner edge of the two streams of supercritical flow which continue downstream of the strong shock. As in the case of a teardrop shock solution, a chain of weaker shock reflections exists in these two streams, which are too weak to be indicated as shocks on figure 10(a), but are clearly visible in the flow height contours of figure 10(b). The flow downstream of the strong shock was measured to be 0.07 ms^{-1} in the experiment of figure 4. The numerical simulation is consistent with this, predicting $u = 0.055$ ms^{-1} on the

centreline immediately downstream of the shock at $x = 0.11$ m, rising to $u = 0.081$ ms^{-1} at $x = 0.25$ m.

A feature shown clearly in figure 10(a) (and which is present, but less clear, in figure 8a) is the structure of the two streams surrounding the shock. Within the region of the stream, the flow is supercritical (shaded in figure 10a) and streamlines are nearly parallel to the shock. This phenomenon is caused by the effect of the shock on the flow velocity: the rapid decrease in velocity normal to the shock as material goes through the shock, together with the continuity of velocity tangential to the shock, results in material that has been through the shock travelling nearly tangential to it. Outside of the supercritical streams, the streamlines diverge sharply from being parallel to the shock, and assume their form for the flow far downstream.

One difference between the numerical solutions and experimental observations of figures 10 and 4 respectively is in the presence of a shock interaction point in the solution of the model equations, where instead a strongly curved shock is observed experimentally. This is likely to be due to either an effect of the granular rheology, or to the three-dimensional breaking wave observed at the shock in experiments. A related feature in experimental flows, not present in numerical solutions, is the thin trench in the flow which persists downstream. We attribute the formation of the trench in experiments to the complex three-dimensional flow in the shock region, which is not present in the depth-integrated model. However, even if a perturbation in height is introduced artificially into a time-dependent numerical solution, the perturbation will dissipate in a wave-like manner; by contrast, in experimental flows the perturbation persists and is advected downstream. This suggests that the persistence of the trench is due to the actual rheology differing from the modelled lithostatic pressure distribution. The lack of disturbance of the trench, and of grains on the surface of thicker experimental flows such

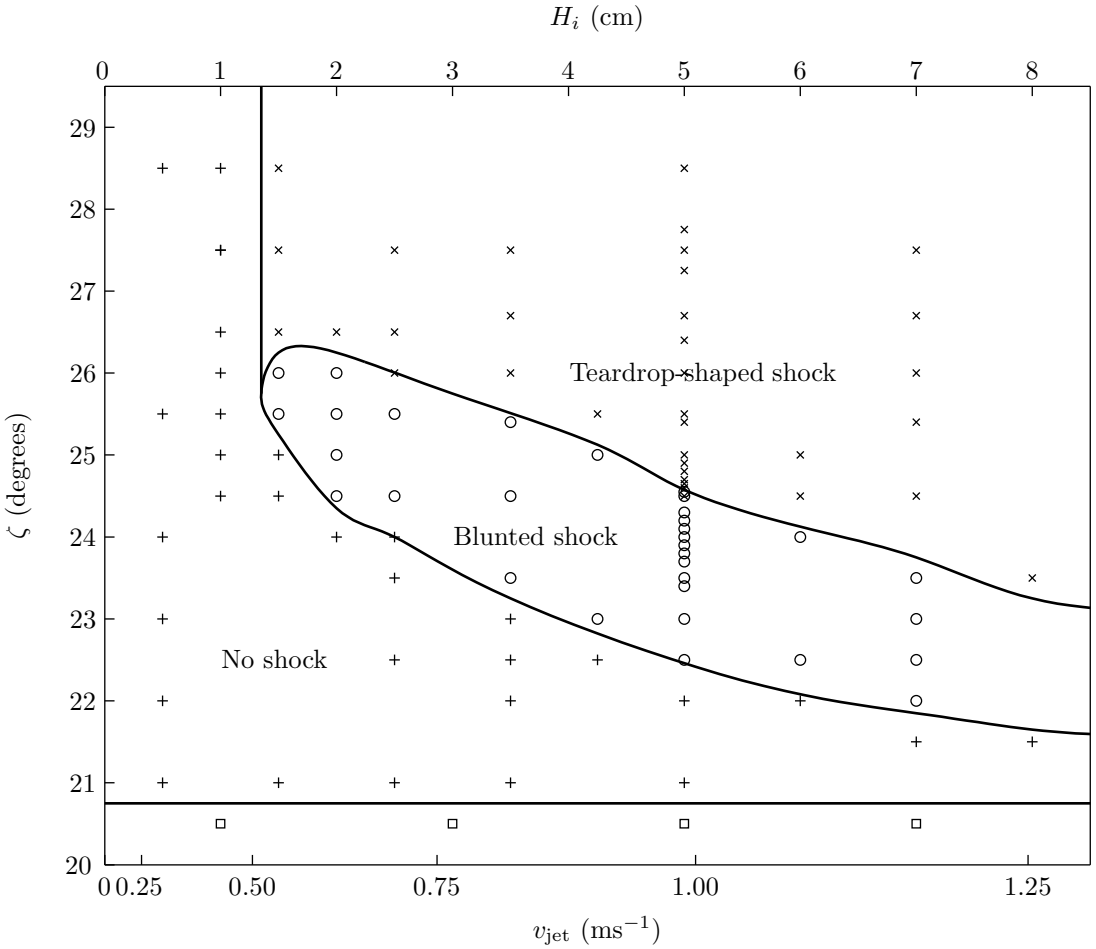

FIGURE 11. Numerical phase diagram, showing the dependence of flow regime on u_{jet} and ζ, for $D = 15$ mm. As before, teardrop-shaped shocks are indicated by crosses ($\times$), blunted shocks by circles ($\circ$), and steady flows showing no shock by plus signs ($+$). Time-dependent flows are represented by squares ($\square$). All flows for $\zeta \gtrsim 21^\circ$ are steady.

as that in figure 4, suggests that very little shear occurs near the surface, the shear being concentrated instead in a thin region at the base.

5.3. *Dependence on ζ and u_{jet}*

A phase diagram of flow regimes observed in the numerical solutions for $D = 15$ mm is shown in figure 11, which is comparable to the experimental phase diagram in figure 5. The four regimes of flow (unsteady flows, steady flows without a shock, steady teardrop-shaped shocks, and steady blunted shocks) and their relative locations on the phase diagram are all reproduced by the shallow-flow model.

The numerical results are parameterised by u_{jet}, the speed of flow exiting the impingement region in (4.16). In the experiments, this velocity is unknown, but is dependent on the funnel height H_f. To aid comparison between figures 5 and 11, we plot figure 11 with the effective funnel height H_i required to generate flow exiting the impingement region at u_{jet}. Assuming a freely falling jet (in which the grain acceleration is g), and no loss of energy in the impingement region, this effective height is

$$H_i = \frac{u_{\mathrm{jet}}^2}{2g}\,. \tag{5.3}$$

The energy loss in the impingement region causes H_i to be significantly smaller than the corresponding experimental H_f: for a flow speed exiting the impingement region of $0.99\ \mathrm{ms}^{-1}$ as measured for the flow in figure 2, $H_i \approx 5$ cm, whereas $H_f = 30$ cm.

The model solutions reproduce the experimental result of a single inclination angle dividing steady and unsteady flows, and (for sufficiently large ζ) a single value of H_i separating flows with teardrop-shaped shocks and flows with no shocks. The numerical solutions also correctly predict that as H_i increases, blunted shocks are observed over a shallower range of slope angles, though this effect is more pronounced in numerical simulations than in experiments. The overestimate could be attributed to an increasing proportion of the energy of the granular jet being dissipated in the impingement region with increasing H_i. In general, the numerical solutions predict the occurrence of flow regimes at lower slope angles than those measured experimentally. Such a difference is to be expected, since our grains and the inclined plane surface roughness are not identical to those used by Pouliquen & Forterre (2002) in the measurements of the friction law.

While the regimes of teardrop-shaped and blunted shocks are closely reproduced by numerical solutions, the regimes of unsteady flow and of steady flow without a shock are modelled less well. Experimentally, when H_i is sufficiently low, the flow velocity is too

small to create a clear shock and a diffuse transition to down-slope flow is observed. In the numerical solutions, rheological effects that would cause the shocks to become diffuse are not modelled, and we do not observe these smooth solutions. Instead, the size of the predicted shock continues to decrease with H_i, to the point where the shock reaches the diameter of the impinging jet. In figure 11, we mark solutions as having no shock if either the shock width or length is smaller than the diameter of the impinging jet. Flows with no shock also occur experimentally when ζ is sufficiently small, in which the flow is subcritical everywhere, including at the point of impingement. In numerical solutions of these flows, a subcritical flow with no shocks is observed everywhere in the domain, apart from in the impingement region, where the model of section 4.2 is applied. While this model of the impinging jet is not appropriate for flows which are subcritical at the impingement point, it nonetheless provides the correct mass flux to a subcritical flow.

The regimes in the numerical phase diagram are robust to changes in the parameters of the friction law. While the values of ζ and H_i for which different regimes occur vary with the details of the friction law, as does the size of the shock, the occurrence and relative position in the phase diagram of the four flow regimes is insensitive to the precise formulation. This is consistent with the experimental observation of blunted and teardrop-shaped shocks in a range of granular materials, particle sizes and rough surfaces.

Figure 12 shows numerical predictions and experimental measurements of the shock length (the distance from the impingement point to the lowest point of the shock). The experimental results are for $H_f = 30$ cm, and the numerical solutions at the corresponding $u_{\mathrm{jet}} = 0.99\ \mathrm{ms}^{-1}$.

An approximately linear relationship between shock length and slope angle is observed experimentally. The numerical predictions are in quantitative agreement with experimental measurements at steeper slope angles, where the flow is well into the teardrop-shaped

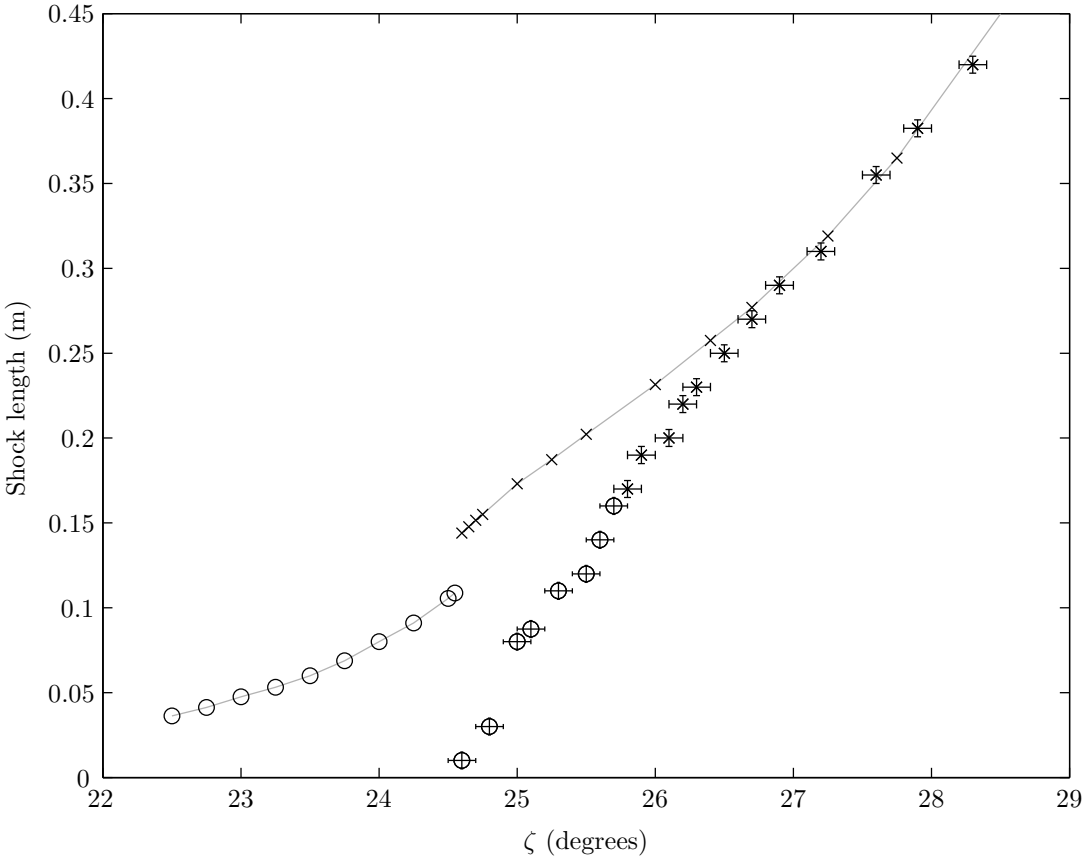

FIGURE 12. Experimental measurements and numerical predictions of the shock length, against slope angle, for $D = 15$ mm, $H_f = 30$ cm (experimental), $u_{\text{jet}} = 0.99$ ms^{-1} (numerical). Experimental measurements are indicated by symbols with error bars, and numerical results are joined by a grey line. A cross ($\times$) indicates a teardrop-shaped shock, and a circle ($\circ$) a blunted shock.

shock regime. At lower slope angles, the discrepancy between numerical and experimental results at lower slope angles is due, as before, to the difference between particle and surface properties in our experimental setup, and in that used to determine the friction law.

A notable feature of the model results is the discontinuous change in shock lengths that occurs at the transition between teardrop-shaped and blunted shocks ($\zeta = 24.6°$). No such discontinuity is evident in the experimental results. This reinforces the conclusion that, although the primary mechanism for the formation of blunted granular jumps is the presence of a Mach reflection, three-dimensional or rheological effects also play an important role.

6. Unsteady flows

The flows considered thus far have all tended quickly to a steady state after an initial transient flow. A range of flows are observed experimentally, below a critical slope angle ζ_0, which do not tend to steady flow or which do so in a complex manner. This angle is insensitive to H_f (figure 5), but decreases with increasing D. At sufficiently low ζ, no steady flows are observed, for all H_f and D.

These observations are consistent with the hypothesis that unsteady flow behaviour is related to stationary material on the plane and the stick-slip behaviour encapsulated by the heights $h_{\rm start}$ and $h_{\rm stop}$. Static uniform layers of material can exist on the plane at heights up to $h_{\rm start}$. If the depth of flowing material is similar to or smaller than this, the effect of the static layer on the location and form of the flow becomes significant. From a steady-state flow, this situation can occur either through a decrease in mass flux (and correspondingly in h), or through a decrease in ζ, with a corresponding increase in $h_{\rm start}$ and $h_{\rm stop}$.

For a given mass flux, a steady uniform flow has its thickness and velocity determined by mass conservation, and by the balance of forces

$$\mu\left(h,u\right)=\tan\zeta\,, \tag{6.1}$$

corresponding to $s_x=0$ in (2.3). If the mass flux is sufficiently small, or the cross-slope width sufficiently large, the flow height h becomes less than $h_{\rm stop}$ and no steady solution exists. The flow regime entered in this case is one of unsteady avalanching.

A typical unsteady flow is shown in figure 13. Material downstream of the impingement region is arrested by friction to form a layer of stationary material on the plane, and two shocks propagate up toward the point of impingement (figure 13*b*). The two shocks connect, and a closed shock resembling that of the steady teardrop-shaped shock is formed,

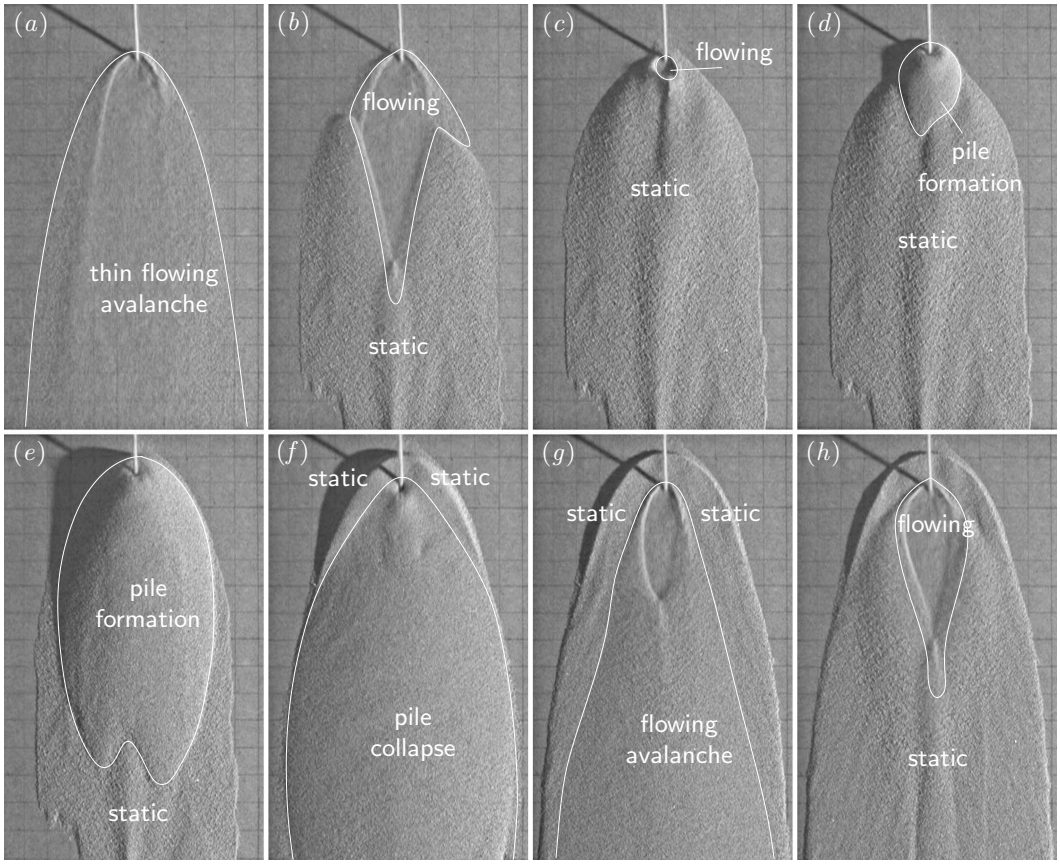

FIGURE 13. Unsteady flow, $\zeta = 26.5^\circ$, $H_f = 25$ cm, $D = 10$ mm. Material striking the plane in (a) spreads into a thin layer, as in figure 3(a). This layer slows downstream and becomes stationary (b), and the shock connecting the stationary to the flowing material propagates back towards the point of impingement $(b,\ c)$. When the shock reaches the impingement point, the flow regime changes to the formation of a conical pile (d), which grows through avalanches down its flanks. A number of such avalanches occur (e), before a collapse of the pile occurs (f). This reforms the region of thin, radial flow around the impingement point and surrounding shock (g). The material downstream is arrested by friction, and the shock again propagates inwards and towards the point of impingement (h). A movie showing the evolution of this unsteady flow is available with the online version of this paper.

although in this case the shock continually propagates inward towards the impingement point. The flowing region consists of the thin radial flow surrounding the shock, and two supercritical streams of flow immediately outside the shock that were identified in the steady-state flows. Outside this, the flow is stationary. This flowing region contrasts with that seen in a one-dimensional propagating granular bore, in which the grains are brought to rest rapidly by the shock (Gray *et al.* 2003). In the oblique shocks of 13(b), only the flow velocity normal to the shock is brought to zero, leaving tangentially flowing streams of material in the thicker flow outside the closed jump. The collision of these

streams at the vertex of the shock creates a stream of moving grains downstream of the vertex (shown in figure 13*b*), which deposits a ridge of stationary material (figure 13*b*–*e*). Up to this point, the impingement region and shallow-layer flow models presented are appropriate, and can reproduce the main features of the flow.

When the shock reaches the impingement point (figure 13*c*), the flow switches to a new regime of conical pile formation (figure 13*d*), in which the flow is no longer shallow. Material in the falling jet is slowed rapidly by impact with other material on the plane, and acts simply as a mass source at the top of the conical pile. The flow is thus very insensitive to H_f once in this regime. The pile grows through unsteady avalanching down its flanks. Avalanches are concentrated on the downslope flank of the pile, and are approximately periodic, with a period of the order a few seconds, though the position on the flank and temporal length of each avalanche vary.

Unlike pile formation on a horizontal plane, where the size of the pile grows indefinitely, a spontaneous collapse of the pile occurs on an inclined plane. Figure 13(*e*) shows the pile just before this occurs. The collapse causes a large mass of material to flow down the plane (figure 13*f*), re-mobilising the existing static layer. As a consequence of this collapse, a new region of fast radial flow surrounded by a closed shock forms around the impingement point. Uphill and to the sides of the impingement point there remains a deep pile of stationary material, the remnants of the conical pile. The flow from the collapsed part of the conical pile thins as it spreads, and becomes static as h drops below h_{stop}. As before, this causes the shock to propagate inwards toward the impingement point, and a new conical pile is formed. The cycle of conical pile formation, collapse, flow stagnation and inward shock propagation may continue over several tens of cycles.

The initiation of collapse of the growing conical pile is nearly simultaneous across the whole pile, occurring within one frame of video (1/25 second), which corresponds

to a rate of information propagation of $\gtrsim 5\ \mathrm{ms}^{-1}$. This is much faster than the gravity wave speed of $0.7\ \mathrm{ms}^{-1}$ predicted by the hyperbolic equations (2.2–2.4), indicating that the mechanism of collapse is not captured by the depth-averaged model. The collapse does not occur at a well-defined pile size; the onset appears to be very sensitive to the properties of the pile, possibly to the internal micro-structure of the grains.

Small asymmetries can be seen in figure 13(d) and 13(e), which can be attributed to variations in the height of the static material. A much greater asymmetry occurs occasionally in the collapse of the conical pile. This asymmetric collapse is due to the ridge of material seen in figure 13(b–e), which has the effect of supporting the central part of the conical pile against collapse. As a result, the collapse can occur on only one side of the pile. The resulting flow consists of an asymmetric flowing region with several shocks. The flowing region is bounded by thick stationary material from the conical pile, which diverts the flow near the impingement region to one side, and by a thinner layer of static material on the inclined plane, which restricts the downslope flow to a narrow channel. The flow is nearly steady: the restriction of the width of flowing material allows the flowing layer downstream to have a depth greater than h_{stop}, and thus be in steady uniform flow. A very slow evolution of the flow is observed, caused by erosion of the static grains, and deposition of the flowing ones, at the boundary between flowing and static material.

The shock structure in figure 14 differs from that seen in the teardrop and blunted cases. The shock surrounding region A is asymmetric, with a greater mass flux from regions A to B across shock α than that from regions A to C across shock β. Beyond the point P, the flow in region C converges with the thicker flow of region B, forming the shock γ between the two regions. Shock δ, separating regions C and D, originates at the point R, where the boundary between flowing and static grains is sharply curved.

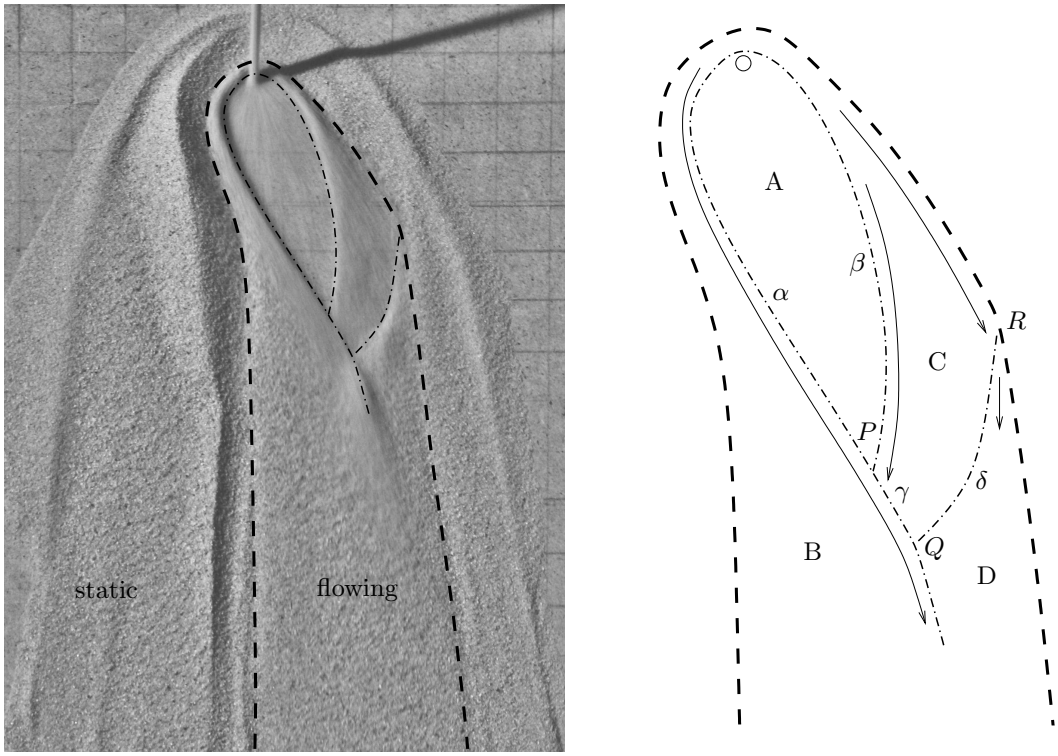

FIGURE 14. Asymmetric flow, $\zeta = 26.4^\circ$, $H_f = 9$ cm, $D = 8$ mm. Dashed lines indicated the boundary of the flowing region; thin dot-dash lines indicate the location of shocks. The flow is quasi-steady, in the sense the time-dependence is through slow evolution of the boundary between static and flowing grains.

This is an oblique shock, analogous to that found in the case of a compression ramp in supersonic gas dynamics (Courant & Friedrichs 1977) and in converging channels of flowing granular material (Gray & Cui 2007). A second shock interaction point is formed at Q.

7. Conclusion

The flow generated by impingement of a granular jet on an inclined plane, while having similarities with its fluid counterpart, exhibits a range of behaviour specific to granular materials. Two distinct steady-state flow regimes displaying closed granular jumps have been found, one with a teardrop-shaped shock and one with a smooth, 'blunted' shock. In these two regimes, the principal features of the flow, listed from the point of impingement outwards, are a fast-moving region of thin radial flow, a closed granular jump,

rapid streams of material flowing nearly tangentially to the shock, a region of slower downslope flow, and static material outside the flowing region. The two regimes differ in the supercritical or subcritical nature of the thicker flow surrounding the shock; fully supercritical flow leads to a teardrop-shaped shock, whereas subcritical flow surrounding the downstream part of the shock leads to a blunted shock.

These flows have been modelled through a shallow-layer approximation, leading to a system of hyperbolic equations. The concepts of sub- or super-critical flow and shock waves which result from these equations are fundamental to an understanding of the flow. Numerical solutions of the model equations reproduce the phase diagram of the solution regimes, and quantitatively predict features such as flow velocity and the shock length in the regime of steady teardrop-shaped shocks. The three-dimensional breaking wave observed in blunted shocks is outside the scope of the depth-averaged model, but the overall form of flow is nonetheless correctly reproduced, displaying quantitative agreement with the measured flow velocity.

The steady granular jumps, and the radial flow within them, are governed primarily by conservation of mass and momentum. Outside the shock, in the slower down-slope flow, the basal friction and gravity source terms play an important role. The balance of these forces governs the flow far downstream, and influences the form of the granular jump through control of the flow on the downstream side of the shock.

At sufficiently low slope angles, there is no steady balance between gravity and friction in the down-slope flow. Instead, the hysteretic nature of the transition between flowing and stationary material, encapsulated in the functions $h_{\rm start}$ and $h_{\rm stop}$ leads to oscillatory behaviour and periodic avalanching. The exact mechanism is unclear, however, for transition between stationary and moving flow (involved in the erosion and deposition of static material), and for the sudden collapse of the conical pile. Such regimes are known

to exhibit complex dynamics (Pouliquen & Forterre 2002), and are likely dependent on details of the grain micro-structure.

Chris Johnson acknowledges support from NERC DTG NE/G523747/1 and an EPSRC DTA. Nico Gray was supported by NERC grant NE/E003206/1 and an EPSRC Advanced Research Fellowship GR/S50052/01 & GR/S50069/01.

REFERENCES

Akers, B. & Bokhove, O. 2008 Hydraulic flow through a channel contraction: Multiple steady states. *Phys. Fluids* **20**, 056601.

Boudet, J. F., Amarouchene, Y., Bonnier, B. & Kellay, H. 2007 The granular jump. *J. Fluid Mech.* **572**, 413–431.

Brennen, C. E., Sieck, K. & Paslaski, J. 1983 Hydraulic jumps in granular material flow. *Powder Tech.* **35**, 31–37.

Bush, J. W. M. & Aristoff, J. M. 2003 The influence of surface tension on the circular hydraulic jump. *J. Fluid Mech.* **489**, 229–238.

Bush, J. W. M. & Hasha, A. E. 2004 On the collision of laminar jets: fluid chains and fishbones. *J. Fluid Mech.* **511**, 285–310.

Courant, R. & Friedrichs, K. O. 1977 *Supersonic flow and shock waves*. Springer.

Courant, R. & Hilbert, D. 1962 *Methods of mathematical physics*. Interscience New York.

Cui, X., Gray, J. M. N. T. & Jóhannesson, T. 2007 Deflecting dams and the formation of oblique shocks in snow avalanches at Flateyri, Iceland. *J. Geophys. Res.* **112** (F4), F04012.

Doyle, E. E., Huppert, H. E., Lube, G., Mader, H. M. & Sparks, R. S. J. 2007 Static and flowing regions in granular collapses down channels: insights from a sedimenting shallow water model. *Phys. Fluids* **19**, 106601.

Edwards, C. M., Howison, S. D., Ockendon, H. & Ockendon, J. R. 2008 Non-classical shallow water flows. *IMA J. Appl. Math.* **73** (1), 1–21.

Eglit, M. E. 1983 Some mathematical models of snow avalanches. In *Advances in mechanics and the flow of granular materials* (ed. M. Shahinpoor), p. 577. Zellerfeld and Gulf.

Eglit, M. E., Kulibaba, V. S. & Naaim, M. 2007 Impact of a snow avalanche against an obstacle. Formation of shock waves. *Cold Reg. Sci. Technol.* **50** (1–3), 86–96.

Forterre, Y. & Pouliquen, O. 2003 Long-surface-wave instability in dense granular flows. *J. Fluid Mech.* **486**, 21–50.

Gray, J. M. N. T. & Cui, X. 2007 Weak, strong and detached oblique shocks in gravity-driven granular free-surface flows. *J. Fluid Mech.* **579**, 113–136.

Gray, J. M. N. T. & Hutter, K. 1997 Pattern formation in granular avalanches. *Continuum Mech. Therm.* **9** (6), 341–345.

Gray, J. M. N. T., Tai, Y. C. & Noelle, S. 2003 Shock waves, dead zones and particle-free regions in rapid granular free-surface flows. *J. Fluid Mech.* **491**, 161–181.

Gray, J. M. N. T., Wieland, M. & Hutter, K. 1999 Free surface flow of cohesionless granular avalanches over comples basal topography. *Proc. R. Soc. A* **455**, 1841–1874.

Grigoryan, S. S., Eglit, M. E. & Yakimov, Yu. L. 1967 New state and solution of the problem of the motion of snow avalanche. *Tr. Vysokogornogo Geofizich. Inst.* **12**, 104–113.

Gruber, U. & Bartelt, P. 2007 Snow avalanche hazard modelling of large areas using shallow water numerical methods and GIS. *Environ. Modell. Softw.* **22** (10), 1472–1481.

Hákonardóttir, K. M. & Hogg, A. J. 2005 Oblique shocks in rapid granular flows. *Phys. Fluids* **17**, 077101.

Hasson, D. & Peck, R. E. 1964 Thickness distribution in a sheet formed by impinging jets. *A. I. Ch. E. Journal* **10** (5), 752–754.

Iverson, R. M. 1997 The physics of debris flows. *Rev. Geophys.* **35** (3), 245–296.

Iverson, R. M. & Denlinger, R. P. 2001 Flow of variably fluidized granular masses across three-dimensional terrain: 1. Coulomb mixture theory. *J. Geophys. Res.* **106** (B1), 537–552.

Jiang, G-S. & Tadmor, E. 1998 Nonoscillatory central schemes for multidimensional hyperbolic conservation laws. *SIAM J. Sci. Comput.* **19** (6), 1892–1917.

Kate, R. P., Das, P. K. & Chakraborty, S. 2007 Hydraulic jumps due to oblique impingement of circular liquid jets on a flat horizontal surface. *J. Fluid Mech.* **573**, 247–263.

Lajeunesse, E., Mangeney-Castelnau, A. & Vilotte, J. P. 2004 Spreading of a granular mass on a horizontal plane. *Phys. Fluids* **16**, 2371.

LeVeque, R. J. 1992 *Numerical methods for conservation laws*. Birkhäuser.

LeVeque, R. J. 2002 *Finite Volume Methods for Hyperbolic Problems*. *Cambridge Texts in Applied Mathematics* 31. Cambridge University Press.

Liu, A.J. & Nagel, S.R. 1998 Jamming is not just cool any more. *Nature* **396**, 21–22.

Lube, G., Huppert, H.E., Sparks, R.S.J. & Hallworth, M.A. 2004 Axisymmetric collapses of granular columns. *J. Fluid Mech.* **508**, 175–199.

Mitchell, J. K. & Soga, K. 2005 *Fundamentals of soil behavior*. John Wiley & Sons Ltd Chichester, UK.

Nessyahu, H. & Tadmor, E. 1990 Non-oscillatory central differencing for hyperbolic conservation laws. *J. Comput. Phys.* **87** (2), 408–463.

Pouliquen, O. 1999 Scaling laws in granular flows down rough inclined planes. *Phys. Fluids* **11** (3), 542–548.

Pouliquen, O. & Forterre, Y. 2002 Friction law for dense granular flows: application to the motion of a mass down a rough inclined plane. *J. Fluid Mech.* **453**, 133–151.

Rajchenbach, J. 2000 Granular flows. *Adv. Phys.* **49** (2), 229–256.

Lord Rayleigh 1914 On the theory of long waves and bores. *Proc. R. Soc. A* **90** (619), 324–328.

Rericha, E. C., Bizon, C., Shattuck, M. D. & Swinney, H. L. 2002 Shocks in supersonic sand. *Phys. Rev. Lett.* **88** (1), 6338.

Rouse, H. 1949 *Engineering Hydraulics*. Wiley.

Royer, J. R., Evans, D. J., Oyarte, L., Guo, Q., Kapit, E., Möbius, M. E., Waitukaitis, S. R. & Jaeger, H. M. 2009 High-speed tracking of rupture and clustering in freely falling granular streams. *Nature* **459**, 1110–1113.

Savage, S. B. 1979 Gravity flow of cohesionless granular materials in chutes and channels. *J. Fluid Mech.* **92** (01), 53–96.

Savage, S. B. & Hutter, K. 1989 The motion of a finite mass of granular material down a rough incline. *J. Fluid Mech.* **199**, 177–215.

Schach, W. 1934 Umlenkung eines freien Flüssigkeitsstrahles an einer ebenen Platte. *Ing. Arch.* **5** (4), 245–265.

Staron, L. & Hinch, E. J. 2005 Study of the collapse of granular columns using two-dimensional discrete-grain simulation. *J. Fluid Mech.* **545**, 1–27.

Tai, Y. C., Noelle, S., Gray, J. M. N. T. & Hutter, K. 2001 An accurate shock-capturing finite-difference method to solve the Savage Hutter equations in avalanche dynamics. *Ann. Glaciol.* **32** (1), 263–267.

Tai, Y. C., Noelle, S., Gray, J. M. N. T. & Hutter, K. 2002 Shock-capturing and front-tracking methods for granular avalanches. *J. Comput. Phys.* **175** (1), 269–301.

Taylor, G. I. 1960 Formation of thin flat sheets of water. *Proc. R. Soc. A* **259** (1296), 1–17.

Taylor, G. I. 1966 Oblique impact of a jet on a plane surface. *Phil. Trans. R. Soc. A* **260** (1110), 96–100.

Thorpe, S. A. & Kavcic, I. 2008 The circular internal hydraulic jump. *J. Fluid Mech.* **610**, 99–129.

Vreman, A. W., Al-Tarazi, M., Kuipers, J. A. M., van Sint Annaland, M. & Bokhove, O. 2007 Supercritical shallow granular flow through a contraction: experiment, theory and simulation. *J. Fluid Mech.* **578**, 233–269.

Watson, E. J. 1964 The radial spread of a liquid jet over a horizontal plane. *J. Fluid Mech.* **20** (03), 481–499.

Weiyan, T. 1992 *Shallow water hydrodynamics*. Elsevier.

Zhao, J. & Khayat, R. E. 2008 Spread of a non-Newtonian liquid jet over a horizontal plate. *J. Fluid Mech.* **613**, 411–443.

4. Conclusion

This thesis has presented experiments and modelling of two unconfined granular flows. In each case, a simple kinematic or depth-averaged model has captured the dominant flow processes.

In *The kinematics of levee formation in geophysical mass flows*, a detailed model of levee formation kinematics has been proposed, which describes how coarse-particle-rich levees result from a combination of segregation and transport processes within a debris flow head. While the kinematic processes have been described in detail, the dynamics involved in the formation of levees, and the resulting self-channelised flow, are much less well understood. Historically, the assumptions of a uniform Bingham rheology and instantaneous, en masse deposition for allowed interpretations about the flow rheology to be made from the shape and structure of deposits. Our experimental results show that the deposition process is not simply an en masse stopping, and are consistent with the more recent hypothesis of a spatially heterogeneous rheology, in which coarse-rich levees are considerably more frictional than the interior flow, allowing them to support the pressure of the fluidised channel flow. However, the lack of a detailed dynamical model for the progressive levee formation that we observe means that it is not yet possible to infer dynamical flow parameters, such as the velocity, mass flux and rheology, from measurements of leveed channel deposits. Inferences of this sort are important in practical hazard assessment since, in most regions, the only record of past geophysical mass flows is through historical flow deposits. While the modelling in this paper does not solve the question of flow dynamics, the experimental observation of levee formation by streamwise accretion close to the flow front implies that the dynamics responsible for setting the width of levees occurs in the flow head. The study of dynamics within the flow head provides an interesting direction for future research: construction of a momentum balance

model within the flow head (similar to the mass balance model constructed in this thesis) may provide information about the dynamics of large- and small-scale self-channelised flows, without requiring a full rheology.

In *Granular jets and hydraulic jumps on an inclined plane*, a depth-averaged model is used to predict the closed teardrop-shaped and blunted granular shocks that occur when a jet of granular material impinges on an inclined plane. Despite assumptions made about the flow close to the impingement point (for which an inviscid fluid model is used), quantitative agreement between experiments and model predictions is achieved for teardrop-shaped shocks. This agreement demonstrates that, in this regime, the dominant physical process is the conservation of mass and slope-tangential momentum across a granular jump, encapsulated in the depth-averaged model. The transition between teardrop-shaped and blunted shocks, captured in the model by the transition from a regular to a Mach shock reflection, is further evidence that shock dynamics are a central part of the governing physics. Away from the regime of teardrop-shaped shocks, there is evidence that other processes are important. For example, the experimental blunted shock is smooth, with no evidence of the shock triple point predicted by the depth-averaged model. The jump conditions, which determine the shock structure, are not dependent on the basal friction, indicating that the other effects of the granular rheology such as horizontal shear stresses may be significant at this point. In the regime of unsteady flows, the complex interaction between stationary and flowing material on the plane reflects another aspect of granular rheology. These flows may provide an effective test for current and future rheological models.

Bibliography

Branney, M. J. & Kokelaar, B. P. 2002 *Pyroclastic density currents and the sedimentation of ignimbrites*. Geological Society Publishing House.

Campbell, C. S. 1990 Rapid Granular Flows. *Annu. Rev. Fluid Mech.* **22** (1), 57–90.

Lord Bishop of Clogher 1712 An account of the subsiding, or sinking down of part of a hill near clogher in Ireland. *Phil. Trans.* **28**, 267–269.

Cui, X., Gray, J. & Jóhannesson, T. 2007 Deflecting dams and the formation of oblique shocks in snow avalanches at Flateyri, Iceland. *J. Geophys. Res* **112**.

GDR MiDi 2004 On dense granular flows. *The European Physical Journal E: Soft Matter and Biological Physics* **14** (4), 341–365.

Gray, J. M. N. T., Tai, Y. C. & Noelle, S. 2003 Shock waves, dead zones and particle-free regions in rapid granular free-surface flows. *Journal of Fluid Mechanics* **491**, 161–181.

Hákonardóttir, K. M. & Hogg, A. J. 2005 Oblique shocks in rapid granular flows. *Physics of Fluids* **17**, 077101.

Hungr, O., Evans, S. G., Bovis, M. J. & Hutchinson, J. N. 2001 A review of the classification of landslides of the flow type. *Environ. Eng. Geosci.* **7** (3), 221.

Iverson, R. M. & Denlinger, R. P. 2001 Flow of variably fluidized granular masses across three-dimensional terrain: 1. Coulomb mixture theory. *J. Geophys. Res* **106** (B1), 537–552.

Iverson, R. M., Logan, M., LaHusen, R. G. & Berti, M. 2010 The perfect debris flow? Aggregated results from 28 large-scale experiments. *J. Geophys. Res.* **115** (F3), F03005.

Jóhannesson, T., Gauer, P., Issler, P. & Lied, K., ed. 2009 *The design of avalanche protection dams: Recent practical and theoretical developments*. European Commission.

Jop, P., Forterre, Y. & Pouliquen, O. 2006 A constitutive law for dense granular flows. *Nature* **441** (7094), 727–730.

Pouliquen, O. 1999 Scaling laws in granular flows down rough inclined planes. *Phys. Fluids* **11** (3), 542–548.

Savage, S. B. & Hutter, K. 1989 The motion of a finite mass of granular material down a rough incline. *J. Fluid Mech.* **199**, 177–215.

Takahashi, T. 2007 *Debris flow: mechanics, prediction and countermeasures*. Routledge.